COPPE
UFRJ

**Instituto Alberto Luiz Coimbra de
Pós-Graduação e Pesquisa de Engenharia**

NUMERICAL ANALYSIS OF TWO-PHASE FLOW IN A MICRO-REACTOR FOR BIODIESEL PRODUCTION

Antônio Emanuel Marques dos Santos

Dissertação de Mestrado apresentada ao Programa de Pós-graduação em Engenharia Mecânica, COPPE, da Universidade Federal do Rio de Janeiro, como parte dos requisitos necessários à obtenção do título de Mestre em Engenharia Mecânica.

Orientadores: Gustavo Rabello dos Anjos
              Gustavo César Rachid Bodstein

Rio de Janeiro
Setembro de 2025

NUMERICAL ANALYSIS OF TWO-PHASE FLOW IN A MICRO-REACTOR FOR BIODIESEL PRODUCTION

Antônio Emanuel Marques dos Santos

DISSERTAÇÃO SUBMETIDA AO CORPO DOCENTE DO INSTITUTO ALBERTO LUIZ COIMBRA DE PÓS-GRADUAÇÃO E PESQUISA DE ENGENHARIA DA UNIVERSIDADE FEDERAL DO RIO DE JANEIRO COMO PARTE DOS REQUISITOS NECESSÁRIOS PARA A OBTENÇÃO DO GRAU DE MESTRE EM CIÊNCIAS EM ENGENHARIA MECÂNICA.

Orientadores: Gustavo Rabello dos Anjos
Gustavo César Rachid Bodstein

Aprovada por: Prof. Rafael Menezes de Oliveira
Prof. Daniel José Nahid Mansur Chalhub
Prof. Gustavo César Rachid Bodstein
Prof. Gustavo Rabello dos Anjos

RIO DE JANEIRO, RJ – BRASIL
SETEMBRO DE 2025

Do not labor for the food which
perishes, but for the food which
endures to everlasting life, which
the Son of Man will give you,
because God the Father has set
His seal on Him.
(John 6:27)

Acknowledgments

First and foremost, I thank God, whose Word, grace, strength, and guidance sustained me throughout this journey and made the completion of this work possible.

I would like to express my deepest gratitude to my advisor, Professor PhD. Gustavo Rabello dos Anjos, for his constant guidance, encouragement, and insightful discussions throughout the development of this work. His expertise and dedication were fundamental to the successful completion of this dissertation. I also extend my sincere thanks to my co-advisor, Professor PhD. Gustavo César Rachid Bodstein, whose valuable advice and support greatly enriched this research.

My appreciation goes to the staff of LABMFA, Jaciara Roberta, Carlos Lionel, and Antônia, for their continuous assistance and for providing an environment that was both professional and welcoming. I am also thankful to my colleagues at LABMFA — Daniel Barbedo, Higor Odilon, Gabriel Sousa, and Lucas Miranda — for the many stimulating discussions, collaborative spirit, and friendship that made this academic journey more rewarding.

I am also grateful to the colleagues I met during this master's program — Gian, Filipe, Carol, Emely, and Bruninho — for their companionship, encouragement, and the many moments we shared that enriched both my academic and personal life.

I owe my heartfelt gratitude to my parents, Áurea and Ani dos Santos, whose love, sacrifices, and encouragement have been the foundation of all my achievements. I give my special thanks to my wife, Laylla, for her unwavering support, patience, prayers and love during the most challenging moments of this work. Her presence was a constant source of motivation and strength.

I wish to dedicate a heartfelt in memoriam to Vera and Tito, who were part of the secretary staff of the Mechanical Engineering Program. Their kindness, dedication, and generosity touched the lives of many students, and their memory will always remain with those who had the privilege to know them.

Resumo da Dissertação apresentada à COPPE/UFRJ como parte dos requisitos necessários para a obtenção do grau de Mestre em Ciências (M.Sc.)

NUMERICAL ANALYSIS OF TWO-PHASE FLOW IN A MICRO-REACTOR
FOR BIODIESEL PRODUCTION

Antônio Emanuel Marques dos Santos

Setembro/2025

Orientadores: Gustavo Rabello dos Anjos
Gustavo César Rachid Bodstein

Programa: Engenharia Mecânica

A crescente demanda global por fontes de energia sustentáveis tem impulsionado avanços significativos nas tecnologias de produção de biodiesel. Os microrreatores surgiram como uma alternativa promissora aos reatores contínuos e em lote convencionais devido às suas características aprimoradas de transferência de calor e massa, bem como ao seu potencial de intensificação do processo. Este estudo apresenta uma investigação numérica do comportamento do escoamento em microrreatores usados para a síntese de biodiesel, com foco no impacto de diferentes configurações geométricas e na presença de obstáculos dentro do reator. O principal objetivo desta pesquisa é avaliar a influência do projeto do microrreator na dinâmica do escoamento e na eficiência da mistura. As equações que regem o escoamento e o transporte das espécies químicas são discretizadas usando o Método dos Elementos Finitos de Galerkin (FEM) combinado com um esquema de advecção semilagrangeano, garantindo uma representação de alta fidelidade da dinâmica do fluido e das reações químicas. As simulações são realizadas para diferentes configurações de microrreatores, incluindo projetos com e sem obstáculos, para analisar seu efeito nos padrões de escoamento e na evolução da reação. Os resultados indicam que a inclusão de obstáculos aumenta a mistura ao induzir a advecção caótica e promover interações interfaciais entre os reagentes. Além disso, a análise destaca a importância das variações do regime de escoamento, especialmente em diferentes números de Reynolds, sobre a estabilidade e a eficiência do processo de síntese de biodiesel. As descobertas deste estudo contribuem para a otimização do projeto do microrreator, oferecendo percepções sobre as configurações mais eficazes para aumentar a eficiência da produção de biodiesel.

NUMERICAL ANALYSIS OF TWO-PHASE FLOW IN A MICRO-REACTOR FOR BIODIESEL PRODUCTION

Antônio Emanuel Marques dos Santos

September/2025

Advisors: Gustavo Rabello dos Anjos
Gustavo César Rachid Bodstein

Department: Mechanical Engineering

The increasing global demand for sustainable energy sources has driven significant advancements in biodiesel production technologies. Microreactors have emerged as a promising alternative to conventional batch and continuous reactors due to their enhanced heat and mass transfer characteristics, as well as their potential for process intensification. This study presents a numerical investigation of the flow behavior in microreactors used for biodiesel synthesis, focusing on the impact of different geometrical configurations and the presence of obstacles within the reactor. The primary objective of this research is to evaluate the influence of microreactor design on flow dynamics and mixing efficiency. The governing equations of the flow and the species transport equations are discretized using the Galerkin Finite Element Method (FEM) combined with a Semi-Lagrangean advection scheme, ensuring a high-fidelity representation of the fluid dynamics and chemical reactions. Simulations are performed for different microreactor configurations, including designs with and without obstacles, to analyze their effect on flow patterns and reaction evolution. Results indicate that the inclusion of obstacles enhances mixing by inducing chaotic advection and promoting interfacial interactions between reactants. Additionally, the analysis highlights the significance of flow regime variations, particularly at different Reynolds numbers, on the stability and efficiency of the biodiesel synthesis process. The findings of this study contribute to the optimization of microreactor design, offering insights into the most effective configurations for enhancing biodiesel production efficiency.

Contents

List of Figures

List of Tables

List of Symbols

Symbol	Description
c_s	Dimensionless scalar concentration
D_s	Molecular diffusion coefficient
H	Channel height
L	Channel length
N	Number of nodes
p	Pressure
t	Time
u, v	Velocity components in x and y directions
Δt	Time step
$\Delta x, \Delta y$	Spatial steps in x and y directions
α	Volume fraction
δ	Kronecker delta
μ	Dimensionless dynamic viscosity
ν	Dimensionless kinematic viscosity
ρ	Dimensionless fluid density
Re	Reynolds number
Re_{TG}	Reynolds number based on triglyceride properties
Pe	Péclet number
MI	Mixing Index
PI	Performance Index
Pe	Péclet number
Kn	Knudsen number
WCO	Wasting Cooking Oil
SFO	Sunflower Oil

Chapter 1

Introduction

The rising cost of oil, the depletion of oil reserves, and the growing environmental concerns, mainly due to the pollution caused by the combustion of fossil fuels, have led to the development of alternative fuel sources, such as biodiesel [5–7]. Biodiesel is commonly produced through the transesterification reaction of vegetable oils, frying oils or animal fats with short-chain alcohols, such as methanol or ethanol, in the presence of a catalyst [6].

Biodiesel production is typically carried out in batch or continuous processes. Traditional methods rely on stirred tank reactors or batch reactors, and the transesterification process in these reactors uses long residence times (from one hour to several hours) and high temperatures [8, 9]. In batch systems, a fixed amount of reactants is processed, while continuous systems have a constant flow of reactants [10]. Among various techniques for process intensification in biodiesel synthesis, microreactor technology stands out as a promising option. Microreactors can improve chemical processing by enhancing mass and heat transfer rates. They also offer safer and more sustainable operations [11–14]. However, achieving effective mixing in microreactors remains a challenge. Microreactor flows tend to be laminar, where diffusion is the primary mixing mechanism [15].

Introducing obstacles, such as cylindrical pins and rectangular elements, in microchannels has been shown to improve mixing. These obstacles induce chaotic advection, which improves heat and mass transfer [2, 16]. Flow around cylinders is well understood on a macro-scale [17], but micro-scale flows introduce unique challenges. These include high blockage (the ratio of cylinder diameter to channel width) and low aspect ratios (the ratio of cylinder length to diameter) [18]. In micromixers, cylindrical obstacles face both lateral and vertical confinement, which can alter the flow dynamics. Confinement may prevent vortex shedding [19]. However, under high Reynolds numbers, vortex shedding can still occur. This phenomenon generates periodic changes in the local flow direction, creating flow vortices that improve mixing by stretching and folding the fluid streams [20].

Although the amount of biodiesel produced by a single microreactor is not substantial, one advantage of these microdevices is that it is easy to scale up production by using a larger number of microreactors in parallel. Whereas scaling up by increasing the size of conventional reactors would require an increase in the size of each reactor unit, which is sometimes difficult, expensive and time-consuming. In addition, scaling up production using microreactors allows for the construction of a portable biofuel production unit, thus making it possible to generate energy in remote and difficult-to-access locations [21].

Depending on the flow conditions - such as the mass flow rate, the ratio between phases, and the density and viscosity of the fluids involved - various characteristic distributions of the phase geometries can be formed, as shown in Figure 1.1. These distributions, called flow patterns, not only represent visual distinctions, but also have a direct influence on many of its properties, such as pressure gradients related to pressure drop and heat exchange coefficients.

(a)

(b)

(c)

(d)
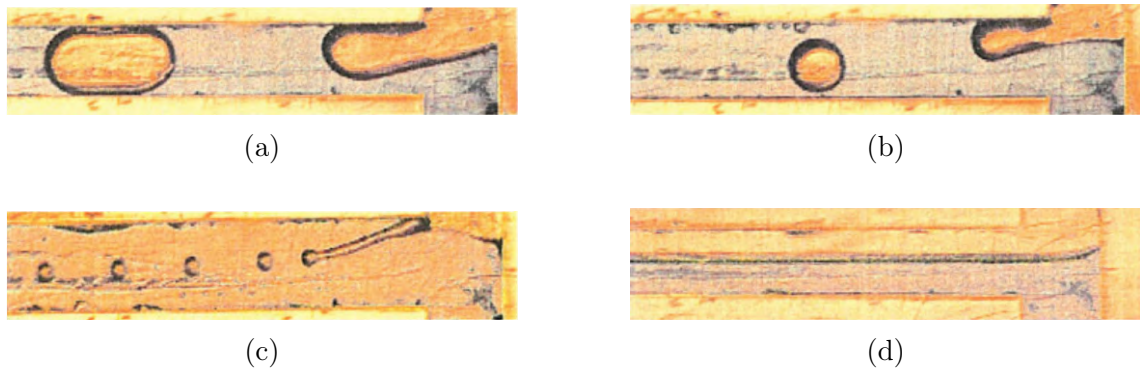
Figure 1.1: Flow patterns at the T-junction of a microchannel found by ZHAO *et al.* [1] in experiments with water and kerosene.

This research aims to numerically evaluate the flow behavior in different microreactor geometries, with and without obstacles. By examining various microreactor geometries, this study aims to determine the optimal conditions for flow in biodiesel synthesis, thereby enhancing the efficiency of compact and sustainable biodiesel production technologies.

The structure of this work is organized as follows:

- Chapter 1: Introduction;

- Chapter 2: Literature Review;

- Chapter 3: Methodology;

- Chapter 4: Validation and Results;

- Chapter 5: Conclusion.

Chapter 1 consists of this introduction to the topic and the work, containing the main aspects of its organization.

Chapter 2 presents a literature review, divided into five topics of interest: biodiesel production, microreactors in biodiesel synthesis, flow behavior in microchannels, simulation of multiphase flows in microreactors and interface representation techniques.

Chapter 3 then explains the methodology proposed for simulating two-phase miscible fluids flow. In summary, the flows are modeled by the two-dimensional incompressible Navier-Stokes equations, which are approximated by the Finite Element Method. The Galerkin method is employed to discretize the equations in the spatial domain, while the semi-Lagrangian method is used to discretize the material derivative in the space-time domain. A one-fluid approach is used, whereby the domain occupied by the two-phase flow is described by a single set of equations. An unstructured static triangular mesh is defined over the entire length of the spatial domain. The proposed methodology was implemented in a Python code, which is described through a pseudo-code presented at the end of this chapter.

Chapter 4 presents the results of the simulations carried out using the implemented code, with the objective of validating the proposed methodology. In addition to the results, each case includes all the flow input data, the main parameters of the computational meshes used, and the duration of each simulation. This level of detail is intended to ensure that all results presented in this work can be easily reproduced and verified by peers. The initial simulations focused on flow between parallel plates, lid-driven cavity flow, and backward-facing step flow, aiming to validate the application of the methodology to single-phase flows, which are comparatively simpler. Subsequently, the methodology was validated for the target miscible two-phase flows, with particular emphasis on the flow within a Hele-Shaw cell. The results obtained from these simulations showed good agreement with analytical solutions as well as with numerical and experimental results reported in the literature, thereby confirming the validity of the methodology for modeling miscible two-phase flows. In addition to the validation cases, further simulations of practical interest were performed to investigate the influence of specific parameters on flow behavior in microchannels. The conclusions drawn from these analyses are also included in this chapter.

Finally, Chapter 5 presents the overall conclusions drawn from the development of this dissertation, along with suggestions for future work.

Chapter 2

Literature Review

This chapter presents a literature review on biodiesel production and key aspects related to its computational simulation. Its purpose is to introduce the topic in a focused manner, discussing and analyzing the various possible approaches that can be adopted, thereby clarifying the choices made in the development of the methodology proposed in this work.

This chapter is organized into five sections, each addressing one of the main topics reviewed:

- Biodiesel Production;

- Microreactors in Biodiesel Synthesis;

- Flow Behavior in Microchannels;

- Simulation of Multiphase Flows in Microreactors;

- Interface Representation Techniques.

2.1 Biodiesel Production

Biodiesel is chemically defined as a long-chain fatty acid mono-alkyl ester derived from renewable sources such as vegetable oils, animal waste, charcoal, crop residues, timber, and microbial feedstock through biological processes [22–25]. Depending on the biomass, biofuel could be categorized into three generations: first, second, and third [26]. The first-generation biofuel is produced from food crops, whereas the second-generation biodiesel contains various nonfood-based materials like lignocellulosic biomass, crop residues, and forest residues [26]. On the other hand, third-generation biofuel is derived from the biomass of different living organisms, including micro and macroalgae [27].

Biodiesel is highly regarded as a suitable biofuel for transportation due to its low carbon footprint, higher degradability, and widely accessible raw materials [28]. Numerous nonedible oils (various plant and animal oils) are readily available for biodiesel manufacturing, as most of these raw materials are considered waste. Therefore, food security concerns are limited in biodiesel production as it does not place a strain on edible sources [29]. Biodiesel can be produced through various processes, such as micro-emulsions, dilution, thermal cracking or pyrolysis and esterification and transesterification reactions [30–34]. The transesterification reaction is the most commonly used in the production of biodiesel [35]. Biodiesel generated through this technique has properties as good as diesel. In addition, transesterification is economically advantageous for industrial processing [36]. In this reaction, triglycerides, the main components of vegetable oils, react with alcohol to produce mono-alkyl ester and glycerol [37].

The transesterification reaction is an endothermic and reversible reaction that takes place in three consecutive steps. In the first step, diglycerides (DG) are obtained from the reaction of alcohol (A) with triglycerides (TG). In the second step, monoglycerides (MG) are produced from the reaction of alcohol with diglycerides and, in the last step, glycerol (GL) is obtained from the reaction of alcohol with monoglycerides. In all the reaction steps, fatty acid ethyl or esters are obtained if the alcohol used is ethanol or fatty acid methyl esters are obtained if the alcohol used is methanol [38, 39]. Fatty acid esters represent biodiesel (B) and in Brazil, the minimum amount of biodiesel accepted by the National Agency for Petroleum, Natural Gas and Biofuels (ANP) is 96.5 %, i.e. the final product of the reaction must have at least 96.5 % esters [21]. Equation 2.1 shows the overall transesterification reaction, where the triglyceride reacts with the alcohol to produce ester and glycerol. Equations 2.2, 2.3 and 2.4 show the same overall reaction shown in 2.1 but detailing the breakdown of this overall reaction into the three intermediate steps of the transesterification reaction, which allows the appearance of the intermediate glycerides to be visualized, where k_i are the kinetic constants [40].

$$\text{Triglyceride} + 3\,\text{Alcohol} \underset{k_2}{\overset{k_1}{\rightleftharpoons}} \text{Glycerol} + 3\,\text{Ester} \tag{2.1}$$

$$\text{Triglyceride} + \text{Alcohol} \underset{k_2}{\overset{k_1}{\rightleftharpoons}} \text{Diglyceride} + \text{Ester} \tag{2.2}$$

$$\text{Diglyceride} + \text{Alcohol} \underset{k_4}{\overset{k_3}{\rightleftharpoons}} \text{Monoglyceride} + \text{Ester} \tag{2.3}$$

$$\text{Monoglyceride} + \text{Alcohol} \underset{k_6}{\overset{k_5}{\rightleftharpoons}} \text{Glycerol} + \text{Ester} \tag{2.4}$$

A surrogate model for kinetics regarding the global equation is as follows [41]:

$$(-\dot{R}_{TG}) = -\frac{dc_{TG}}{dt} = \overrightarrow{k}\,c_{TG}c_A - \overleftarrow{k}\,c_E c_{GL} \tag{2.5}$$

where $-\dot{R}$ is the reaction rate ($mol\ m^{-3}s^{-1}$), $\overrightarrow{k}$ and $\overleftarrow{k}$ are the reaction rate constants for direct and reverse reactions ($m^3\ mol^{-1}s^{-1}$), respectively, c is the molar concentration ($mol\ m^{-3}$), and the subscripts TG, A, GL and E denote triglyceride, alcohol, glycerol and ethyl ester species.

2.2 Microreactors in Biodiesel Synthesis

This section presents the main microreactor designs used in biodiesel synthesis, such as straight channels, serpentine channels, and T- or Y-junctions, and discusses their impact on reaction performance.

Microreactor technology has emerged as a highly efficient method for biodiesel production, offering significant advantages over conventional batch reactors [22]. The technology utilizes continuous flow reactors with small internal dimensions to enhance heat and mass transfer, reduce reaction times, and achieve superior biodiesel yields [42]. GOPI *et al.* [43] highlighted that microreactors, such as T-shaped and zigzag microchannel reactors, provide improved mixing rates and reaction efficiencies due to their high surface-area-to-volume ratio. For example, zigzag microchannel designs have achieved biodiesel yields exceeding 99% within short residence times, primarily attributed to intensified volumetric mass transfer and droplet formation dynamics. Moreover, microreactors allow for efficient use of heterogeneous catalysts, further reducing energy consumption and production costs, making them a sustainable alternative for scaling biodiesel production.

MOHD LAZIZ *et al.* [44] reported the synthesis of biodiesel at an ambient room environment (25 ˚C) in a microchannel reactor using refined cooking palm oil as feedstock. The microchannel reactor consisted of a T-junction and an internal diameter of 690 μm. A biodiesel yield of 98.6 % was achieved within 40 s using 5 wt.% potassium hydroxide, KOH to catalyze the reaction. With the results of numerical simulations, the detailed flow structure inside the methanol slug was discussed in terms of relative velocity, vector, and streamline profile. A torus-shaped recirculation pattern is found inside the slug that enhances the mixing and mass transfer of oil, hence improving the overall transesterification reaction.

GUAN *et al.* [45, 46] investigated flow patterns in the course of transesterification of waste cooking oil (WCO), sunflower oil (SFO) with water and/or oleic acid as a model of WCO, and pure SFO in the presence of a KOH catalyst in microtubes. FAME yield for the transesterification of WCO reached more than 89% in

the microtube reactors with a residence time of 252 s at 333 K. The flow patterns when using WCO were changed from a liquid-liquid slug flow at the inlet region to a parallel flow at the middle region, and then to a homogeneous liquid flow at the outlet region as the reaction proceeded at 333 K. Fine droplets containing glycerol and methanol generally formed in oil slugs when using pure SFO, but were almost unobservable when using WCO.

RICHARD *et al.* [38] performed the sunflower oil ethanolysis in a micro-scaled device, inducing better control for heat and mass transfer in comparison with batch processes. Kinetic data was acquired during the first seconds of the reaction to determine kinetic constants and mass transfer coefficients. For all the ethanol-to-oil molar ratios evaluated (6.0, 9.0, 16.2, 22.7, and 45.4), the two liquids formed an annular flow. With the evolution of the reaction, the medium appeared to be homogeneous although there were two phases on the microreactor (composed of very small droplets of glycerol in the ester phase). A model able to represent both mass transfer phenomenon and reaction kinetics at a 65 °C for the transesterification reaction between high oleic sunflower oil and ethanol was built.

XIE *et al.* [22] provided an overview of the current status of research on biodiesel synthesis in microreactors, including the types of microreactors used in biodiesel production, the main factors influencing biodiesel synthesis in microreactors, the types of catalysts used, and the application of the microfluidic technique in the purification of biodiesel.

SUN *et al.* [6] reported the transesterification of cottonseed oil and methanol with KOH as the catalyst for biodiesel production in microstructured reactors at residence times of less than 1 minute and high flow rates. The influences of the type of micromixer, the residence time, the methanol-to-oil molar ratio, the flow rate, the type of delay loop, and reaction temperatures below and above the boiling point of methanol were examined. Flow patterns under different conditions were also examined in transparent microtubes. The results indicated that multilaminate micromixers exhibited higher efficiencies in biodiesel production than simple T- and J-type micromixers. A higher yield of biodiesel could be obtained at reaction temperatures above the normal boiling point of methanol.

ABDULLA YUSUF *et al.* [47] investigated the production of biodiesel using waste cooking oil and methanol, with sodium hydroxide as a catalyst. In a four-micro serpentine-based microreactor, biodiesel was produced under varying operating conditions: methanol to oil molar ratio, catalyst concentration, and reaction temperature. The optimum biodiesel yield was 82.8% at a methanol to oil molar ratio of 12 : 1, 1.5 wt% catalyst concentration, and reaction temperature of 59.4 °C while maintaining the reactants' inlet flow rate of 20 $\mu L/s$. The reactants were previously mixed before entering the microreactor.

AGHEL and BIABANI [48] investigated the transesterification of waste cooking oil using TiO2, CuO, and GO as catalysts in solar plain and helical glass microreactors. The authors employed a response surface methodology to optimize biodiesel production. GO catalyst and helical microreactor proved to be the most effective due to their unique geometry. The highest biodiesel purity was achieved with GO at 99.98%, followed by TiO2 at 95.78% and CuO at 93.55%, all with a 3% catalyst dose, 200 s residence time, and oil-to-methanol volume ratio of 2.

SILVA *et al.* [49] addressed challenges in continuous biodiesel production, seeking to overcome limitations of conventional batch reactors, such as biphasic reactions and thermodynamic equilibrium constraints that raised production costs. While microreactors initially demonstrated promise in enhancing mixing and transfer rates at smaller scales, the efficiency and product yield diminished when scaled up. The authors proposed a novel microreactor design that incorporated static mixing elements, an optimized micromixer, an enlarged channel cross-sectional area, and an additional obstacle-free channel. Through a combination of Fractional Design and Central Composite Design, they identified optimal values for the design variables to maximize performance. Simulations showed a high mixing index ($M > 0.77$) across a wide range of Reynolds numbers ($Re = 0.1$–100), achieving conversions over 91% with residence times above 60 s. This approach offered a promising pathway to improve mixing and reactant distribution in industrial-scale biodiesel production, potentially reducing the number of required micro/millidevices.

2.3 Flow Behavior in Microchannels

The hydrodynamic behavior in microchannels is significantly influenced by viscous forces, geometry, and interface phenomena. This section provides an overview of flow regimes, pressure drop characteristics, and the influence of channel dimensions and obstacles. Special attention is given to laminar flows and the development of hydrodynamic entrance regions, which are predominant under microfluidic conditions.

By analyzing various T-shaped micromixer designs — triangular, rectangular, trapezoidal, and circular — under laminar flow conditions, TAJIK GHANBARI *et al.* [50] found that triangular micromixers exhibited the highest mixing performance, with an 8.3% improvement in the mixing index compared to circular designs. While rectangular micromixers underperformed at low Reynolds numbers, their efficiency improved significantly at higher Reynolds numbers ($Re = 20$ and above), attributed to vortex formation, achieving a mixing coefficient of 0.98 at $Re = 40$. Additionally, the introduction of obstacles enhanced mixing efficiency, yielding a 34% improvement over obstacle-free cases. This enhancement was driven by vortex

generation at low Reynolds numbers, with obstacle angles of 90° and 120° being particularly effective in improving mixing proficiency.

Sinusoidal microchannels have gained attention for their ability to enhance mixing performance in droplet-based microfluidic systems. ÖZKAN and ERDEM [51] investigated the impact of particle motion within droplets on the mixing efficiency in sinusoidal geometries. The analysis revealed that the curvature and periodicity of the sinusoidal channel significantly influence droplet deformation and internal recirculation, which are critical for efficient mixing. By comparing various channel designs, the study demonstrated that increasing the channel's sinusoidal amplitude enhances mixing due to stronger vortices and more pronounced droplet interactions. This approach highlights the importance of leveraging channel geometry to achieve improved mixing in microfluidic applications, such as chemical synthesis and biological assays, where precise control over droplet behavior is essential.

WU et al. [52] visualized liquid-liquid flow regimes in three square microchannels. At the inlet junction, three major flow regimes including tubing/threading, dripping, and jetting were mapped using the aqueous capillary number versus the organic Weber number. Correspondingly, in the main microchannel, annular, slug, and droplet flow patterns were mapped using two dimensionless numbers (Weber number times Ohnesorge number) of both phases. Both dripping and jetting regimes at the inlet junction can evolve into either slug or droplet flows in the main microchannel. Besides, it was realized that as the organic flow rate increases, the transitional aqueous flow rate at the slug-droplet transition firstly increases, then decreases, and then increases again. The droplet formation mechanism has transited from dripping to jetting, which causes the slug-droplet transition to occur at a much lower aqueous flow rate.

WIDIANTO et al. [53] explored the use of microreactors to improve mass and heat transfer in heterogeneous chemical processes that are challenging for traditional batch or continuous stirred tank reactors. The authors emphasized that the high specific surface area in microreactors is critical to enhancing mass and heat transfer between phases. In two-phase liquid-liquid flows, the slug flow pattern has been identified as ideal due to its high stability, regular velocity, and uniform dimension across the microchannel. Recognizing this, the authors sought to determine the mass transfer coefficient in liquid-liquid slug flow and assess the effects of slug size, channel material, volumetric flow rate, and flow rate ratio of organic to aqueous phases. They conducted experiments using $1mm$ (internal diameter) circular polytetrafluoroethylene and silicone tubes, at flow rates of 30–40 $ml/hour$, and with sodium hydroxide concentrations of 0.1, 0.13, and 0.15 M. Their findings indicated that the highest mass transfer coefficient, $0.121/s$, was achieved at a 0.15 M concentration of sodium hydroxide with a 40 $ml/hour$ flow rate in the silicone channel.

Additionally, smaller slugs formed at higher aqueous phase flow rates relative to the organic phase, increasing the specific surface area and enhancing the mass transfer coefficient.

2.4 Simulation of Multiphase Flows in Microreactors

In order to understand in detail the reasons why microreactor technology achieves high yields in biodiesel production in very short residence times, several researchers have focused on investigating the factors that influence the conversion of vegetable oil or animal fat into esters during the transesterification reaction in microreactors not only experimentally, but also by means of mathematical models that describe the physical and chemical phenomena involved in biodiesel synthesis in microreactors [2, 11, 47, 49, 54]. In addition to enabling a more detailed understanding of the factors that influence biodiesel synthesis through the modeling and simulation of mass transfer equations, mathematical models are also very important for obtaining suitable conditions in advance to maximize biodiesel production [21].

AL-DHUBABIAN [11] carried out a theoretical and experimental study in a microreactor made of thin glass plates for the synthesis of biodiesel using soybean oil, methanol and NaOH as a catalyst. The flow model proposed in this work was stratified with a fixed fluid interface and adopted a mass transfer model coupled with the reversible second-order chemical reactions developed considering the three consecutive steps of the transesterification reaction shown in 2.2, 2.3 and 2.4. The model was solved using FEMLAB (Finite Element Method Laboratory) software. The kinetic constants (k_i) used in the mathematical model were estimated by adjusting the triglyceride conversions obtained experimentally with the triglyceride conversions obtained with the mathematical model. Using microchannels with heights of 100 and 200 µm, soybean oil conversions of 86 % and 91 % were achieved, respectively, both at a temperature of 25 °C. The results of the experiments were compared with the results of the numerical simulations for different residence times and a good agreement was observed between the experimental data and the numerical simulations, showing that the proposed mathematical model was able to describe the experimental data well.

SANTANA et al. [2] presented simulations of the mixing and reaction of jatropha oil - ethanol in microreactors containing circular obstructions with the aim of evaluating the mixing between species within the microreactors and predicting the best microreactor for biodiesel synthesis. Three different micromixers were studied: a T-shaped microreactor without obstructions, a T-shaped microreactor with

circular obstructions and a T-shaped microreactor with alternating circular obstructions. The geometries and numerical meshes of the microreactors were created using ANSYS ICEM 14.0 software, where tetrahedral elements were used in the discretization. Figure 2.1 shows the geometry of the three microreactors studied in this work. The computer simulation was carried out using the ANSYS CFX - 14.0 software. The mass and momentum conservation equations, together with the kinetic model, which was developed using the global transesterification reaction (Equation 2.1), were solved using the finite volume method. The simulations were carried out varying the Reynolds number from 1 to 160 and the residence time from 0.2 to 100 s. The results show that channels with obstructions improve the interaction between the fluids, and the higher the number of obstructions, the better the mixing efficiency. The T-shaped microreactor with alternating circular obstructions had the highest mixing index (0.99). The authors concluded that the presence of obstacles improves species conversion. Figure 2.2 shows the oil mass fraction, which is the ratio between the mass of oil and the sum of the of the masses of all the constituents of biodiesel synthesis (oil+alcohol+catalyst), and the fluid flow lines for the T-shaped microreactor (Figure 2.2a) and the T-shaped microreactor with obstructions (Figure 2.2b).
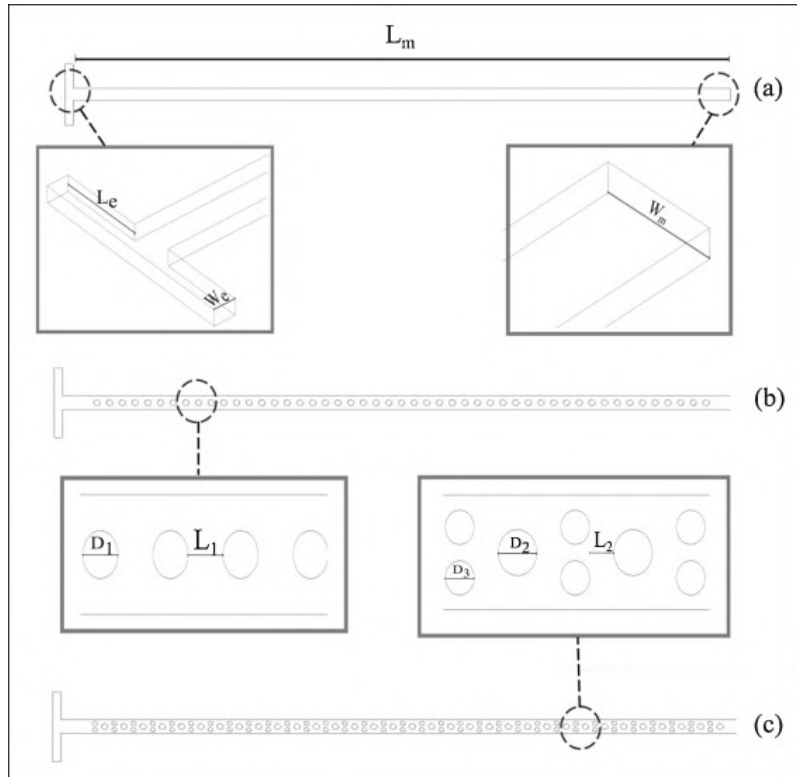
Figure 2.1: Microreactor geometry: (a) T-shaped without obstructions; (b) T-shaped with obstructions; and (c) T-shaped with alternating circular obstructions (SANTANA *et al.* [2]).
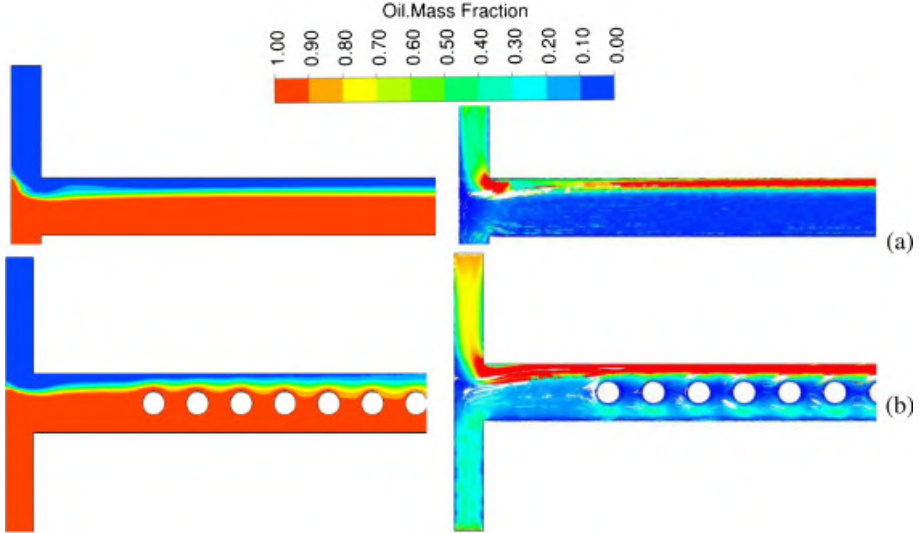
Figure 2.2: Mass fraction and streamlines at $Re = 17$: (a) in T format without obstructions; (b) in T format with obstructions (SANTANA *et al.* [2]).

CHEN and NAVEIRA-COTTA [54] present a theoretical study of the influence of two types of flow on the synthesis of biodiesel in microreactors using soybean oil, methanol and NaOH as a catalyst. The types of flow studied were stratified flow and segmented flow. This problem was modeled using the Navier-Stokes equations and the mass transfer equations coupled with second-order kinetic equations, assuming homogeneous, reversible and elementary chemical reactions. The mathematical model was solved by the finite element method using the COMSOL Multiphysics software. In this work the authors observed that in the microreactor with stratified flow high triglyceride conversions are obtained at high residence times due to the fact that the reactants have more time in chemical contact, while in the microreactor with segmented flow they observed that for different values of bubble size and quantity the triglyceride conversion was very similar. The segmented flow did not take into account the flow inside the bubbles, which would renew the fluid near the interface and probably improve triglyceride conversion. When comparing the types of flow, it was observed that segmented flow achieves a higher triglyceride conversion than stratified flow at short residence times and at long residence times both flows achieve similar conversions.

2.5 Interface Representation Techniques

One approach to simulating two-phase flows is to describe each phase independently. In this case, a set of equations is used for each phase, plus equations to couple them. This ensures the physical consistency of the simulation, but also adds complexity to the model. This method is called the two-fluid model.

An alternative is the one-fluid model. Here, a single set of equations describes the entire domain occupied by the phases. The fluid is treated as one, but properties change abruptly in the interface region. This variation mimics the presence of different phases. Unlike the two-fluid model, this approach does not require coupling equations between the phases. However, it does require adding interfacial tension as a localized force at the interface.

This description can be made based on different methods, which, according to the classification used by UNVERDI and TRYGGVASON [55], can be divided into two main groups: interface-capturing methods, in which the interface is defined implicitly by means of a function that is advected with the flow; and interface-tracking methods, in which the interface is defined explicitly by a set of points.

The main methods of interface-capturing are volume of fluid (VOF) and level-set (LS).

The VOF method, introduced by HIRT and NICHOLS [56], represents the interface through a marker function that varies between 0 and 1 in each mesh element, depending on the fraction of that element occupied by a reference fluid. A value of 1 indicates that the element is fully within the reference fluid, while a value of 0 means it is entirely in the other fluid. Intermediate values, between 0 and 1, correspond to elements located at the interface. In this approach, the interface is not explicitly or sharply defined; instead, only its approximate position is indicated. This feature complicates the calculation of interface curvature and surface tension, limiting the accuracy of the method in certain flows. Nevertheless, the lack of an explicit interface representation can also be advantageous. For flows with frequent topological changes—such as bubble coalescence or droplet breakup—the method avoids the need to explicitly track these complex events. Instead, they are naturally captured through the marker function, which evolves automatically at each time step. Moreover, the VOF method is recognized for ensuring good mass conservation of both fluids.

Accurate flow measurement in microchannels is essential for understanding flow behavior and informing the design of microfluidic devices. To address limitations in numerical accuracy, particularly those arising from spurious velocities in simulations, SOH *et al.* [57, 58] proposed a modified Volume of Fluid (VOF) model incorporating smoothing functions. This improved model effectively reduces spurious velocity artifacts that typically distort velocity fields and droplet dynamics in standard VOF simulations. The smoothed VOF approach was used to simulate velocity profiles and droplet lengths in microchannels, with results validated against experimental data. Comparisons demonstrate that the smoothed VOF outperforms the standard model, which tends to generate artificially high velocity regions and non-physical shear stresses, leading to premature droplet formation and reduced droplet lengths.

By mitigating these numerical artifacts, the smoothed VOF model provides a more accurate and reliable tool for simulating microchannel flows.

The LS method, introduced by SUSSMAN *et al.* [59], also represents the interface using a marker function. Unlike VOF, this marker function is defined as a signed distance function, taking positive values in the region occupied by one fluid and negative values in the region of the other. The interface itself corresponds to the zero level of this function. As in the VOF approach, the interface is advected with the flow through the transport of the marker function. However, the LS method exhibits characteristics that are complementary to those of VOF: it enables accurate computation of interface curvature and surface tension, but it suffers from difficulties in maintaining strict mass conservation of each fluid.

The LS method has proven to be a robust approach for representing interfaces in multiphase flows, particularly in scenarios involving heat and mass transfer. BALCÁZAR-ARCINIEGA *et al.* [60] introduced a conservative level-set (CLS) model to simulate interfacial mass transfer in bubbly flows using a finite-volume method on unstructured meshes. The CLS approach effectively maintains a sharp fluid interface while preventing nonphysical coalescence of bubbles, a common issue in interface-capturing methods. By combining flux-limiters to minimize numerical diffusion and an adaptive mesh refinement technique to enhance resolution near interfaces, the model offers accurate predictions of mass transfer phenomena. The authors also validated the methodology against analytical solutions and empirical correlations, demonstrating its reliability for applications involving complex interfacial dynamics.

MORA *et al.* [61] investigated droplet breakup in T-junction microchannels to improve microreactor and microfluidic device designs, using coupled volume of fluid and level-set methods (S-CLSVOF) in OpenFOAM for 3D simulations. They analyzed the droplet morphology and rupture regimes in varying capillary numbers and initial droplet lengths, focusing on the thickness of the neck, the width of the tunnel, and the local pressure. The results identified four different rupture regimes, providing information on the stages of droplet breakup and the role of Laplace pressure in determining rupture points. A notable backflow near the neck region, characterized by pressure drops, was observed just before the breakup, leading to reduced breakup times.

In light of the advances and limitations discussed in this section, the present work contributes by developing a numerical methodology capable of simulating miscible two-phase flow in microreactors with realistic geometries relevant to biodiesel synthesis. The miscible flow assumption simplifies interface representation while still accounting for the influence of distinct phases on the velocity and pressure fields. The finite element method, combined with a semi-Lagrangian discretization that ensures

15

stability for convection-dominated transport problems, was employed. This framework enables the direct resolution of the incompressible Navier–Stokes equations coupled with the convection–diffusion equation, capturing the intricate interplay between hydrodynamic instabilities, molecular diffusion, and viscosity variations that govern miscible displacement. By systematically investigating both simple and obstacle-based microchannel configurations, this study not only extends the numerical modeling strategies found in the literature but also provides new insights into the trade-offs between mixing efficiency and hydrodynamic performance, offering valuable guidelines for the design of compact and sustainable biodiesel production technologies.

Chapter 3

Methodology

This chapter discusses the foundations of the theory that supports the study of this project. Here, hypotheses and parameters of the problem studied are presented, as well as elaborating the main governing equations and boundary conditions, mainly those governing fluid mechanics and mass transfer.

This chapter is subdivided into six sections, each dealing with one of the central points of the proposed methodology:

- Governign Equations;

- Boundary and Initial Conditions;

- Finite Element Method;

- The Semi-Lagrangian Method;

- Problem Formulation and Resolution;

- Computational Implementation.

3.1   Governing Equations

This section introduces the equations governing the motion of two miscible fluids, separated by a non-defined interface. In multi-phase flow, the motion can be described using two distinct approaches. The first, known as the "one-fluid" formulation, treats both fluid phases as a single fluid with variable properties across the domain, which change at the interface. The second approach considers each phase as a separate fluid, with each governed by its own set of equations and boundary conditions at the interface. This study employs the "one-fluid" formulation, and the equations in this chapter are presented accordingly. In the following section, the equations are reformulated in a non-dimensional form, incorporating known dimensionless groups [62] [63].

The following analysis relies on several key assumptions. First, the fluid motion is assumed to be isothermal, meaning that temperature effects are neglected. Additionally, the conservation of mass and momentum principles govern the fluid's behavior. By applying the constitutive equation for a Newtonian fluid within the momentum conservation equation, we obtain the Navier-Stokes equations. These equations are further simplified by assuming an incompressible fluid, which eliminates density variations with pressure [64]. Under these assumptions, we present the resulting simplified form below, beginning with the conservation of mass equation.

$$\nabla \cdot \mathbf{v} = 0 \tag{3.1}$$

where $\mathbf{v}$ represents velocity [m/s]. Then, we present the conservation of momentum equation for a Newtonian fluid.

$$\rho(\mathbf{x}) \left(\frac{\partial \mathbf{v}}{\partial t} + \mathbf{v} \cdot \nabla \mathbf{v} \right) = -\nabla p + \nabla \cdot \left[\mu(\mathbf{x})(\nabla \mathbf{v} + \nabla \mathbf{v}^T) \right] \tag{3.2}$$

where t is the time [s], p is the pressure [N/m^2], and $\rho(\mathbf{x})$ is the fluid density at the point x [kg/m^3]. Likewise, and $\mu(\mathbf{x})$ is the fluid viscosity [N $\cdot$ s/m^2].

In addition, the species transport equation governs the evolution of the concentration (or mass fraction) of each component involved in the system, accounting for advection, diffusion, and reaction effects. The general dimensional form of the species transport equation for species i is given by:

$$\frac{\partial c_s}{\partial t} + \mathbf{v} \cdot \nabla c_s = D_s \nabla^2 c_s + \dot{R}_s, \tag{3.3}$$

where c_s is the molar concentration of species s, D_s is the diffusion coefficient of species s [m^2/s], which is assumed to be constant, and $\dot{R}_s$ is the source term due to chemical reaction [mol/(m^3·s)], and is related to 2.5.

These equations can be rewritten into their non-dimensional form, replacing their dimensional units with their non-dimensional form as given by

$$\mathbf{v}^* = \frac{\mathbf{v}}{V}, \quad x^* = \frac{x}{L}, \quad t^* = \frac{tV}{L}, \quad p^* = \frac{p}{\rho_d V^2}, \quad \rho^* = \frac{\rho}{\rho_d}, \quad \mu^* = \frac{\mu}{\mu_d} \tag{3.4}$$

$$\nabla^* = \nabla L, \quad c_s^* = \frac{c_s}{c_0}, \tag{3.5}$$

where L and V refer to characteristic length and characteristic velocity, respectively. The superscript $*$ refers to non-dimensional quantities, and the subscript d refers to the denser fluid property, be it specific mass or viscosity.

Replacing the non-dimensional parameters in 3.1, one obtains:

18

$$\frac{V}{L}\nabla^* \cdot \mathbf{v}^* = 0 \tag{3.6}$$

which can then be simplified to result in

$$\nabla^* \cdot \mathbf{v}^* = 0 \tag{3.7}$$

The non-dimensional form of the momentum equation can be derived by substituting the dimensionless variables into 3.2. Following this procedure yields the following expression:

$$\rho_0\rho^* \left[\frac{V^2}{L}\frac{\partial \mathbf{v}^*}{\partial t^*} + \frac{V^2}{L}\mathbf{v}^* \cdot \nabla^*\mathbf{v}^* \right] = -\frac{\rho_0 V^2}{L}\nabla^* p^*$$
$$+ \frac{\mu_0 V}{L^2}\nabla^* \cdot \left[\mu^* \left(\nabla^*\mathbf{v}^* + \nabla^*\mathbf{v}^{*T} \right) \right] \tag{3.8}$$

which after being multiplied by $L/\rho_d V^2$, results in

$$\rho(\mathbf{x})^* \left(\frac{\partial \mathbf{v}^*}{\partial t^*} + \mathbf{v}^* \cdot \nabla^*\mathbf{v}^* \right) = -\nabla^* p^* + \frac{\mu_d}{\rho_d V L}\nabla^* \cdot \mu(\mathbf{x})^* \left[\nabla^*\mathbf{v}^* + (\nabla^*\mathbf{v}^*)^T \right] \tag{3.9}$$

Following the same procedure in 3.3, one obtains

$$\frac{c_0 V}{L}\frac{\partial c_s^*}{\partial t} + \frac{c_0 V}{L}\mathbf{v}^* \cdot \nabla c_s^* = \frac{c_0 D_s}{L^2}\nabla^2 c_s^* + \dot{R}_s \tag{3.10}$$

which is multiplied by $L/V c_0$, to obtain

$$\frac{\partial c_s^*}{\partial t} + \mathbf{v} \cdot \nabla c_s^* = \frac{D_s}{V L}\nabla^2 c_s^* + \frac{L}{V c_0}\dot{R}_s \tag{3.11}$$

This formulation includes four dimensionless parameters, whose definitions are set out below:

Reynolds Number

The Reynolds number (Re) represents the ratio between inertial forces and viscous forces in a flow, and is defined by 3.12 [65, 66].

$$Re = \frac{\rho_d V L}{\mu_d} \tag{3.12}$$

Péclet Number

The Péclet number (Pe) represents the ratio of advective transport rate to diffusion transport rate, and is defined by 3.13 [67].

$$\text{Pe} = \frac{VL}{D} \tag{3.13}$$

First Damköhler Number

The first Damköhler number (Da_{Is}) represents the ratio of a transport time to a reaction time, and is defined by 3.14 [68, 69].

$$Da_{Is} = \frac{L\dot{R}_s}{Vc_0} \tag{3.14}$$

Substituting the Reynolds and Froude numbers in 3.9, and the Péclet and Damköhler numbers in 3.11, and removing the asterisks for simplicity of notation, we obtain the final formulation of the governing equations, given by 3.15 and 3.16.

$$\rho(\mathbf{x})\left(\frac{\partial \mathbf{v}}{\partial t} + \mathbf{v} \cdot \nabla \mathbf{v}\right) = -\nabla p + \frac{1}{Re}\nabla \cdot \mu(\mathbf{x})\left[\nabla \mathbf{v} + (\nabla \mathbf{v})^T\right] \tag{3.15}$$

$$\frac{\partial c_s}{\partial t} + \mathbf{v} \cdot \nabla c_s = \frac{1}{Pe_s}\nabla^2 c_s + Da_{Is} \tag{3.16}$$

Specific mass and dynamic viscosity are assumed to be related to c_s by [70, 71]

$$\rho = \sum_{i=1}^{n} c_{s,i}\rho_{s,i} \tag{3.17}$$

$$\mu = \exp\left(\sum_{i=1}^{n} c_{s,i}\ln\mu_{s,i}\right) \tag{3.18}$$

3.2   Boundary and Initial Conditions

For a differential equation to have a unique solution, it needs to be well-posed with defined boundary conditions. These conditions act as constraints. They specify known values at certain points, reducing the range of possible solutions.

In fluid dynamics, one common boundary condition occurs near a stationary solid surface. If the solid is non-porous, the fluid cannot enter it. As a result, the fluid's velocity perpendicular to the surface is zero. The fluid's velocity parallel to the surface is also zero, due to viscosity. This no-slip behavior has been confirmed experimentally in macroscopic flows [72].

Initial conditions set the state of the system and the values of field variables at the starting time.

When solving numerically, boundary and initial conditions should match these physical properties. Boundary conditions are classified as Dirichlet, prescribing the solution's value at the boundary, or Neumann, prescribing the derivative of the solution at the boundary [73].

Here follows the description of the boundary conditions used in the present work:

- **No-slip**: The no-slip condition sets all velocity components to zero at the surface, meaning the fluid does not slip along the wall.

- **Slip at walls in microchannels**: At micro- and nano-scales, experimental evidence has demonstrated that the no-slip hypothesis may not always hold. Instead, a finite slip velocity can occur at the wall, typically modeled through the Navier slip condition, where the tangential velocity at the wall is proportional to the shear rate. This effect becomes significant when the Knudsen number, Kn, is not negligible, as is the case in microfluidic systems. The slip length depends on surface roughness, wettability, and fluid–wall interactions [74–76].

- **Inflow**: The inflow condition specifies a prescribed velocity, setting the fluid's velocity to desired values. It represents the entry of mass into the domain.

- **Outflow**: The outflow condition is a prescribed pressure condition, where the pressure is set to zero. This models the exit of mass from the domain.

- **Species concentration**: For the transported chemical species, a Dirichlet condition was imposed at the inlet, prescribing fixed concentrations for triglyceride and alcohol according to the inlet molar ratios considered. At the channel walls (upper and lower boundaries), homogeneous Neumann conditions were applied, ensuring zero diffusive flux normal to the walls. At the outlet, a Neumann condition was also used, allowing the concentration field to develop freely without imposing artificial gradients.

3.3 Finite Element Method

The finite element method is a powerful computational tool used to address differential and integral equations, especially in engineering fields. It's popular for handling complex scenarios in fluid dynamics, heat transfer, structural analysis, and other areas, as it delivers highly accurate approximations where analytical solutions are challenging or impossible.

This technique works by breaking down the domain of the problem into small, finite regions known as elements, which are connected at designated points called nodes. These elements come in various shapes, such as line segments, triangles, quadrilaterals, or tetrahedrons, and can exist in one, two, or three dimensions. The finite element method relies on a weighted residual or variational approach to approximate the differential equation's solution at the nodes. This approach involves multiplying the differential equation by a test function and integrating across the domain. Rather than requiring zero error across the entire domain, it instead minimizes the error integral, or residuum, to zero for an acceptable solution.

The flexibility of the finite element method allows it to handle intricate geometries and complex boundary conditions, as the elements do not need to conform to specific shapes. This adaptability enables it to represent irregular domains and non-uniform boundary conditions effectively.

3.3.1 Variational Formulation

To apply the Finite Element Method, it is necessary to obtain the variational or weak formulation of these equations, as described by DONEA and HUERTA [77]. This process starts from the non-dimensional Navier-Stokes and species transport equations given by 3.19, 3.20 and 3.21.

$$\nabla \cdot \mathbf{v} = 0 \tag{3.19}$$

$$\rho(\mathbf{x}) \left(\frac{\partial \mathbf{v}}{\partial t} + \mathbf{v} \cdot \nabla \mathbf{v} \right) = -\nabla p + \frac{1}{Re} \nabla \cdot \mu(\mathbf{x}) \left(\nabla \mathbf{v} + (\nabla \mathbf{v})^T \right) \tag{3.20}$$

$$\frac{\partial c_s}{\partial t} + \mathbf{v} \cdot \nabla c_s = \frac{1}{Pe_s} \nabla^2 c_s + Da_{Is} \tag{3.21}$$

For this formulation, a validity domain given by $\Gamma = \Gamma_1 \cup \Gamma_2 \cup \Gamma_3$ will be considered, along with the boundary conditions given by 3.22, 3.23 and 3.24. The first condition characterizes a prescribed velocity and zero pressure gradient on the boundary Γ_1, while the second addresses a condition of prescribed zero pressure and zero velocity gradient on the boundary Γ_2. Additionally, the third addresses a prescribed species concentration on the boundary Γ_3. These three generalized formulations encompass the types of boundary conditions used throughout this work, as listed in the previous section.

$$\mathbf{v} = \mathbf{v_\Gamma} \quad \text{on } \Gamma_1 \tag{3.22}$$

$$p = 0 \quad \text{on } \Gamma_2 \tag{3.23}$$

$$c_s = c_{s\Gamma} \quad \text{on } \Gamma_3 \tag{3.24}$$

Let $L^2(\Omega)$ be the space of quadratically integrable functions over the domain Ω, given by 3.25.

$$L^2(\Omega) = \left\{ v : \Omega \to \mathbb{R}, \int_\Omega v^2 \, d\Omega < \infty \right\} \tag{3.25}$$

Let's also take the Sobolev space $H^1(\Omega)$, given by 3.26, and its analog $H^1(\Omega)^n$ for n-dimensional vectors, given by the Cartesian product between $nH^1(\Omega)$ spaces, according to 3.27.

$$H^1(\Omega) = \left\{ v \in L^2(\Omega) : \frac{\partial v}{\partial x_i} \in L^2(\Omega), \, i = 1, 2, \ldots, n \right\} \tag{3.26}$$

$$H^1(\Omega)^n = \left\{ \mathbf{v} = (v_1, v_2, \ldots, v_n) : v_i \in H^1(\Omega), \, i = 1, 2, \ldots, n \right\} \tag{3.27}$$

Let the subspaces $V_{v_\Gamma}(\Omega)$, $P_{p_\Gamma}(\Omega)$ and $C_{c_{s\Gamma}}(\Omega)$ be defined by 3.28, 3.29 and 3.30 where Γ_1, Γ_2 and Γ_3 are the velocity, pressure and species concentration contours respectively.

$$V_{\mathbf{v}_\Gamma}(\Omega) = \{ \mathbf{v} \in H^1(\Omega)^n : \mathbf{v} = \mathbf{v}_\Gamma \text{ on } \Gamma_1 \} \tag{3.28}$$

$$P_{p_\Gamma}(\Omega) = \{ p \in H^1(\Omega) : p = p_\Gamma \text{ on } \Gamma_2 \} \tag{3.29}$$

$$C_{c_{s\Gamma}}(\Omega) = \{ c_s \in H^1(\Omega) : c_s = c_{s\Gamma} \text{ on } \Gamma_3 \} \tag{3.30}$$

The variational formulation of the Navier-Stokes and species transport equations is obtained by multiplying 3.20, 3.19 and 3.21 by the weight functions $\mathbf{w}$, q and η, respectively, as shown in 3.31, 3.32 and 3.33.

$$\int_\Omega \nabla \cdot \mathbf{v} \, q \, d\Omega = 0 \tag{3.31}$$

$$\int_\Omega \left\{ \rho(x) \left[\frac{\partial \mathbf{v}}{\partial t} + \mathbf{v} \cdot \nabla \mathbf{v} \right] + \nabla p - \frac{1}{Re} \nabla \cdot [\mu(x)(\nabla \mathbf{v} + \nabla \mathbf{v}^T)] \right\} \cdot \mathbf{w} \, d\Omega = 0 \tag{3.32}$$

$$\int_\Omega \left\{ \frac{\partial c_s}{\partial t} + \mathbf{v} \cdot \nabla c_s - \frac{1}{Pe_s} \nabla^2 c_s - Da_{Is} \right\} \cdot \eta \, d\Omega = 0 \tag{3.33}$$

Due to the distributivity of the inner product, 3.32 and 3.33 becomes 3.34 and 3.35.

$$\int_{\Omega} \left\{ \rho(x) \left[\frac{\partial \mathbf{v}}{\partial t} + \mathbf{v} \cdot \nabla \mathbf{v} \right] \right\} \cdot \mathbf{w} \, d\Omega + \int_{\Omega} \{ \nabla p \} \cdot \mathbf{w} \, d\Omega$$
$$- \int_{\Omega} \left\{ \frac{1}{Re} \nabla \cdot [\mu(x)(\nabla \mathbf{v} + \nabla \mathbf{v}^T)] \right\} \cdot \mathbf{w} \, d\Omega = 0 \quad (3.34)$$

$$\int_{\Omega} \left\{ \frac{\partial c_s}{\partial t} + \mathbf{v} \cdot \nabla c_s \right\} \eta \, d\Omega - \int_{\Omega} \left\{ \frac{1}{Pe_s} \nabla^2 c_s \right\} \eta \, d\Omega - \int_{\Omega} Da_{Is} \eta \, d\Omega = 0 \quad (3.35)$$

Using the definition of material derivative, the advective term in 3.34 and 3.35 can be rewritten as 3.36 and 3.37.

$$\int_{\Omega} \rho \left[\frac{\partial \mathbf{v}}{\partial t} + \mathbf{v} \cdot \nabla \mathbf{v} \right] \cdot \mathbf{w} \, d\Omega = \int_{\Omega} \rho \frac{D\mathbf{v}}{Dt} \cdot \mathbf{w} \, d\Omega \quad (3.36)$$

$$\int_{\Omega} \left\{ \frac{\partial c_s}{\partial t} + \mathbf{v} \cdot \nabla c_s \right\} \eta \, d\Omega = \int_{\Omega} \frac{Dc_s}{Dt} \eta \, d\Omega \quad (3.37)$$

Applying Green's Theorem, the integral of the diffusive term in 3.34 and 3.35 can be rewritten as 3.38 and 3.39.

$$- \int_{\Omega} \left\{ \frac{1}{Re} \nabla \cdot [\mu(x)(\nabla \mathbf{v} + \nabla \mathbf{v}^T)] \right\} \cdot \mathbf{w} \, d\Omega = \frac{1}{Re} \int_{\Omega} \mu(x) \left[(\nabla \mathbf{v} + \nabla \mathbf{v}^T) : \nabla \mathbf{w}^T \right] \, d\Omega$$
$$- \frac{1}{Re} \int_{\Gamma} \mathbf{n} \cdot \left[\mu(x)(\nabla \mathbf{v} + \nabla \mathbf{v}^T) \cdot \mathbf{w} \right] \, d\Gamma \quad (3.38)$$

$$- \int_{\Omega} \left\{ \frac{1}{Pe_s} \nabla^2 c_s \right\} \eta \, d\Omega = \frac{1}{Pe_s} \int_{\Omega} \nabla c_s \cdot \nabla \eta \, d\Omega - \frac{1}{Pe_s} \int_{\Gamma} \eta \nabla c_s \cdot \, d\Gamma \quad (3.39)$$

Furthermore, it can be said that the boundary integrals Γ in 3.38 and 3.39 are null, since it can be broken down into a sum of two null integrals: one on the boundary Γ_1, where $\mathbf{w} = 0$, and Γ_3, where $\eta = 0$ and another on the boundary Γ_2, where the nullity derives from the boundary condition itself.

Similarly, applying Green's Theorem, the pressure term can be rewritten as 3.40.

$$\int_{\Omega} \nabla p \cdot \mathbf{w} \, d\Omega = - \int_{\Omega} p \nabla \cdot \mathbf{w} \, d\Omega + \int_{\Gamma} p(\mathbf{w} \cdot \mathbf{n}) \, d\Gamma \quad (3.40)$$

It can be said that the boundary integral Γ in 3.40 is also null, since it can also

be broken down into a sum of two null integrals: one on the Γ_1 boundary, where $\mathbf{w} = \mathbf{0}$, and another on the Γ_2 boundary, where $p = 0$.

Thus, the variational formulation of the Navier-Stokes equations is given by 3.41, 3.42 and 3.43.

$$\int_\Omega (\nabla \cdot \mathbf{v}) \, q d\Omega = 0 \tag{3.41}$$

$$\int_\Omega \rho(x)\frac{D\mathbf{v}}{Dt} \cdot \mathbf{w} \, d\Omega - \int_\Omega p\nabla \cdot \mathbf{w} \, d\Omega + \frac{1}{Re} \int_\Omega \mu(x) \left[(\nabla\mathbf{v} + \nabla\mathbf{v}^T) : \nabla\mathbf{w}^T\right] \, d\Omega = 0 \tag{3.42}$$

$$\int_\Omega \frac{Dc_s}{Dt}\eta \, d\Omega + \frac{1}{Pe_s} \int_\Omega \nabla c_s \cdot \nabla\eta \, d\Omega - \int_\Omega Da_{Is}\eta \, d\Omega = 0 \tag{3.43}$$

The problem consists of finding the solutions $\mathbf{v}(\mathbf{x}, t) \in V_{\mathbf{v}_\Gamma}(\Omega)$, $p(\mathbf{x}, t) \in P_{p_\Gamma}(\Omega)$ and $c(\mathbf{x}, t) \in C_{c_\Gamma}(\Omega)$ that satisfy 3.42, 3.41 and 3.43 for all $\mathbf{w} \in V_{\mathbf{0}}(\Omega)$, for all $q \in P_0(\Omega)$ and for all $\eta \in C_{c_\Gamma}(\Omega)$.

3.3.2   Galerkin Method

Let's discretize the Ω domain into a mesh with NE triangular elements, NV velocity nodes and NP pressure nodes, as shown in Figure 3.1.
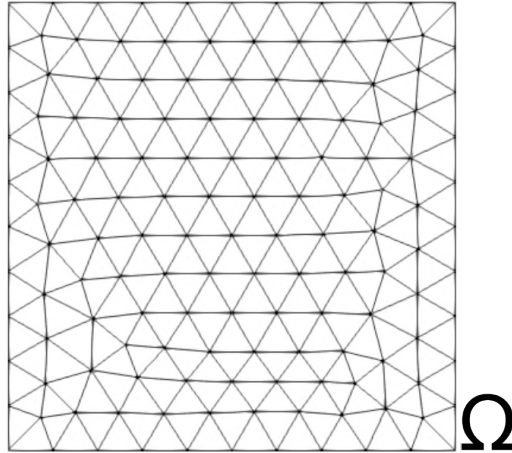
Figure 3.1: Discretization of a domain into triangular elements.

The Galerkin method consists of approximating the continuous variables of the problem into discrete variables in space, using the approximations 3.44, 3.45, 3.46, 3.47 and 3.48. The terms N_i and P_j are called interpolation functions and are used to construct the velocity, pressure and species concentration fields, respectively, from the values of these fields at the mesh nodes [78].

$$v_x(\mathbf{x}, t) \approx \sum_{n=1}^{NV} N_n(\mathbf{x}) v_{x,n}(t) \tag{3.44}$$

$$v_y(\mathbf{x}, t) \approx \sum_{n=1}^{NV} N_n(\mathbf{x}) v_{y,n}(t) \tag{3.45}$$

$$p(\mathbf{x}, t) \approx \sum_{r=1}^{NP} P_r(\mathbf{x}) p_r(t) \tag{3.46}$$

$$c_s(\mathbf{x}, t) \approx \sum_{n=1}^{NV} N_n(\mathbf{x}) c_s(t) \tag{3.47}$$

$$Da_{Is}(\mathbf{x}, t) \approx \sum_{n=1}^{NV} N_n(\mathbf{x}) Da_{Is}(t) \tag{3.48}$$

Finally, for the discretization of the density and viscosity of the fluid, the average values of these properties in each element of the mesh, ρ_e and μ_e, are calculated. To do this, the values of these properties at the three vertices of the triangle are considered, as shown in 3.49 and 3.50.

$$\rho_e = \frac{1}{3}(\rho_{e1} + \rho_{e2} + \rho_{e3}) \tag{3.49}$$

$$\mu_e = \frac{1}{3}(\mu_{e1} + \mu_{e2} + \mu_{e3}) \tag{3.50}$$

Thus, the density and viscosity fields can be discretized spatially, based on their average values in each element, according to 3.51 and 3.52.

$$\rho(\mathbf{x}, t) \approx \sum_{e=1}^{NE} \rho_e(\mathbf{x}, t) \tag{3.51}$$

$$\mu(\mathbf{x}, t) \approx \sum_{e=1}^{NE} \mu_e(\mathbf{x}, t) \tag{3.52}$$

Considering the Navier-Stokes equations 3.19, 3.20 and the species transport equation 3.21, in a two-dimensional domain, where $\mathbf{v} = (v_x, v_y)$ and $\mathbf{w} = (w_x, w_y)$, and substituting the continuous variables for the discretized variables obtained above, we obtain 3.53, 3.54, 3.55 and 3.56. The weight functions w_x and w_y were replaced by the interpolation functions $N_m(\mathbf{x})$, $m = 1, 2, ..., NV$, since the equations of conservation of quantity of movement are evaluated at the velocity nodes. Similarly for the weight function η for the species transport equation. The weight function q has been replaced by the interpolation functions $P_r(\mathbf{x})$, $r = 1, 2, ..., NP$,

since the mass conservation equation is evaluated at the pressure nodes.

$$\sum_{e=1}^{NE} \int_{\Omega^e} \sum_{n=1}^{NP} \left(\frac{\partial N_n}{\partial x} v_{x,n} + \frac{\partial N_n}{\partial y} v_{y,n} \right) P_r \, d\Omega = 0 \tag{3.53}$$

$$\sum_{e=1}^{NE} \int_{\Omega^e} \sum_{n=1}^{NV} \rho^e \frac{Dv_{x,n}}{Dt} N_m N_n \, d\Omega - \sum_{e=1}^{NE} \int_{\Omega^e} \sum_{r=1}^{NP} \frac{\partial N_m}{\partial x} P_r p_r \, d\Omega$$
$$+ \frac{1}{Re} \sum_{e=1}^{NE} \int_{\Omega^e} \sum_{n=1}^{NV} \mu^e \left[\frac{\partial N_m}{\partial x} \frac{\partial N_n}{\partial x} v_{x,n} + \frac{\partial N_m}{\partial y} \frac{\partial N_n}{\partial y} v_{x,n} + \frac{\partial N_m}{\partial x} \frac{\partial N_n}{\partial x} v_{y,n} \right. \tag{3.54}$$
$$\left. + \frac{\partial N_m}{\partial y} \frac{\partial N_n}{\partial x} v_{y,n} \right] d\Omega = 0$$

$$\sum_{e=1}^{NE} \int_{\Omega^e} \sum_{n=1}^{NV} \rho^e \frac{Dv_{y,n}}{Dt} N_m N_n \, d\Omega - \sum_{e=1}^{NE} \int_{\Omega^e} \sum_{r=1}^{NP} \frac{\partial N_m}{\partial y} P_r p_r \, d\Omega$$
$$+ \frac{1}{Re} \sum_{e=1}^{NE} \int_{\Omega^e} \sum_{n=1}^{NV} \mu^e \left[\frac{\partial N_m}{\partial x} \frac{\partial N_n}{\partial x} v_{y,n} + \frac{\partial N_m}{\partial y} \frac{\partial N_n}{\partial y} v_{y,n} + \frac{\partial N_m}{\partial x} \frac{\partial N_n}{\partial y} v_{x,n} \right. \tag{3.55}$$
$$\left. + \frac{\partial N_m}{\partial y} \frac{\partial N_n}{\partial y} v_{y,n} \right] d\Omega = 0$$

$$\sum_{e=1}^{NE} \int_{\Omega^e} \sum_{n=1}^{NV} \frac{Dc_{s,n}}{Dt} N_m N_n \, d\Omega \quad + \frac{1}{Pe_i} \sum_{e=1}^{NE} \int_{\Omega^e} \sum_{n=1}^{NV} \left[\frac{\partial N_m}{\partial x} \frac{\partial N_n}{\partial x} c_{s,n} + \frac{\partial N_m}{\partial y} \frac{\partial N_n}{\partial y} c_{s,n} \right] d\Omega$$
$$- \sum_{e=1}^{NE} \int_{\Omega^e} \sum_{n=1}^{NV} N_m N_n Da_{Is,n} d\Omega = 0 \tag{3.56}$$

By restricting the interpolation functions to each element, equations 3.53, 3.54, 3.55 and 3.56 are converted into 3.57, 3.58, 3.59 and 3.60.

$$\sum_{e=1}^{NE} \int_{\Omega_e} \sum_{j,k \in e} \left(\frac{\partial N_j^e}{\partial x} v_{x,j} + \frac{\partial N_j^e}{\partial y} v_{y,j} \right) P_k \, d\Omega = 0 \tag{3.57}$$

$$\sum_{e=1}^{NE} \int_{\Omega_e} \sum_{i,j\in e} \rho^e \frac{Dv_{x,j}}{Dt} N_i^e N_j^e \, d\Omega - \sum_{e=1}^{NE} \int_{\Omega_e} \sum_{i,k\in e} \frac{\partial N_i^e}{\partial x} P_k p_k \, d\Omega$$

$$+ \frac{1}{Re} \sum_{e=1}^{NE} \int_{\Omega_e} \sum_{i,j\in e} \mu^e \left(\frac{\partial N_i^e}{\partial x} \frac{\partial N_j^e}{\partial x} v_{x,j} + \frac{\partial N_i^e}{\partial y} \frac{\partial N_j^e}{\partial y} v_{x,j} \right) d\Omega$$

$$= 0 \quad (3.58)$$

$$\sum_{e=1}^{NE} \int_{\Omega_e} \sum_{i,j\in e} \rho^e \frac{Dv_{y,j}}{Dt} N_i^e N_j^e \, d\Omega - \sum_{e=1}^{NE} \int_{\Omega_e} \sum_{i,k\in e} \frac{\partial N_i^e}{\partial y} P_k p_k \, d\Omega$$

$$+ \frac{1}{Re} \sum_{e=1}^{NE} \int_{\Omega_e} \sum_{i,j\in e} \mu^e \left(\frac{\partial N_i^e}{\partial x} \frac{\partial N_j^e}{\partial x} v_{y,j} + \frac{\partial N_i^e}{\partial y} \frac{\partial N_j^e}{\partial y} v_{y,j} \right) d\Omega$$

$$= 0 \quad (3.59)$$

$$\sum_{e=1}^{NE} \int_{\Omega^e} \sum_{i,j\in e} \frac{Dc_{s,j}}{Dt} N_i^e N_j^e \, d\Omega \quad + \frac{1}{Pe_i} \sum_{e=1}^{NE} \int_{\Omega^e} \sum_{i,j\in e} \left[\frac{\partial N_i^e}{\partial x} \frac{\partial N_j^e}{\partial x} c_{s,j} + \frac{\partial N_i^e}{\partial y} \frac{\partial N_j^e}{\partial y} c_{s,j} \right] d\Omega$$

$$- \sum_{e=1}^{NE} \int_{\Omega^e} \sum_{i,j\in e} N_i^e N_j^e Da_{Is,j} d\Omega = 0 \quad (3.60)$$

Equations 3.57, 3.58 and 3.59 can be written in the form of the system of equations 3.61, where $\dot{\mathbf{v}}_{\mathbf{x}} = \left[\frac{\partial v_{x,1}}{\partial t}, \ldots, \frac{\partial v_{x,NV}}{\partial t} \right]^T$, $\dot{\mathbf{v}}_{\mathbf{y}} = \left[\frac{\partial v_{y,1}}{\partial t}, \ldots, \frac{\partial v_{y,NV}}{\partial t} \right]^T$, $\mathbf{v}_{\mathbf{x}} = [v_{x,1}, \ldots, v_{x,NV}]^T$, $\mathbf{v}_{\mathbf{y}} = [v_{y,1}, \ldots, v_{y,NV}]^T$, $\mathbf{p} = [p_1, \ldots, p_{NP}]^T$, $\mathbf{g}_{\mathbf{x}} = [g_{x,1}, \ldots, g_{x,NV}]^T$, and $\mathbf{g}_{\mathbf{y}} = [g_{y,1}, \ldots, g_{y,NV}]^T$

$$\begin{cases} \mathbf{M}_{\rho,\mathbf{x}} \dot{\mathbf{v}}_{\mathbf{x}} + \frac{1}{Re} \left[(2\mathbf{K}_{\mathbf{xx}} + \mathbf{K}_{\mathbf{yy}}) \mathbf{v}_{\mathbf{x}} + \mathbf{K}_{\mathbf{xy}} \mathbf{v}_{\mathbf{y}} \right] - \mathbf{G}_{\mathbf{x}} \mathbf{p} = \mathbf{0} \\[2mm] \mathbf{M}_{\rho,\mathbf{y}} \dot{\mathbf{v}}_{\mathbf{y}} + \frac{1}{Re} \left[\mathbf{K}_{\mathbf{yx}} \mathbf{v}_{\mathbf{x}} + (\mathbf{K}_{\mathbf{xx}} + 2\mathbf{K}_{\mathbf{yy}}) \mathbf{v}_{\mathbf{y}} \right] - \mathbf{G}_{\mathbf{y}} \mathbf{p} = \mathbf{0} \quad (3.61) \\[2mm] \mathbf{D}_{\mathbf{x}} \mathbf{v}_{\mathbf{x}} + \mathbf{D}_{\mathbf{y}} \mathbf{v}_{\mathbf{y}} = \mathbf{0} \end{cases}$$

The global matrices $\mathbf{M}_{\rho,\mathbf{x}}$, $\mathbf{M}_{\rho,\mathbf{y}}$, $\mathbf{M}_{\mathbf{x}}$, $\mathbf{M}_{\mathbf{y}}$, $\mathbf{K}_{\mathbf{xx}}$, $\mathbf{K}_{\mathbf{yy}}$, $\mathbf{K}_{\mathbf{xy}}$, $\mathbf{K}_{\mathbf{yx}}$, $\mathbf{G}_{\mathbf{x}}$, $\mathbf{G}_{\mathbf{y}}$, $\mathbf{D}_{\mathbf{x}}$ and $\mathbf{D}_{\mathbf{y}}$ are defined by the following equations:

$$\mathbf{M_{\rho,x}} = \mathcal{A}_x \left(m_\rho^e \right) \quad \mathbf{M_{\rho,y}} = \mathcal{A}_y \left(m_\rho^e \right) \quad \mathbf{M_x} = \mathcal{A}_x \left(m^e \right) \quad \mathbf{M_y} = \mathcal{A}_y \left(m^e \right)$$

$$\mathbf{K_{xx}} = \mathcal{A}_x \left(k_{xx}^e \right) \quad \mathbf{K_{yy}} = \mathcal{A}_y \left(k_{yy}^e \right) \quad \mathbf{K_{xy}} = \mathcal{A}_x \left(k_{xy}^e \right) \quad \mathbf{K_{yx}} = \mathcal{A}_y \left(k_{yx}^e \right) \quad (3.62)$$

$$\mathbf{G_x} = \mathcal{A}_x \left(g_x^e \right) \qquad \mathbf{G_y} = \mathcal{A}_y \left(g_y^e \right) \qquad \mathbf{D_x} = \mathcal{A}_x \left(d_x^e \right) \qquad \mathbf{D_y} = \mathcal{A}_y \left(d_y^e \right)$$

The matrices m_ρ^e, m^e, k_{xx}^e, k_{yy}^e, k_{xy}^e, k_{yx}^e, g_x^e, g_y^e, d_x^e and d_y^e are submatrices of the elements, given by the following equations, and the operators $\mathcal{A}_x$ and $\mathcal{A}_y$ are operators for assembling the global matrices from these submatrices, based on the relationship between the indices in 3.58, 3.59 and 3.57.

$$m_{\rho,ij}^e = \int_{\Omega^e} \rho^e N_i^e N_j^e d\Omega \qquad\qquad m_{ij}^e = \int_{\Omega^e} N_i^e N_j^e d\Omega$$

$$k_{xx,ij}^e = \int_{\Omega^e} \mu^e \left(\frac{\partial N_i^e}{\partial x} \frac{\partial N_j^e}{\partial x} \right) d\Omega \quad k_{yy,ij}^e = \int_{\Omega^e} \mu^e \left(\frac{\partial N_i^e}{\partial y} \frac{\partial N_j^e}{\partial y} \right) d\Omega$$

$$k_{xy,ij}^e = \int_{\Omega^e} \mu^e \left(\frac{\partial N_i^e}{\partial y} \frac{\partial N_j^e}{\partial x} \right) d\Omega \quad k_{yx,ij}^e = \int_{\Omega^e} \mu^e \left(\frac{\partial N_i^e}{\partial x} \frac{\partial N_j^e}{\partial y} \right) d\Omega \qquad (3.63)$$

$$d_{x,kj}^e = \int_{\Omega^e} \frac{\partial N_j^e}{\partial x} P_k^e d\Omega \qquad\qquad d_{y,kj}^e = \int_{\Omega^e} \frac{\partial N_j^e}{\partial y} P_k^e d\Omega$$

Therefore, in a more compact form, the system of equations 3.61 can be written as 3.64, where $\dot{\mathbf{v}} = \left[\frac{Dv_{x,1}}{Dt}, \ldots, \frac{Dv_{x,NV}}{Dt}, \frac{Dv_{y,1}}{Dt}, \ldots, \frac{Dv_{y,NV}}{Dt} \right]^T$, $\mathbf{v} = \left[v_{x,1}, \ldots, v_{x,NV}, v_{y,1}, \ldots, v_{y,NV} \right]^T$, $\mathbf{p} = \left[p_1, \ldots, p_{NP} \right]^T$, and $\mathbf{g} = \left[g_{x,1} \ldots, g_{x,NV}, g_{y,1}, \ldots, g_{y,NV} \right]^T$.

$$\begin{cases} \mathbf{M_\rho} \dot{\mathbf{v}} + \dfrac{1}{Re} \mathbf{K_\mu} \mathbf{v} - \mathbf{G} \mathbf{p} = 0 \\[2mm] \mathbf{D} \mathbf{v} = 0 \end{cases} \qquad (3.64)$$

where $\mathbf{D} = \mathbf{G^T}$.

Regarding the species transport equation, the following system of equations 3.65 is solved, once the velocity and pressure fields are found.

$$\left\{ \mathbf{M} \dot{\mathbf{c}}_s + \frac{1}{Pe_s} \mathbf{K} \mathbf{c}_s - \mathbf{M} \mathbf{Da_{I_s}} = 0 \right. \qquad (3.65)$$

In those systems, $\mathbf{M_\rho}$, $\mathbf{M}$, $\mathbf{K_\mu}$, $\mathbf{K}$, $\mathbf{G}$ and $\mathbf{D}$ are respectively given by the following matrices:

$$\mathbf{M_\rho} = \begin{bmatrix} \mathbf{M_{\rho,x}} & \mathbf{0} \\ \mathbf{0} & \mathbf{M_{\rho,y}} \end{bmatrix}_{2NV \times 2NV} \qquad (3.66)$$

$$\mathbf{M} = \begin{bmatrix} \mathbf{M_x} & \mathbf{0} \\ \mathbf{0} & \mathbf{M_y} \end{bmatrix}_{2NV \times 2NV} \tag{3.67}$$

where $\mathbf{M_x} = \mathbf{M_y}$.

$$\mathbf{K}_\mu = \begin{bmatrix} 2\mathbf{K_{xx}} + \mathbf{K_{yy}} & \mathbf{K_{xy}} \\ \mathbf{K_{yx}} & \mathbf{K_{xx}} + 2\mathbf{K_{yy}} \end{bmatrix}_{2NV \times 2NV} \tag{3.68}$$

where $\mathbf{K_{yx}} = \mathbf{K_{xy}}^T$

$$\mathbf{K} = \begin{bmatrix} \mathbf{K_{xx}} + \mathbf{K_{yy}} & \mathbf{0} \\ \mathbf{0} & \mathbf{K_{xx}} + \mathbf{K_{yy}} \end{bmatrix}_{2NV \times 2NV} \tag{3.69}$$

$$\mathbf{G} = \begin{bmatrix} \mathbf{G_x} \\ \mathbf{G_y} \end{bmatrix}_{2NV \times NP} \tag{3.70}$$

$$\mathbf{D} = \begin{bmatrix} \mathbf{D_x} & \mathbf{D_y} \end{bmatrix}_{NP \times 2NV} \tag{3.71}$$

3.3.3 Mesh Elements

The domain discretization described earlier supports various types of mesh elements. These elements can vary in geometry, such as triangular or rectangular shapes. They can also differ in the order of their shape functions, like linear, quadratic, or cubic, used for variable interpolation.

In this work, triangular elements were chosen. However, the selection of approximation spaces is not entirely arbitrary. The chosen element defines the shape functions for velocity and pressure, which are coupled in the Navier-Stokes equations. This coupling can lead to instability, depending on the element used.

The Ladyzhenskaya-Babuška-Brezzi (LBB) condition is commonly applied to ensure stability in discretized Navier-Stokes formulations [79–81]. While not a necessary condition, it is sufficient to guarantee a unique solution to the saddle point problem in the developed formulation. To allow the use of Galerkin's formulation, triangular mini elements were used.

Barycentric coordinates

Let P be a known point, located inside a triangle whose vertices are points 1, 2 and 3, also known, as shown in Figure 3.2. Let the areas A_1, A_2 and A_3 be defined as shown in the figure.
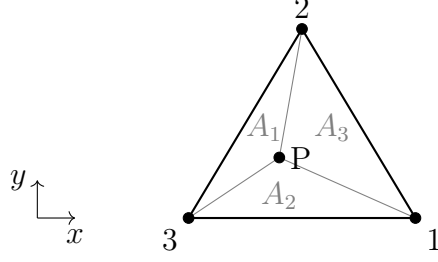
Figure 3.2: Barycentric coordinates of a triangular element.

The position of point P can be expressed from the global x and y coordinates. However, for the methodology that will be described throughout this work, it is interesting to use the local coordinates L_1, L_2 and L_3, called barycentric coordinates and defined using the following equations.

$$L_1 = \frac{A_1}{A} \qquad L_2 = \frac{A_2}{A} \qquad L_3 = \frac{A_3}{A} \tag{3.72}$$

The relationship between the barycentric coordinate system (L_1, L_2, L_3) and the global coordinate system (x, y) is given by 3.73 and 3.74.

$$x = L_1 x_1 + L_2 x_2 + L_3 x_3 \tag{3.73}$$

$$y = L_1 y_1 + L_2 y_2 + L_3 y_3 \tag{3.74}$$

In addition, it is possible to obtain a third equation, given by 3.75.

$$A_1 + A_2 + A_3 = A \implies L_1 + L_2 + L_3 = 1 \tag{3.75}$$

Thus, the values of the barycentric coordinates L_1, L_2 and L_3 as a function of the global coordinates x and y can be obtained by solving the linear system given by 3.76.

$$\begin{bmatrix} 1 & 1 & 1 \\ x_1 & x_2 & x_3 \\ y_1 & y_2 & y_3 \end{bmatrix} \begin{bmatrix} L_1 \\ L_2 \\ L_3 \end{bmatrix} = \begin{bmatrix} 1 \\ x \\ y \end{bmatrix} \tag{3.76}$$

The area of the triangular element can be obtained by calculating the determinant of the linear system matrix, as shown in 3.77.

$$A = \frac{1}{2} \begin{vmatrix} 1 & 1 & 1 \\ x_1 & x_2 & x_3 \\ y_1 & y_2 & y_3 \end{vmatrix} \tag{3.77}$$

31

Mini Element

The mini element, shown in Figure 3.3, is the simplest triangular element that satisfies the Ladyzhenskaya-Babuška-Brezzi condition. It consists of a triangular element with four points: the three vertices of the triangle and its centroid. In this element, the pressure is linear and calculated over the vertices, while the velocity is an incomplete cubic function calculated over all four points.
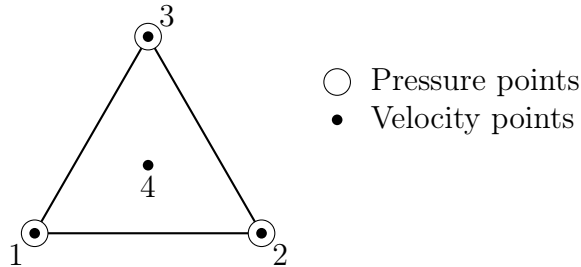
Figure 3.3: Triangular mini element.

The following equations give its shape functions:

$$N_1 = L_1 - 9\,L_1 L_2 L_3$$

$$N_2 = L_2 - 9\,L_1 L_2 L_3$$

$$N_3 = L_3 - 9\,L_1 L_2 L_3$$

$$N_4 = 27\,L_1 L_2 L_3$$

Mini Element Matrices

The mass, $\mathbf{m^e}$, and gradient, $\mathbf{g_x^e}$, $\mathbf{g_y^e}$ matrices of each individual mini element that composes the mesh are given by 3.78, 3.79, 3.80.

$$\mathbf{m^e} = \frac{A}{840} \begin{bmatrix} 83 & 13 & 13 & 45 \\ 13 & 83 & 13 & 45 \\ 13 & 13 & 83 & 45 \\ 45 & 45 & 45 & 243 \end{bmatrix}_{(4,4)} \tag{3.78}$$

$$\mathbf{g_x^e} = \begin{bmatrix} (9/20)\mathbf{g_{x\ lin}^e} + \mathbf{g_{x\ lin}^{eT}} & & {}_{(3,3)} \\ -(9/40)b_1 & -(9/40)b_2 & -(9/40)b_3 \end{bmatrix}_{(4,3)} \tag{3.79}$$

$$\mathbf{g_y^e} = \begin{bmatrix} (9/20)\mathbf{g_{y\ lin}^e} + \mathbf{g_{y\ lin}^{eT}} & & {}_{(3,3)} \\ -(9/40)c_1 & -(9/40)c_2 & -(9/40)c_3 \end{bmatrix}_{(4,3)} \tag{3.80}$$

where $\mathbf{g_{x\ lin}^e}$ and $\mathbf{g_{y\ lin}^e}$ are given by 3.81 and 3.82, respectively.

$$\mathbf{g^e_{x\ lin}} = \frac{1}{6} \begin{bmatrix} b_1 & b_2 & b_3 \\ b_1 & b_2 & b_3 \\ b_1 & b_2 & b_3 \end{bmatrix} \tag{3.81}$$

$$\mathbf{g^e_{y\ lin}} = \frac{1}{6} \begin{bmatrix} c_1 & c_2 & c_3 \\ c_1 & c_2 & c_3 \\ c_1 & c_2 & c_3 \end{bmatrix} \tag{3.82}$$

where a_1, a_2, a_3, b_1, b_2, b_3, c_1, c_2, and c_3 are defined as in 3.83.

$$\begin{array}{lll} a_1 = x_2 y_3 - x_3 y_2 & b_1 = y_2 - y_3 & c_1 = x_3 - x_2 \\ a_2 = x_3 y_1 - x_1 y_3 & b_2 = y_3 - y_1 & c_2 = x_1 - x_3 \\ a_3 = x_1 y_2 - x_2 y_2 & b_3 = y_1 - y_2 & c_3 = x_2 - x_1 \end{array} \tag{3.83}$$

Finally, the stiffness matrices, $\mathbf{k^e_x}$, $\mathbf{k^e_y}$, and $\mathbf{k^e_{xy}}$ are given by 3.84, 3.85, and 3.86, respectively.

$$\mathbf{k^e_x} = \begin{bmatrix} & & & -(27/10)z_x \\ & \mathbf{k^e_{x\ lin}} + (9/10)z_x & & -(27/10)z_x \\ & & & -(27/10)z_x \\ -(27/10)z_x & -(27/10)z_x & -(27/10)z_x & (81/10)z_x \end{bmatrix}_{(4,4)} \tag{3.84}$$

$$\mathbf{k^e_y} = \begin{bmatrix} & & & -(27/10)z_y \\ & \mathbf{k^e_{ylin}} + (9/10)z_y & & -(27/10)z_y \\ & & & -(27/10)z_y \\ -(27/10)z_y & -(27/10)z_y & -(27/10)z_y & (81/10)z_y \end{bmatrix}_{(4,4)} \tag{3.85}$$

$$\mathbf{k^e_{xy}} = \begin{bmatrix} & & & -(27/10)z_{xy} \\ & \mathbf{k^e_{xy\ lin}} + (9/10)z_{xy} & & -(27/10)z_{xy} \\ & & & -(27/10)z_{xy} \\ -(27/10)z_{xy} & -(27/10)z_{xy} & -(27/10)z_{xy} & (81/10)z_{xy} \end{bmatrix}_{(4,4)} \tag{3.86}$$

where $\mathbf{k^e_{xlin}}$, $\mathbf{k^e_{ylin}}$, and $\mathbf{k^e_{xylin}}$ are given by 3.87, 3.88, and 3.89, respectively.

$$\mathbf{k^e_x} = \frac{1}{4A} \begin{bmatrix} b_1^2 & b_1 b_j & b_1 b_3 \\ b_j b_1 & b_j^2 & b_j b_3 \\ b_3 b_1 & b_3 b_j & b_3^2 \end{bmatrix} \tag{3.87}$$

$$\mathbf{k_y^e} = \frac{1}{4A} \begin{bmatrix} c_1^2 & c_1 c_2 & c_1 c_3 \\ c_2 c_1 & c_2^2 & c_2 c_3 \\ c_3 c_1 & c_3 c_2 & c_3^2 \end{bmatrix} \tag{3.88}$$

$$\mathbf{k_{xy}^e} = \frac{1}{4A} \begin{bmatrix} b_1 c_1 & b_1 c_2 & b_1 c_3 \\ b_2 c_1 & b_2 c_2 & b_2 c_3 \\ b_3 c_1 & b_3 c_2 & b_3 c_3 \end{bmatrix} \tag{3.89}$$

and z_x, z_y, and z_{xy} are obtained by 3.90, 3.91, and 3.92, respectively.

$$z_x = \frac{1}{4A} \left(b_j^2 + b_j b_k + b_k^2 \right) \tag{3.90}$$

$$z_y = \frac{1}{4A} \left(c_j^2 + c_j c_k + c_k^2 \right) \tag{3.91}$$

$$z_{xy} = \frac{1}{4A} \left(b_j c_j + b_k c_k + \frac{1}{2} b_j c_k + \frac{1}{2} b_k c_j \right) \tag{3.92}$$

3.4 The Semi-Lagrangian Method

In the momentum conservation equation, the material derivative includes a non-linear convection term, expressed as $\mathbf{v} \cdot \nabla \mathbf{v}$. When applying the Galerkin method, this convective component can lead to non-physical oscillations in the solution, particularly at higher Reynolds and Péclet numbers or when inappropriate time steps are used.

To mitigate these oscillations, various stabilization techniques can be employed. One such technique is the Streamline Upwind Petrov-Galerkin (SUPG) method, which introduces modified weighting functions in the weak formulation. This modification helps counteract the artificial diffusion introduced by central difference schemes. Another approach involves the Characteristic Galerkin methods, which decouple the original equation into convective and diffusive parts and solve them using suitable boundary and initial conditions. Alternatively, the Characteristic-Based Split (CBS) method removes the pressure gradient from the momentum equation, allowing different interpolation strategies for velocity and pressure fields. More information on these methods can be found in references [82] and [77].

A particularly effective strategy for handling advection is the semi-Lagrangian method, originally developed for atmospheric simulations [83]. This method is valued for its ease of implementation, its ability to maintain symmetric system matrices, and its unconditional stability even when large time steps are used [84, 85].

Unlike a fully Lagrangian approach, which tracks the continuous motion of fluid

particles, the semi-Lagrangian method adapts to fixed spatial nodes, such as those in a finite element mesh. It achieves this by identifying, at each time step, the trajectory of particles that will arrive precisely at the mesh nodes after a time increment.

In this framework, the algorithm computes the so-called departure points locations in the domain where particles must have originated to reach the current mesh node positions after advection over a time interval Δt.

The material derivative of a scalar field Ψ, which accounts for both local and convective variations, is expressed as:

$$\frac{D\Psi}{Dt} = \frac{\partial \Psi}{\partial t} + u\frac{\partial \Psi}{\partial x} + v\frac{\partial \Psi}{\partial y} + w\frac{\partial \Psi}{\partial z} \tag{3.93}$$

A first-order approximation of the material derivative in time can be written as:

$$\frac{D\Psi}{Dt} \approx \frac{\Psi^{n+1} - \Psi_d^n}{\Delta t} \tag{3.94}$$

Here, Ψ_d^n denotes the value of Ψ at the departure point. These departure points are determined by tracing backwards along the velocity field using:

$$\mathbf{x_d^n} = \mathbf{x^{n+1}} - \mathbf{v^n}\Delta t \tag{3.95}$$
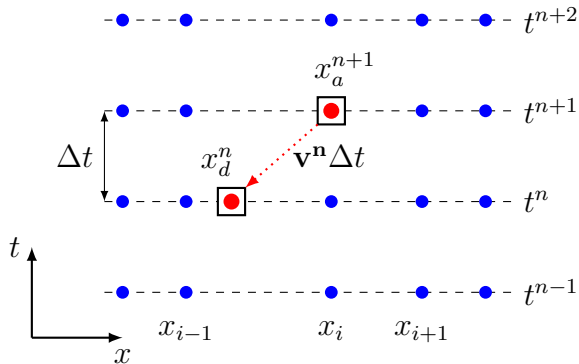
Figure 3.4: Semi-Lagrangian scheme in one-dimensional mesh.

Consider $\mathbf{x_n}$ the mesh node coordinates (Figure 3.4). Once the position of the nodes shifted backward by $\mathbf{v^n}\Delta t$, $\mathbf{x}_d$, are computed, the corresponding value of Ψ_d^n is obtained by interpolating the scalar field Ψ at those departure locations using the known nodal values.

By the use of this approximation, the differential formulation of Navier Stokes and species transport equations becomes as 3.96, 3.97 and 3.98, where $\mathbf{v_d^n}$ represents velocity at the virtual departure position of all mesh points at the preceding time-step.

$$\nabla \cdot \mathbf{v^{n+1}} = 0 \qquad (3.96)$$

$$\rho(x) \left(\frac{\mathbf{v^{n+1}} - \mathbf{v_d^n}}{\Delta t} \right) = -\nabla p^{n+1} + \frac{1}{Re} \nabla \cdot \mu(x) \left[\nabla \mathbf{v^{n+1}} + (\nabla \mathbf{v^{n+1}})^T \right] \qquad (3.97)$$

$$\left(\frac{c_s^{n+1} - c_{s_d}^n}{\Delta t} \right) = -\frac{1}{Pe_s} \nabla^2 c_s + Da_{Is} \qquad (3.98)$$

Therefore, the matricial form of the variational form of the Navier-Stokes and species transport equations are expressed by 3.99 and 3.100.

$$\begin{cases} \mathbf{M}_\rho \left(\dfrac{\mathbf{v^{n+1}} - \mathbf{v_d^n}}{\Delta t} \right) + \dfrac{1}{Re} \mathbf{K}_\mu \mathbf{v^{n+1}} - \mathbf{Gp^{n+1}} = \mathbf{0} \\ \mathbf{Dv^{n+1}} = \mathbf{0} \end{cases} \qquad (3.99)$$

$$\left\{ \mathbf{M} \left(\frac{\mathbf{c_s^{n+1}} - \mathbf{c_{s_d}^n}}{\Delta t} \right) + \frac{1}{Pe_s} \mathbf{Kc_s^{n+1}} - \mathbf{MDa_{I_s}^n} = \mathbf{0} \right. \qquad (3.100)$$

3.5 Problem Formulation and Resolution

The mathematical formulation of the problem consists of a linear system developed based on all the considerations presented earlier in this chapter. The solution of the linear system will provide the velocity and pressure fields throughout the problem domain. This section describes the procedures for defining the linear system and solving it.

3.5.1 Linear System Definition

Once we have all the variables present in the problem equation, we define the linear system $\mathbf{Ax} = \mathbf{b}$, in which the vector $\mathbf{b}$ is based on the flow variables at time n and the vector $\mathbf{x}$ is made up of the velocity and pressure fields at time $n + 1$, as shown in equation 3.101.

$$\begin{bmatrix} \frac{1}{\Delta t}\mathbf{M}_\rho + \frac{1}{Re}\mathbf{K_{11}} & \frac{1}{Re}\mathbf{K_{12}} & -\mathbf{G_x} \\ \frac{1}{Re}\mathbf{K_{21}} & \frac{1}{\Delta t}\mathbf{M}_\rho + \frac{1}{Re}\mathbf{K_{22}} & -\mathbf{G_y} \\ \mathbf{D_x} & \mathbf{D_y} & \mathbf{0} \end{bmatrix} \begin{bmatrix} \mathbf{v_x^{n+1}} \\ \mathbf{v_y^{n+1}} \\ \mathbf{p^{n+1}} \end{bmatrix} = \begin{bmatrix} \frac{1}{\Delta t}\mathbf{M}_\rho \mathbf{v_{d,x}^n} \\ \frac{1}{\Delta t}\mathbf{M}_\rho \mathbf{v_{d,y}^n} \\ \mathbf{0} \end{bmatrix}$$
$$(3.101)$$

Thus, the time evolution of the flow is obtained by solving the linear system consecutively.

$$\left[\frac{1}{\Delta t}\mathbf{M} + \frac{1}{Pe_s}\mathbf{K} \right]\left[\mathbf{c_s^{n+1}} \right] = \left[\frac{1}{\Delta t}\mathbf{Mc_{s_d}^n} + \mathbf{MDa_{I_s}^n} \right] \tag{3.102}$$

3.5.2   Imposition of Boundary and Initial Conditions

Before solving the linear system defined in equation (3.92), however, the velocity and pressure boundary conditions must be imposed. For a flow modeled by the linear system $\mathbf{Ax} = \mathbf{b}$, discretized on a mesh with NN velocity nodes, the enforcement of the horizontal velocity boundary condition at the i-th node is carried out by replacing the i-th row of matrix $\mathbf{A}$ with the unit vector $\hat{\mathbf{e}}_i$, and setting the i-th entry of vector $\mathbf{b}$ to the prescribed horizontal velocity value at that node, $v_{x\Gamma i}$. In this way, as shown in equation 3.103, the horizontal velocity component at node i at time step $n+1$, $v_{x_i}^{n+1}$, is trivially obtained and equals the boundary condition prescribed at that node.

Similarly, to enforce the boundary condition for the vertical velocity component at the i-th node of the mesh, the same operation is performed on row $i + NN$ of matrix $\mathbf{A}$, as indicated in equation 3.104. In turn, to impose the pressure boundary condition at the i-th node, this operation is carried out on row $i + 2NN$ of matrix $\mathbf{A}$, as shown in equation 3.105.

$$\hat{\mathbf{e}}_i \cdot \mathbf{x} = v_{x_{\Gamma_i}} \quad \implies \quad v_{x_i}^{n+1} = v_{x_{\Gamma_i}} \tag{3.103}$$

$$\hat{\mathbf{e}}_{i+N_N} \cdot \mathbf{x} = v_{y_{\Gamma_i}} \quad \implies \quad v_{y_i}^{n+1} = v_{y_{\Gamma_i}} \tag{3.104}$$

$$\hat{\mathbf{e}}_{i+2N_N} \cdot \mathbf{x} = p_{\Gamma_i} \quad \implies \quad p_i^{n+1} = p_{\Gamma_i} \tag{3.105}$$

3.5.3   Solving the Linear System

Once the linear system with the imposed boundary conditions is assembled, it is solved using the direct solver package *umfpack* [86], implemented through the *PETSc* scientific computing library [87]. This solver implements a direct method for solving linear systems, based on LU decomposition, and is particularly efficient for systems with sparse matrices, such as the one considered here. After applying the solver, the velocity and pressure fields at time step $n+1$ are obtained as the solution of the linear system.

3.6 Computational Implementation

Finally, the methodology described in the previous sections was implemented in a Python code using the following open-source libraries, among others:

- Meshio, for mesh reading and results exportation;

- NumPy and Scipy, for sparse matrix and vector operations;

- Petsc4py, for solving the linear system;

The meshes used for the spatial discretization of each flow domain were generated using the software Gmsh [88].

The algorithm executed for the simulations is presented in the pseudo-code below, which references the procedures discussed throughout the methodology in this chapter. The simulation algorithm begins by defining the dimensionless fluid properties, namely the densities and viscosities of the involved phases (ρ^* and μ^*). Next, the relevant dimensionless numbers such as Reynolds (Re), Froude (Fr), Peclet for species transport (Pe_s), and Damköhler for interfacial reactions (Da_{Is}) are specified, as they govern the flow and transport behavior. The time step Δt is then chosen to control the temporal resolution of the simulation. The computational mesh is imported and its nodes are mapped to allow spatial discretization. Numpy vectors for velocity components (v_x, v_y), pressure (p), and concentration (c) are created to store the solution fields. Boundary nodes are identified, and the corresponding boundary conditions are defined and applied. Element-level matrices, such as the mass matrix $\mathbf{m_e}$, stiffness matrix $\mathbf{k_e}$, gradient matrices $\mathbf{g_x}, \mathbf{g_y}$, and divergence matrices $\mathbf{d_{ex}}, \mathbf{d_{ey}}$, are computed. These are assembled into global time-independent matrices: the mass matrix $\mathbf{M}$, stiffness matrix $\mathbf{K}$, gradient matrix $\mathbf{G}$, and the divergence matrix $\mathbf{D} = \mathbf{G}^T$. The simulation time is initialized with $t = t_0$ and the initial fields are saved. At each time step, properties are assigned to mesh nodes, and time-dependent element matrices are computed, including density-weighted mass matrix, $\mathbf{m_{e_\rho}}$, and viscosity-dependent stiffness contributions ($\mathbf{k_e^x}, \mathbf{k_e^y}, \mathbf{k_e^{xy}}, \mathbf{k_e^{yx}}$). These are assembled into mutable global matrices $\mathbf{M}_\rho$ and $\mathbf{K}_\mu$. The semi-Lagrangian method is applied to velocity, pressure, and concentration fields, yielding the displaced positions $\mathbf{x_d}$, velocities $\mathbf{v_d}$, and species concentrations $\mathbf{c_{ds}}$. Linear systems are then defined for velocity-pressure coupling, boundary conditions are applied, and the system is solved to obtain updated flow fields. A similar process is carried out for the species transport equation: the semi-Lagrangian step is applied, the linear system is defined, boundary conditions are enforced, and the system is solved to update concentration. Finally, time is advanced by Δt, results are stored, and the loop continues until the final time t_{end} is reached.

Algorithm 1 Simulation Algorithm
1: **Define** dimensionless fluid properties: ρ^* and μ^*
2: **Define** dimensionless numbers: Re, Fr, Pe_s and Da_{Is}
3: **Define** time step Δt
4: **Import** mesh
5: **Map** mesh nodes
6: **Create** numpy vectors v_x, v_y, p and c
7: **Identify** boundary nodes
8: **Define** boundary conditions
9: **Apply** boundary conditions
10: **Compute** local time-independent matrices $\mathbf{m_e}, \mathbf{k_e}, \mathbf{g_x}, \mathbf{g_y}, \mathbf{d_{ex}}, \mathbf{d_{ey}}$
11: **Assemble** permanent global matrices $\mathbf{M}, \mathbf{K}, \mathbf{G}, \mathbf{D} = \mathbf{G}^T$
12: $t \leftarrow t_0$
13: **Save** initial results
14: **while** $t < t_{\text{end}}$ **do**
15:    **Assign** properties to mesh nodes
16:    **Compute** time-dependent element matrices $\mathbf{m_{e_\rho}}, \mathbf{k_e^x}, \mathbf{k_e^y}, \mathbf{k_e^{xy}}, \mathbf{k_e^{yx}}$
17:    **Assemble** mutable global matrices $\mathbf{M}_\rho, \mathbf{K}_\mu$
18:    **Apply** semi-Lagrangian method for velocity and pressure (compute $\mathbf{x_d}, \mathbf{v_d}, \mathbf{c_{ds}}$)
19:    **Define** linear system for velocity and pressure
20:    **Apply** boundary conditions for velocity and pressure
21:    **Solve** linear system for velocity and pressure
22:    **Apply** semi-Lagrangian method for species concentration (compute $\mathbf{c_{ds}}$)
23:    **Define** linear system for species concentration
24:    **Apply** boundary conditions for species concentration
25:    **Solve** linear system for species concentration
26:    $t \leftarrow t + \Delta t$
27:    **Save** results
28: **end while**

Chapter 4

Results

This chapter presents the preliminary results obtained by applying the simplified version of the proposed methodology to a set of simulations of interest.

All the simulations were carried out on a Dell R650 server with 128 GB of RAM and an Intel Xeon Gold 6348 processor with 28 cores and a frequency of 2.60 GHz. Each simulation was run on 1 core of the processor, which executed the code in Python.

4.1   Single-phase Flow

In the single-phase case, the equation for the conservation of the quantity of movement, given by 3.20, does not have the $\nabla \mathbf{v}^T$ term. Therefore, the K matrix of the problem formulation, given by 3.68, is reduced to 4.1. The other items of the methodology described in the previous chapter were kept unchanged.

$$\mathbf{K} = \left[\begin{array}{cc} \mathbf{K_{xx}} + \mathbf{K_{yy}} & \mathbf{0} \\ \mathbf{0} & \mathbf{K_{xx}} + \mathbf{K_{yy}} \end{array} \right]_{2NV \times 2NV} \tag{4.1}$$

4.1.1   Plane Poiseuille Flow

The flow between flat plates consists of flow through a two-dimensional channel formed in the region between two infinite flat plates. For this flow, a channel of unit width and aspect ratio equal to 15 was considered. On the left and right boundaries of the domain, the boundary conditions of fluid entry - with a uniform horizontal velocity profile equal to 1 - and zero prescribed pressure were imposed respectively. Non-slip boundary conditions were imposed on the lower and upper boundaries. The geometry of the flow, as well as the boundary conditions, are shown in Figure 4.1.
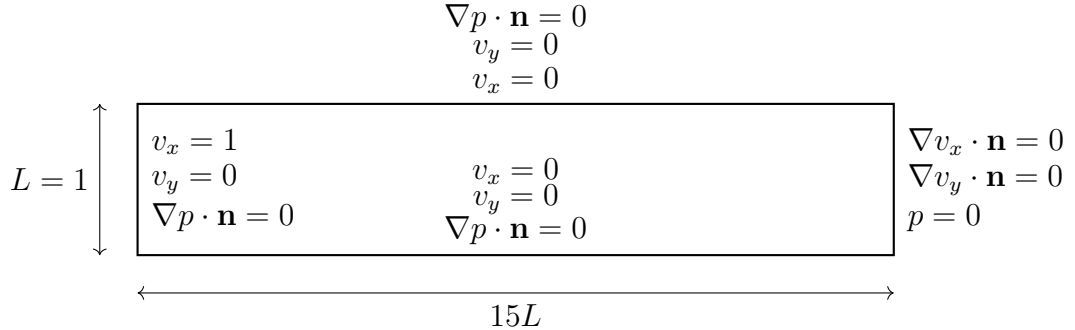
Figure 4.1: Geometry and boundary conditions of flow between flat plates.

The flow was simulated for $Re = 100$. In addition, four triangular meshes were used for mesh study. Mesh information is presented in Table 4.1.

Table 4.1: Plane Poiseuille mesh statistics and computational time for each case.

Mesh	Nodes	Elements	CPU time (h)	Time step [-]
Mesh 01	11317	21832	5.00	0.01
Mesh 02	19863	38656	8.65	0.01
Mesh 03	28252	55226	12.55	0.01
Mesh 04	44319	87036	19.77	0.01

The horizontal velocity and vertical velocity fields in the permanent regime obtained in the simulation with mesh 01 are shown in Figure 4.2.

(a) Horizontal velocity, v_x.

(b) Vertical velocity, v_y.
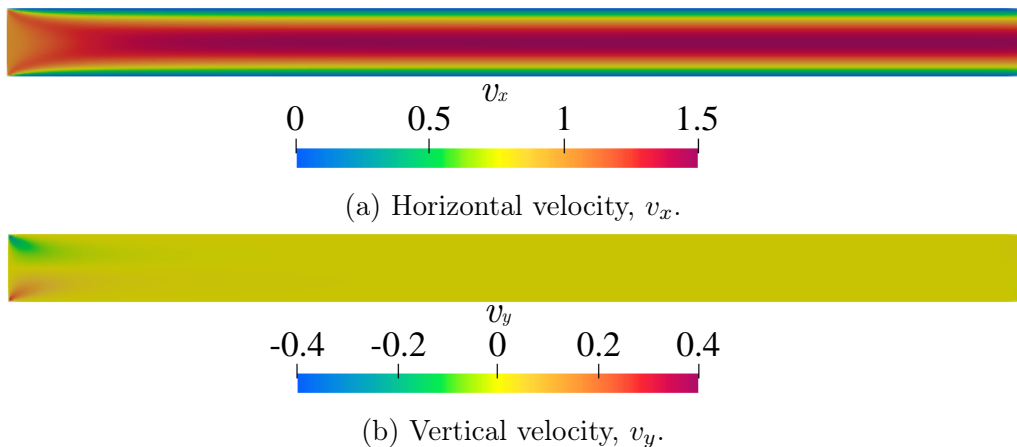
Figure 4.2: Horizontal and vertical velocity fields obtained in the simulation of the flat plates flow with mesh 01.

The flow between flat plates, due to its simplicity, admits an analytical solution for the Navier-Stokes equations, given by 4.2.

$$v_x(y) = \frac{6}{L^2} y(L - y) \tag{4.2}$$

In order to validate the results obtained through the simulations, their fully developed horizontal velocity profiles were compared with the analytical solution of the flow, given by 4.2. This comparison is shown in Figure 4.3.
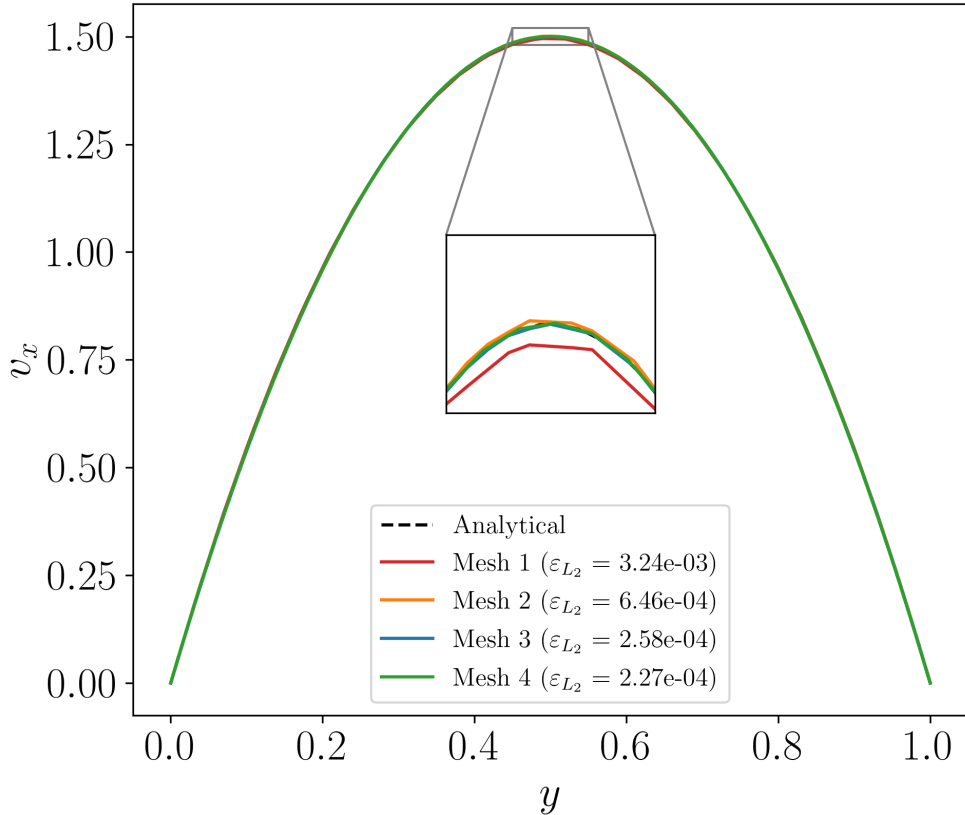

Figure 4.3: Comparison between the numerical horizontal velocity profiles and the analytical profile.

In order to quantify the correspondence between the velocity profiles obtained in the simulations and the analytical profile, the L2 norm of the difference between the profiles, given by 4.3, was used as the error metric. In this equation, v_i^{num} is the speed at point i of the profile obtained through simulation, while v_i^{ref} is the reference speed at the same point, calculated analytically.

$$\varepsilon_{L_2} = \sqrt{\frac{1}{n} \sum_{i=1}^{n} \left(v_i^{\text{num}} - v_i^{\text{ref}}\right)^2} \tag{4.3}$$

The errors calculated for each of the simulations of the flow between flat plates are shown in Table 4.2.

Table 4.2: Errors in simulations of flow between flat plates.

Mesh	ε_{L_2}
Mesh 01	3.24×10^{-3}
Mesh 02	6.46×10^{-4}
Mesh 03	2.58×10^{-4}
Mesh 04	2.27×10^{-4}

The error values found are quite small compared to the magnitudes of the flow velocities in question, which corroborates the validity of the proposed methodology.

4.1.2 Lid-Driven Cavity Flow

This typical problem consists of the flow in a square cavity, which is induced by the horizontal movement of its upper wall. For its simulation, a square cavity with unit width was considered. A moving wall condition with unit velocity was imposed for the top boundary of the domain, and non-slip conditions for the left, bottom, and right boundaries. In addition, a zero prescribed pressure condition was imposed for the lower right vertex of the mesh. Figure 4.4 shows the flow geometry and the boundary conditions imposed.
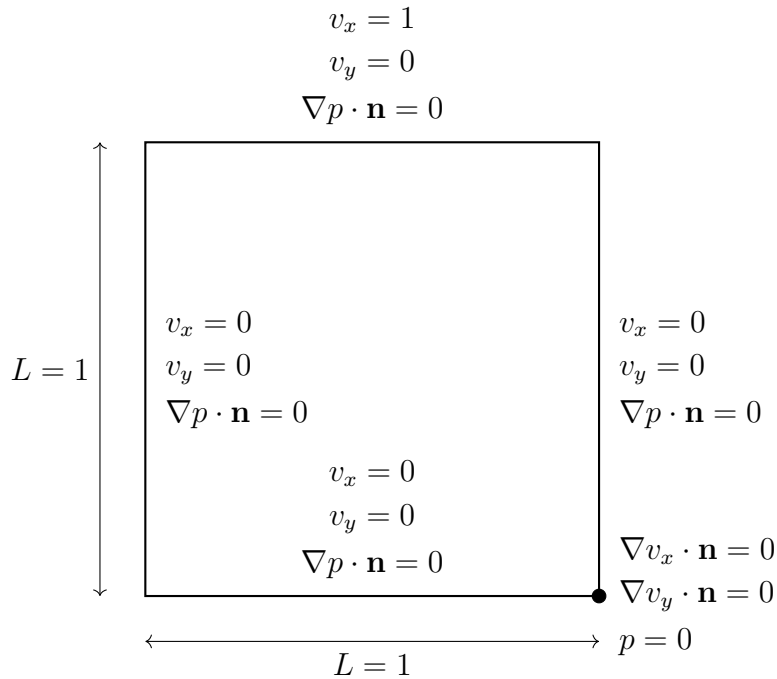

Figure 4.4: Geometry and boundary conditions of flow in a cavity.

This flow was simulated for four different Reynolds numbers ($Re = 10$, $Re = 100$, $Re = 400$, and $Re = 1000$), and the results were compared with those published by

[89]. For the case with $Re = 100$, four triangular meshes were used for mesh study. Mesh information is presented in Table 4.3. Based on the results of this mesh study, Mesh 04 was used to perform the simulation of the other three cases.

Table 4.3: Lid-Driven mesh statistics and computational time for each case.

Mesh	Nodes	Elements	CPU time (h)	Time step [-]
Mesh 01	11823	23264	5.52	0.01
Mesh 02	18299	36096	8.93	0.01
Mesh 03	32625	64580	17.70	0.01
Mesh 04	46678	92554	27.57	0.01

Case 1: $Re = 10$

The flow in a cavity with $Re = 10$ was simulated for 1000 iterations, with a time step $\Delta t = 0.01$. The horizontal and vertical velocity fields in the permanent regime obtained in the simulation, as well as the comparison of the horizontal velocity profiles at y = 0.5 and vertical velocity profiles at x = 0.5 with the reference results, are shown in Figures 4.5, 4.6 and 4.7.


(a) Horizontal velocity.   (b) Vertical velocity.
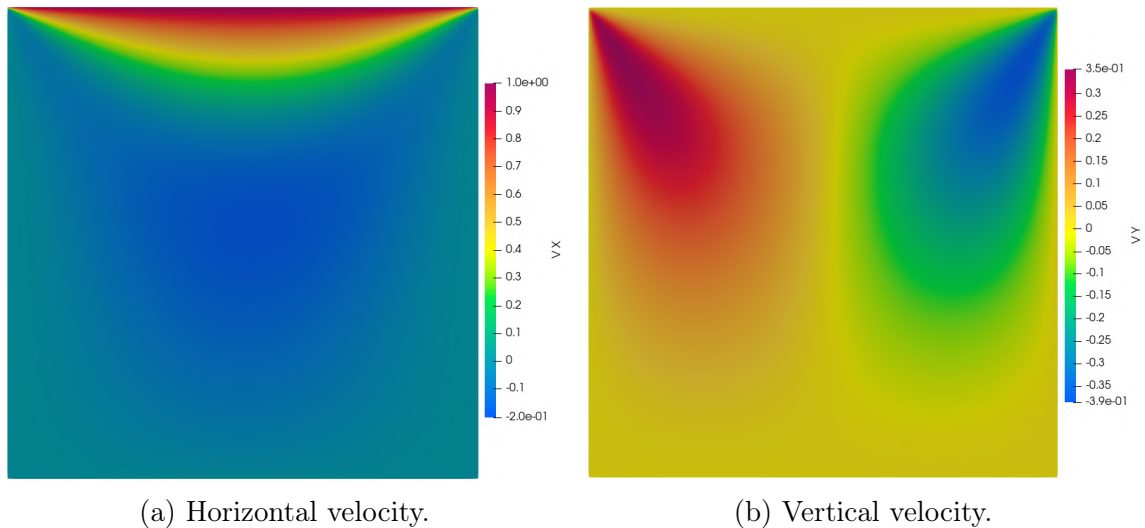
Figure 4.5: Horizontal and vertical velocity fields obtained by simulating the flow in a cavity with $Re = 10$.
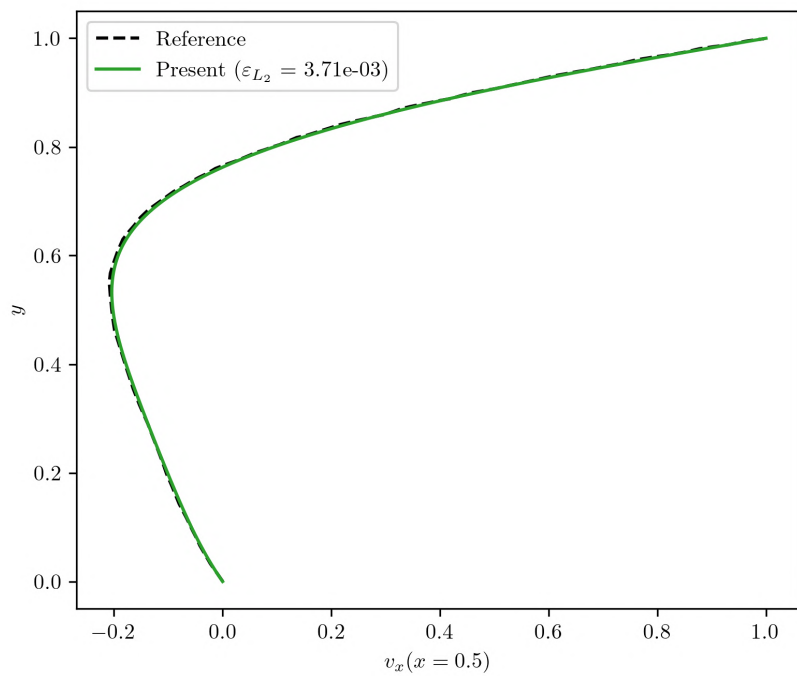
Figure 4.6: Comparison between the numerical horizontal velocity profile and the reference with $Re = 10$.
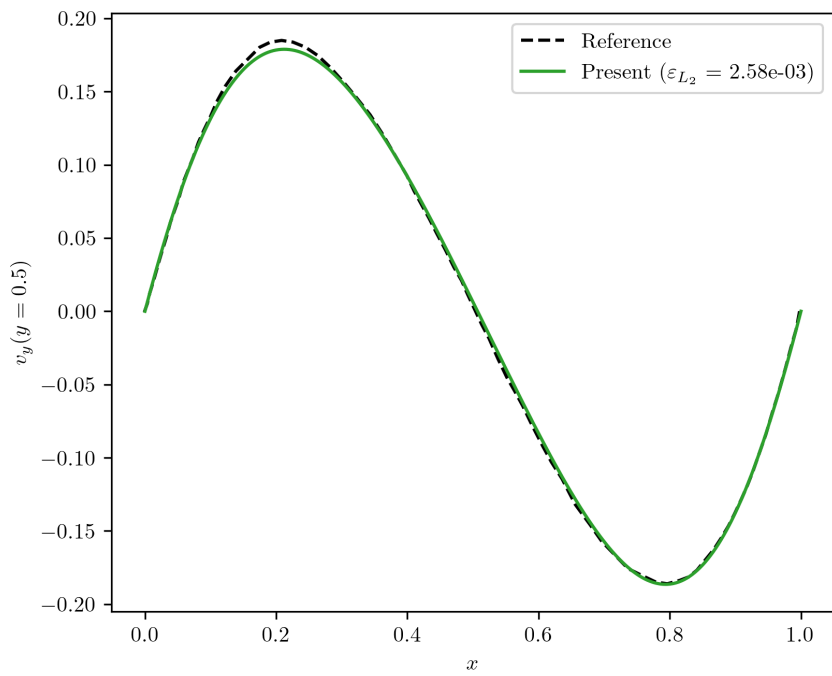

Figure 4.7: Comparison between the numerical vertical velocity profile and the reference with $Re = 10$.

Case 2: $Re = 100$

The flow in a cavity with $Re = 100$ was simulated for 3000 iterations, with a time step $\Delta t = 0.01$. The horizontal and vertical velocity fields in the permanent regime obtained in the simulation, as well as the comparison of the horizontal velocity profiles at y = 0.5 and vertical velocity profiles at x = 0.5 with the reference results, are shown in Figures 4.8, 4.9 and 4.10.

(a) Horizontal velocity.　　　　　　(b) Vertical velocity.
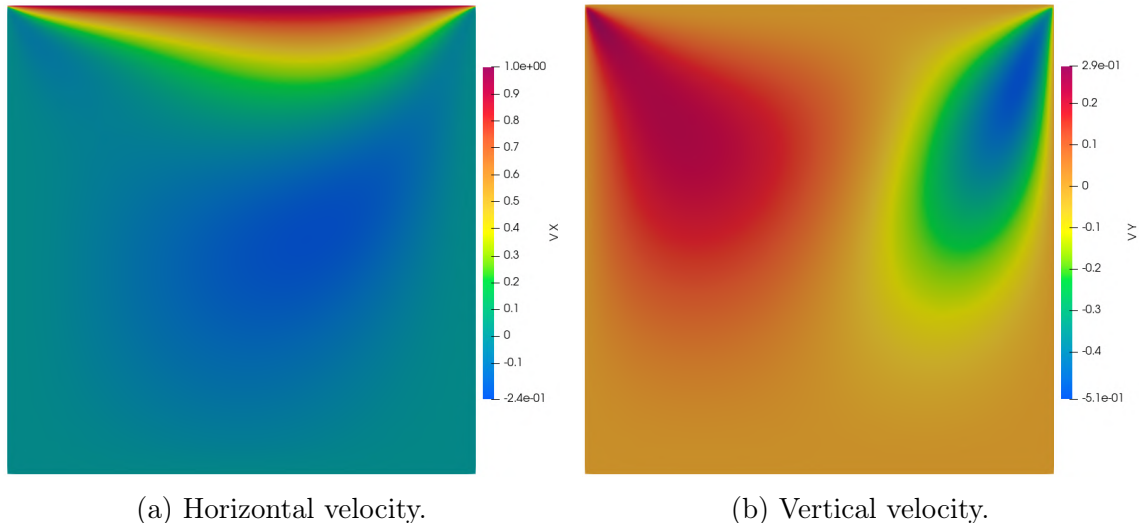
Figure 4.8: Horizontal and vertical velocity fields obtained by simulating the flow in a cavity with $Re = 100$.
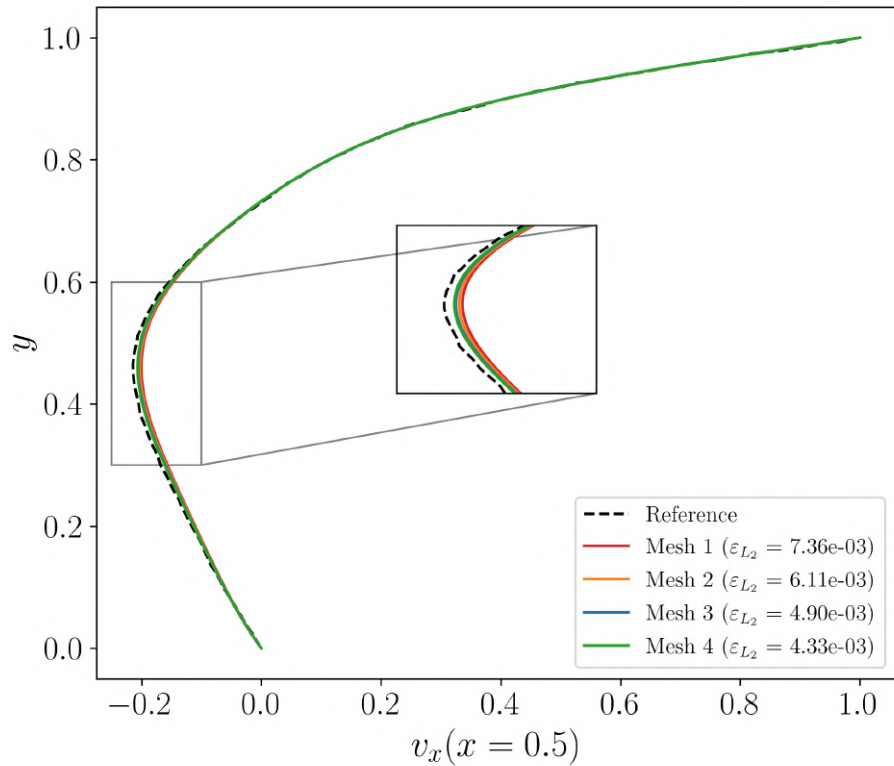
Figure 4.9: Comparison between the numerical horizontal velocity profiles and the reference with $Re = 100$.
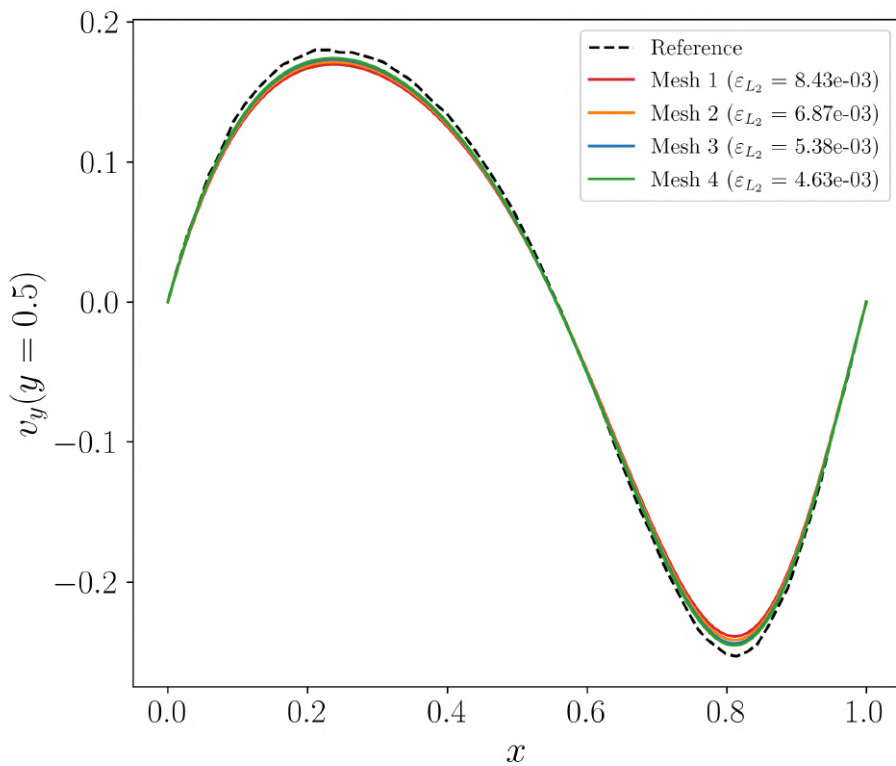

Figure 4.10: Comparison between the numerical vertical velocity profiles and the reference with $Re = 100$.

The errors calculated for each of the simulations of the Cavity flow are shown in Table 4.4.

Table 4.4: Errors in simulations of Lid-Driven Cavity Flow $Re = 100$.

Mesh	ε_{L_2}
Mesh 01	7.36×10^{-3}
Mesh 02	6.11×10^{-3}
Mesh 03	4.90×10^{-3}
Mesh 04	4.33×10^{-3}

Case 3: $Re = 400$

The flow in a cavity with $Re = 400$ was simulated for 3000 iterations, with a time step $\Delta t = 0.01$. The horizontal and vertical velocity fields in the permanent regime obtained in the simulation, as well as the comparison of the horizontal velocity profiles at y = 0.5 and vertical velocity profiles at x = 0.5 with the reference results, are shown in Figures 4.11, 4.12 and 4.13.

(a) Horizontal velocity.

(b) Vertical velocity.
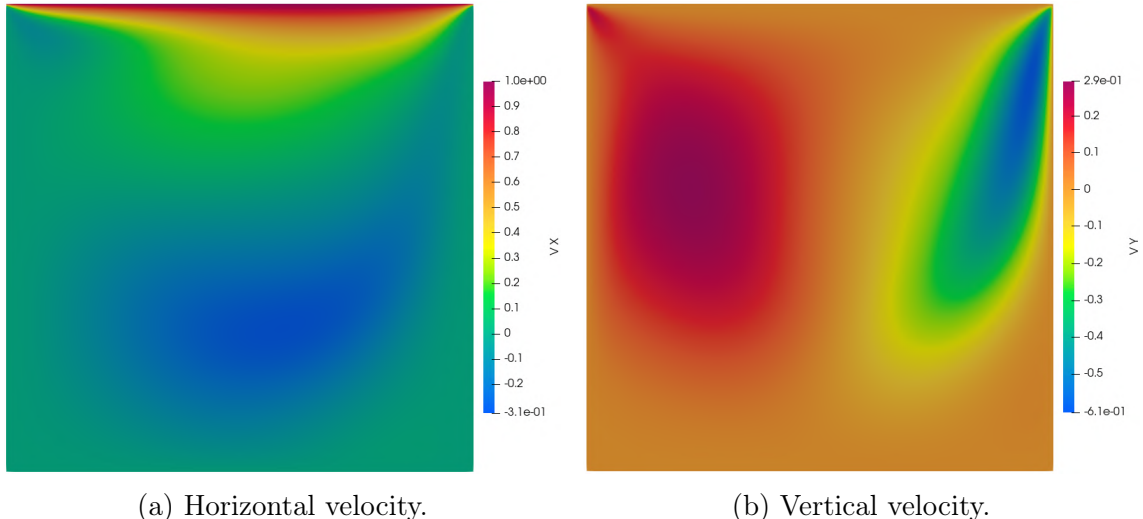
Figure 4.11: Horizontal and vertical velocity fields obtained by simulating the flow in a cavity with $Re = 400$.
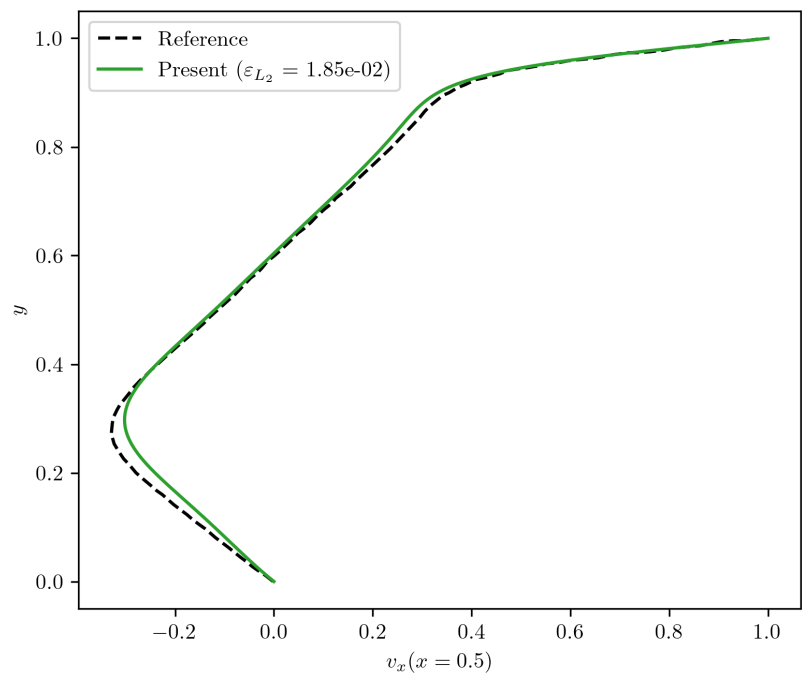
Figure 4.12: Comparison between the numerical horizontal velocity profiles and the reference with $Re = 400$.
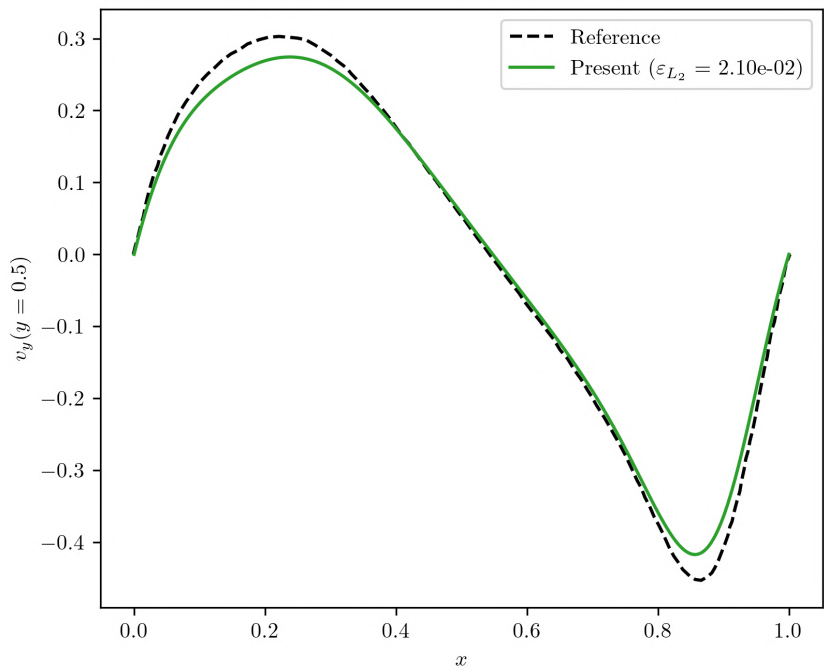
Figure 4.13: Comparison between the numerical vertical velocity profile and the reference with $Re = 400$.

Case 4: $Re = 1000$

The flow in a cavity with $Re = 1000$ was simulated for 10000 iterations, with a time step $\Delta t = 0.01$. The horizontal and vertical velocity fields in the permanent regime obtained in the simulation, as well as the comparison of the horizontal velocity profiles at y = 0.5 and vertical velocity profiles at x = 0.5 with the reference results, are shown in Figures 4.14, 4.15 and 4.16.


(a) Horizontal velocity. (b) Vertical velocity.
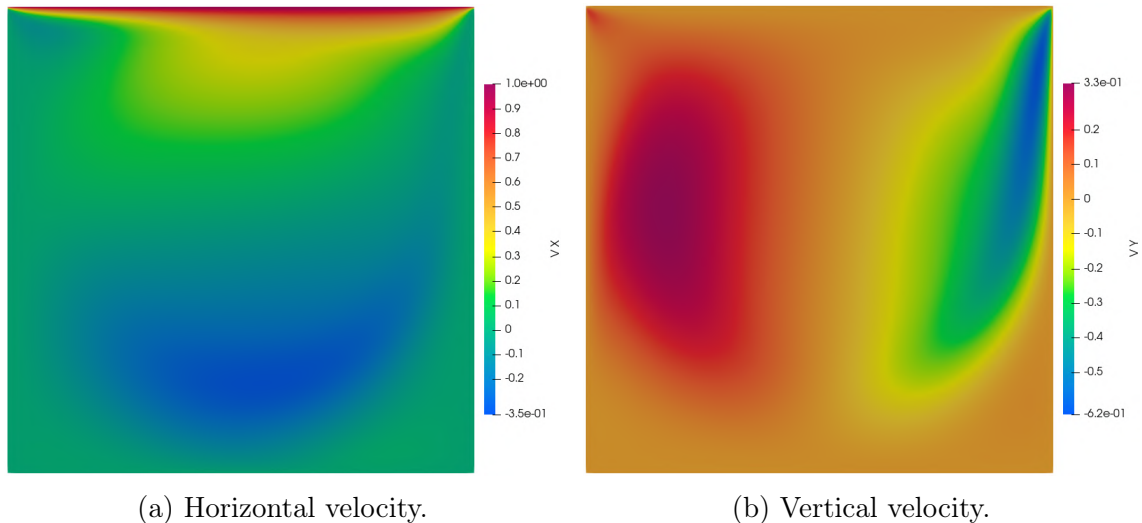
Figure 4.14: Horizontal and vertical velocity fields obtained by simulating the flow in a cavity with $Re = 1000$.
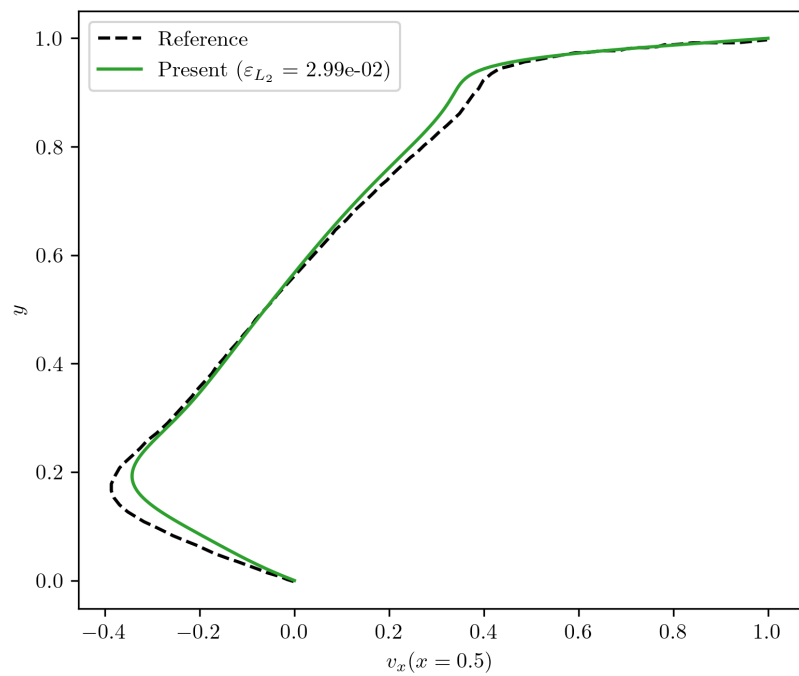
Figure 4.15: Comparison between the numerical horizontal velocity profiles and the reference with $Re = 1000$.
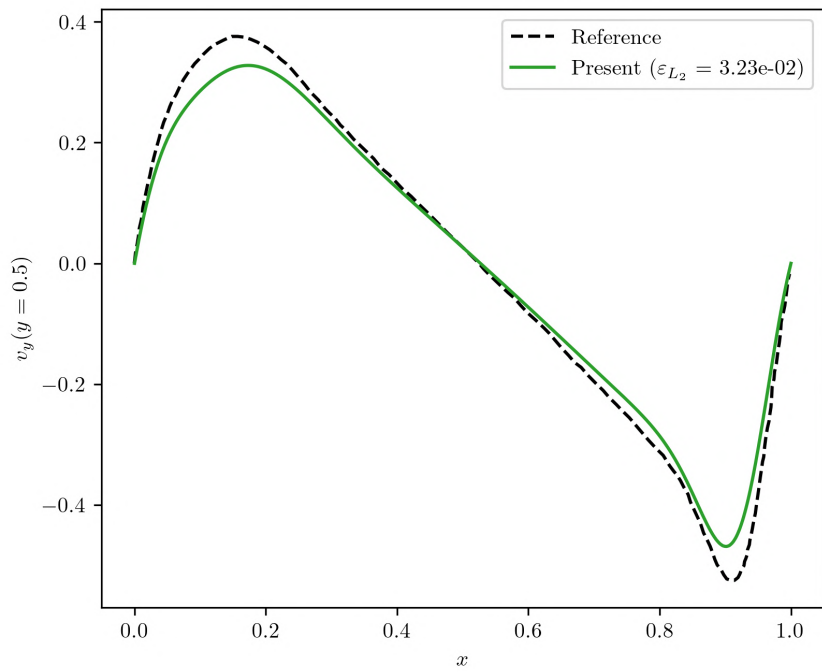

Figure 4.16: Comparison between the numerical vertical velocity profile and the reference with $Re = 1000$.

Once again, very low error values were obtained in relation to the magnitudes of the flow velocities in question, which indicates the high accuracy of the proposed methodology in obtaining the reference results. However, the error increased with increasing Reynolds number. In Figures 4.12, 4.13, 4.15 and 4.16, referring to the simulations with Reynolds number equal to 400 and 1000, it can be seen that the maxima and minima of the reference results are not reached by the simulation, which shows the diffusion phenomenon intrinsic to the implemented method. This phenomenon is negligible for moderate Reynolds numbers, but becomes significant in simulations with higher Reynolds numbers. For the simulations in question, although noticeable, diffusion is not significant and does not compromise the conformity of their results with those of the reference.

4.1.3 Flow Over a Backward-Facing Step

The backward-facing step flow is a classical benchmark problem in fluid dynamics. The flow typically occurs when a fluid passes over a sudden expansion in a channel, creating a recirculation zone downstream of the step [90–92].

For this flow, the downstream channel was defined to have a height H equal to $1.9423h$, with a step height S equal to $0.9423h$ and a unit upstream inlet height h. Upstream and downstream of the step, the channel length is $L_u = 2h$ and $L_d = 20h$, respectively. All geometrical length scales are made dimensionless based on the upstream inlet height h. On the left and right boundaries of the domain, the boundary conditions of fluid entry - with a fully developed horizontal velocity profile - and zero prescribed pressure were imposed respectively. Non-slip boundary conditions were imposed on the lower and upper boundaries. The geometry of the flow, as well as the boundary conditions, are shown in Figure 4.17.
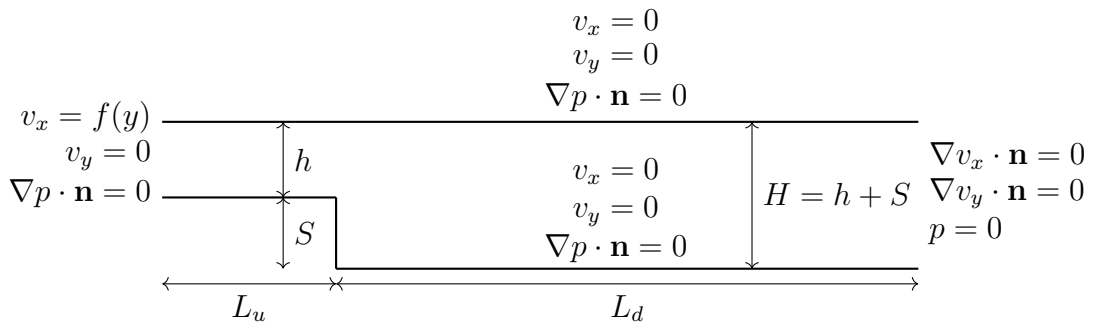
Figure 4.17: Geometry and boundary conditions for flow in a backward-facing step.

The Reynolds number for this geometry is defined as $Re_D = \dfrac{UD}{\nu}$ where U represents the mean inlet velocity — equal to two-thirds of the maximum inlet velocity — and D is the hydraulic diameter of the inlet channel. In this case, the hydraulic diameter is equivalent to twice the inlet channel height, that is, $D = 2h$.

The parameter $Re_D = 100$ was used to simulate this flow for 3000 iterations, with a time step of $\Delta t = 0.01$. To evaluate the influence of mesh resolution on the numerical results, five different triangular meshes were employed as shown in Table 4.5.

Table 4.5: Backward-Facing Step mesh statistics and computational time for each case.

Mesh	Nodes	Elements	CPU time (h)	Time step [-]
Mesh 01	19641	38322	2.87	0.01
Mesh 02	24413	47257	3.65	0.01
Mesh 03	30588	61174	4.52	0.01
Mesh 04	39982	78591	5.82	0.01
Mesh 05	54157	108312	8.03	0.01

The horizontal and vertical velocity contours in the permanent regime obtained in the simulation with Mesh 05 are shown in Figure 4.18.

(a) Horizontal velocity, v_x.

(b) Vertical velocity, v_y.
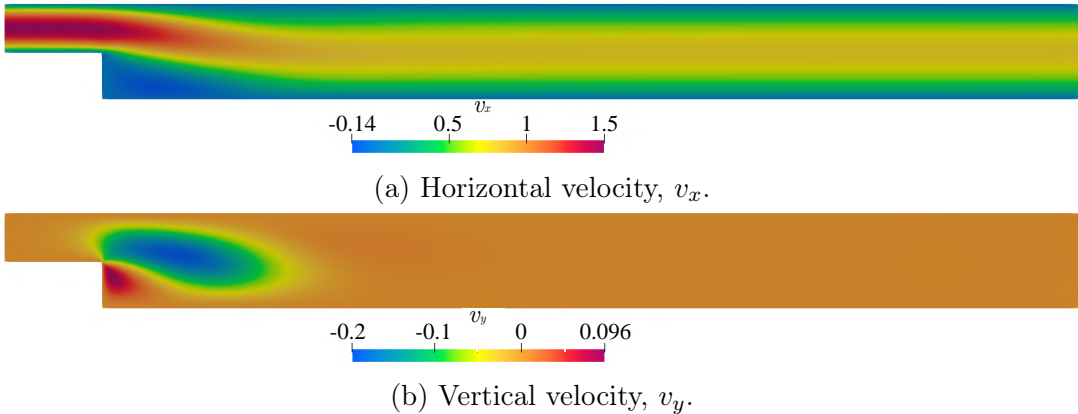
Figure 4.18: Horizontal and vertical velocity fields obtained in the simulation of the backstep-facing flow with mesh 05 for $Re_D = 100$.

The velocity contour plots in Figure 4.18 reveal the characteristic features of the backward-facing step flow at $Re_D = 100$, including the formation of a primary recirculation zone downstream of the step. The horizontal velocity field exhibits a negative region near the lower wall just after the step, corresponding to flow reversal. These features are consistent with those reported in the literature [90–92], validating the physical behavior captured by the simulation.

The horizontal velocity profiles of five meshes were compared with the analytical solution of the flow between flat plates upstream step position. This comparison is shown in Figure 4.19. The velocity profiles and recirculation characteristics obtained with Mesh 04 and Mesh 05 exhibit negligible differences, suggesting mesh independence, as shown in Table 4.6. The velocity profiles upstream the step match

with the parabolic profile at the inlet perfectly, however the velocity profile at the step location deviates from the parabolic profile as shown in Figure 4.20.

From the Figure 4.20, it is evident that the deviation of the velocity profile at the step from the parabolic inlet profile is more pronounced at lower Reynolds numbers. As the Reynolds number increases, this deviation diminishes, consistent with the observations of [93]. This behavior is expected due to the elliptic nature of the Navier–Stokes equations, which allows the influence of the step to propagate upstream into the inlet region. At low Reynolds numbers, this upstream influence is significant, whereas at higher Reynolds numbers, the flow becomes increasingly convection-dominated, reducing the upstream effect. ZANG *et al.* [94] noted that when an entrance section is present, the velocity profile at the point of expansion deviates from the ideal parabolic shape and exhibits a "down-wash" effect — a phenomenon that is clearly observed at low Reynolds numbers, as illustrated in Figure 4.20.
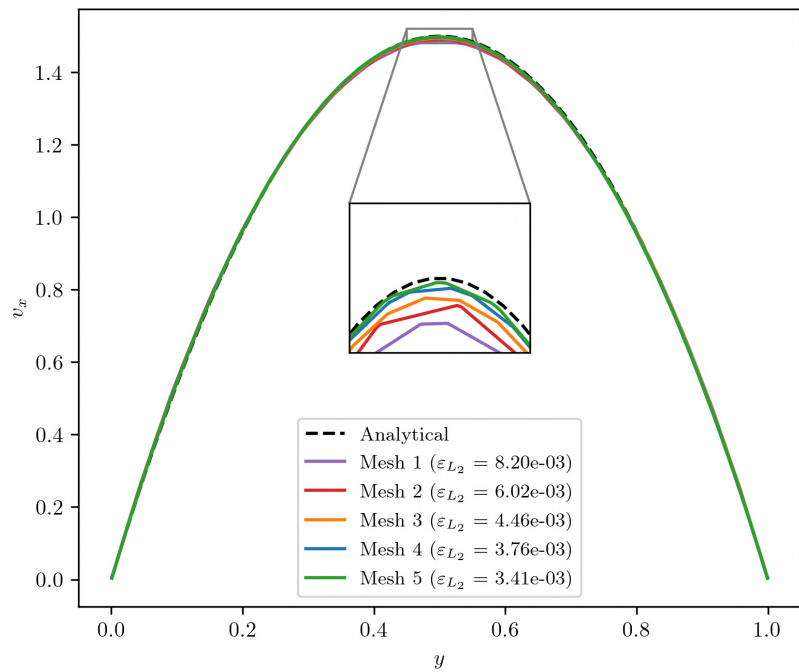

Figure 4.19: Comparison between the horizontal velocity profiles obtained in simulations and the analytical profile upstream the step position.

Table 4.6: Errors in simulations of Backward-Facing Step Flow at $Re = 100$.

| Mesh	ε_{L_2}
Mesh 01	8.20×10^{-3}
Mesh 02	6.02×10^{-3}
Mesh 03	3.76×10^{-3}
Mesh 04	4.33×10^{-3}
Mesh 05	3.41×10^{-3}
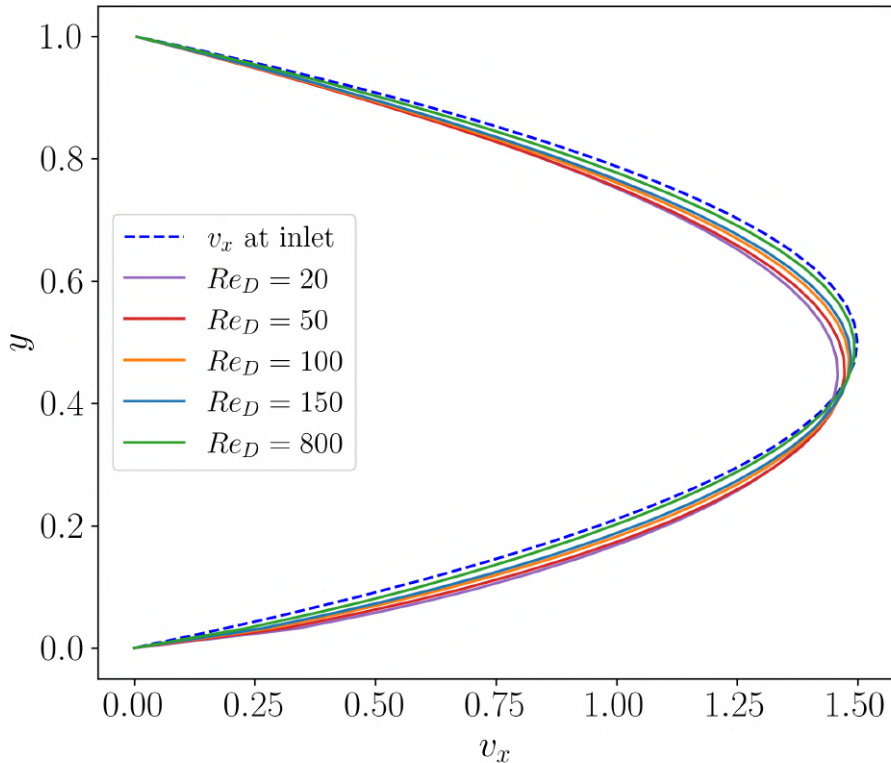
Figure 4.20: Comparison between the horizontal velocity profiles at inlet and at the step location for $Re_D = 20$, $Re_D = 50$, $Re_D = 100$, $Re_D = 150$ and $Re_D = 800$.

The Figures 4.21 and 4.22 present a comparative analysis of streamline patterns for flow over a backward-facing step at four Reynolds numbers ($Re_D = 1, 10, 50, 100$). The upper half of each image in 4.22 shows reference results from the literature [3], while the lower half displays the corresponding numerical results obtained from the present simulations.

At $Re_D = 1$, the flow is in the creeping flow regime, dominated by viscous forces, resulting in smooth streamlines with a very small recirculation bubble immediately downstream of the step. The numerical results successfully reproduce this behavior, accurately capturing the size and position of the primary vortex, which indicates that the solver handles Stokes flow behavior correctly. As the Reynolds number increases

to $Re_D = 10$, inertial effects begin to influence the flow, causing the recirculation bubble to grow in size. The numerical predictions match the reference well, with a good representation of the vortex shape and reattachment length, although minor deviations in streamline density near the reattachment point are observed.

At $Re_D = 50$, the recirculation region becomes substantially larger and more elongated, with a noticeable downstream shift of the vortex core. The numerical simulation captures these features accurately, demonstrating the solver's capability to handle inertia-driven separation and recirculation. At $Re_D = 100$, the recirculation bubble extends even further downstream, and the streamline curvature becomes more pronounced near the step edge. The numerical results remain consistent with the reference, successfully predicting the overall structure and extent of the vortex. Some slight discrepancies in streamline curvature near sharp corners are visible but remain within acceptable limits. Overall, the numerical simulations reproduce the key flow features across all Reynolds numbers with high fidelity, confirming the model's ability to transition smoothly from viscous-dominated to inertia-dominated regimes.
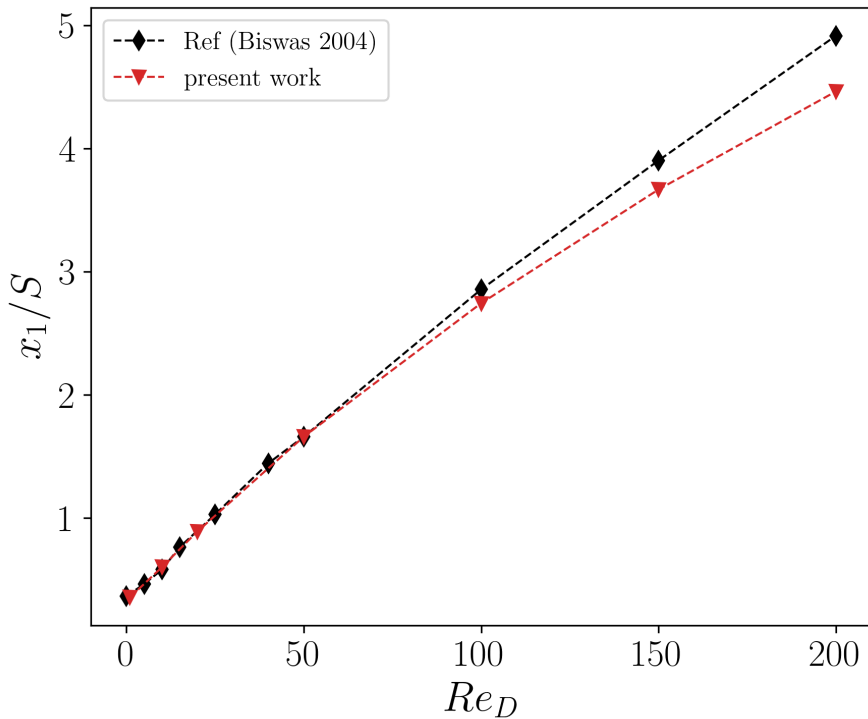

Figure 4.21: Length x_1 of the primary recirculation region behind the backward-facing step normalized by the step height S obtained from the present study and from BISWAS *et al.* [3].

(a) Streamlines for $Re_D = 1$.   (b) Streamlines for $Re_D = 10$.

(c) Streamlines for $Re_D = 50$.   (d) Streamlines for $Re_D = 100$.
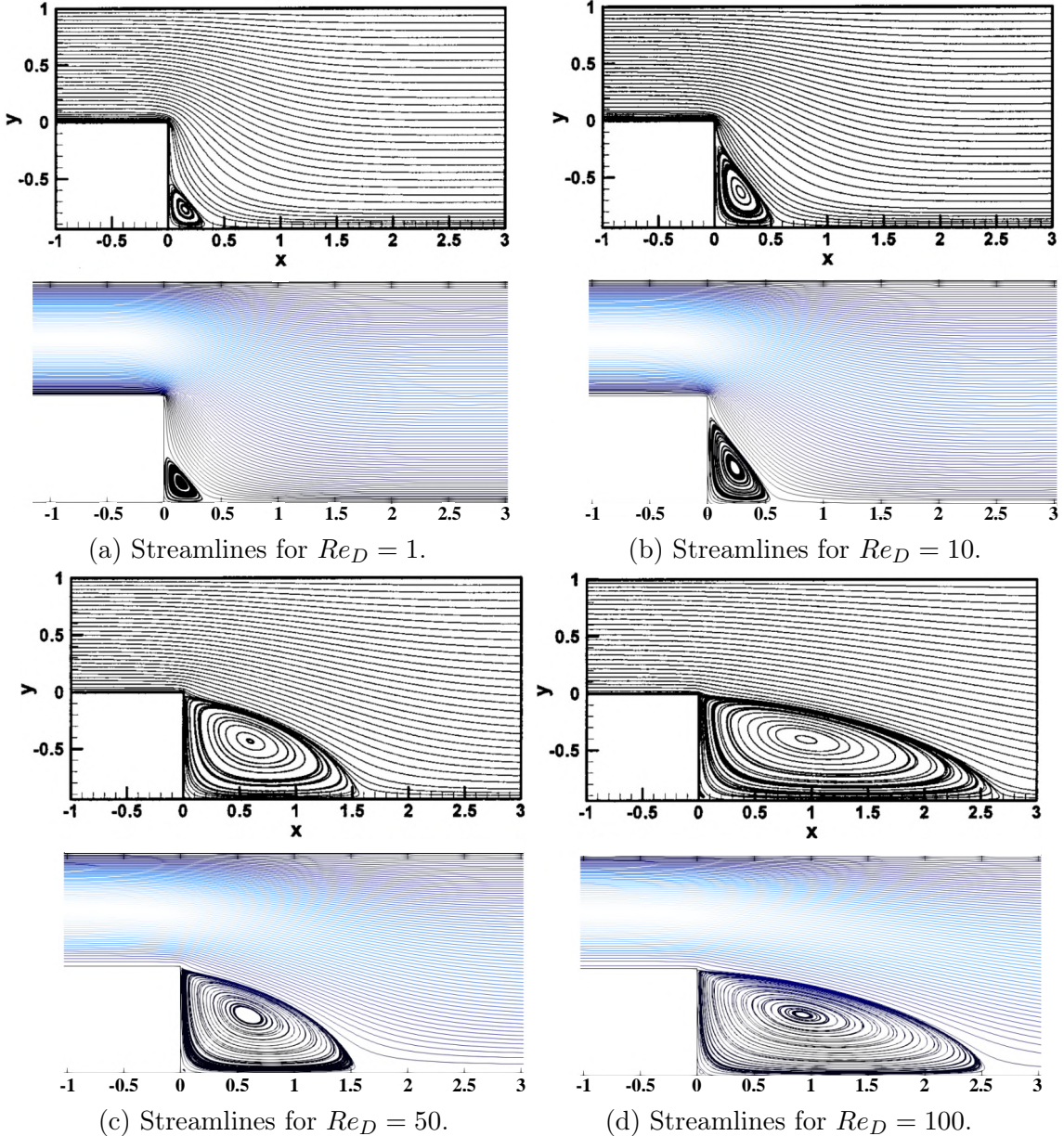
Figure 4.22: Streamline comparisons for different Reynolds numbers obtained in the present work and the literature results [3].

4.2 Two-Phase Miscible Flow

In miscible displacement, the absence of a sharp interface makes the flow strongly dependent on the interplay between advection, diffusion, and viscosity variations, which can give rise to complex mixing patterns and hydrodynamic instabilities. To explore these effects, two complementary configurations were investigated. First, the classical Hele-Shaw cell was simulated to reproduce benchmark cases and validate the ability of the numerical methodology to capture front propagation dynamics under convection-dominated conditions. Subsequently, microchannel geometries representative of micromixing devices were analyzed, focusing on the miscible dis-

57

placement of triglycerides by alcohol. By systematically comparing obstacle-free and obstacle-rich designs, and by evaluating different inlet molar ratios, this study aims to quantify the trade-offs between enhanced mixing and hydrodynamic efficiency, thereby providing a framework for assessing microreactor performance in biodiesel synthesis.

4.2.1 Two-dimensional Hele-Shaw cell

The configuration under investigation consists of the displacement of a more viscous fluid by a less viscous miscible fluid in a Hele-Shaw cell. This classical setup is employed to explore the convective-diffusive dynamics that govern miscible displacement in porous media analogs. The geometry of the domain and the associated boundary conditions regarding the fluids are shown in Figure 4.23. Velocity and pressure boundary conditions are similar to those presented in Figure 4.1 for the flow between flat plates. The computational domain is a two-dimensional rectangular channel of height $L = 1$, in which the more viscous fluid (fluid 2) initially occupies the entire domain, while the less viscous fluid (fluid 1) enters from the left boundary, inducing displacement along the streamwise direction x.

$$\nabla c_1 = \nabla c_2 = 0$$

$L = 1$

$c_1 = 1$
$c_2 = 0$

$$\nabla c_1 = \nabla c_2 = 0$$

$c_2 = 1$

$15L$
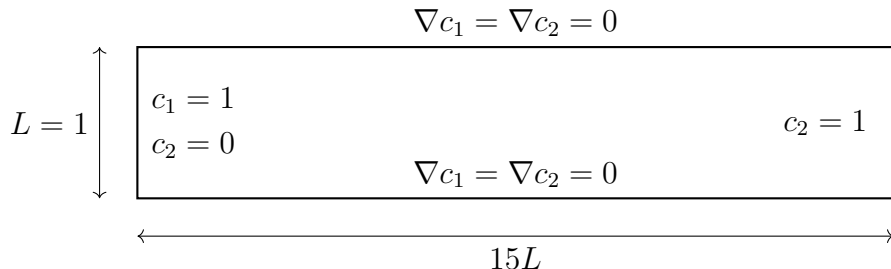
Figure 4.23: Geometry and boundary conditions of Hele-Shaw flow.

To mimic the experimental and theoretical frameworks discussed by [4], the flow is assumed to be incompressible and governed by the Navier-Stokes equations coupled to a convection–diffusion equation for the scalar concentration field c_2, representing the local mass fraction of the more viscous fluid. The viscosity is treated as a function of concentration, typically through an exponential law of the form:

$$\mu(c_2) = \mu_1 e^{Rc_2} \tag{4.4}$$

where μ_1 is the viscosity of the displacing (less viscous) fluid and $R = \ln(\mu_2/\mu_1)$ denotes the viscosity ratio. A high Péclet number regime $Pe \gg 1$ is considered in order to emphasize convection-dominated transport.

An important metric characterizing the displacement dynamics is the velocity of the propagating front, commonly referred to as the tip velocity. In the simulations,

this velocity is measured in a reference frame moving with the mean flow, and it captures the effective advance of the less viscous fluid into the more viscous one. Figure 4.24 shows concentration fields from a numerical simulation for $Pe = 1000$ and $R = 3$ at various times obtained by [4] and the present work. As the flow begins, the velocity field rapidly distorts the concentration profile within the interior of the cell, while changes near the walls occur solely due to diffusion. This evolving concentration field alters the local viscosity, giving rise to a well-defined displacement front of the less viscous fluid. The front advances along the centerline of the Hele-Shaw cell, characterized by a sharp concentration gradient at its tip and gradually diffusing layers along its flanks.

(a) Tip displacement from [4].   (b) Tip displacement from present study.
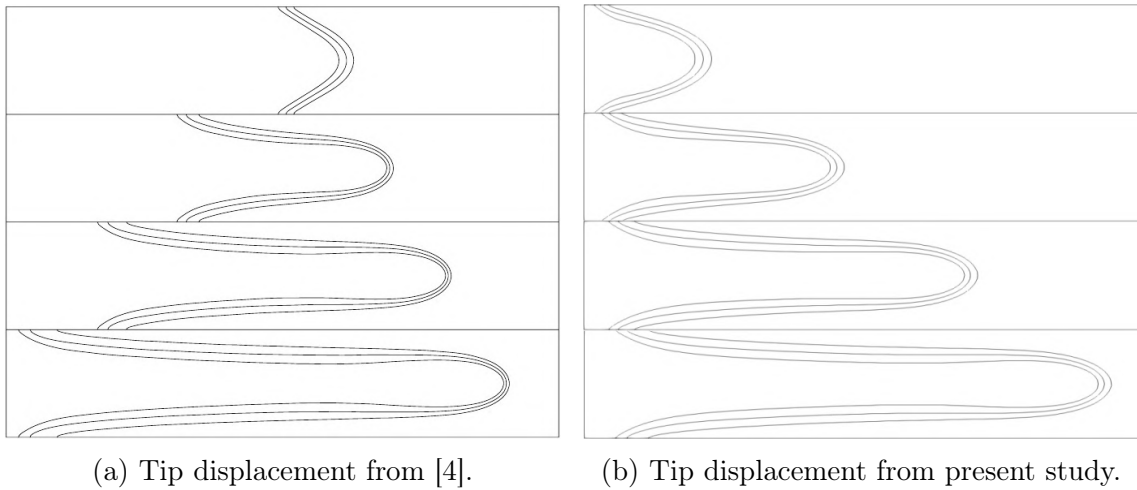
Figure 4.24: Tip displacement comparison at various time-steps for $Pe = 1000$ and $R = 3$.
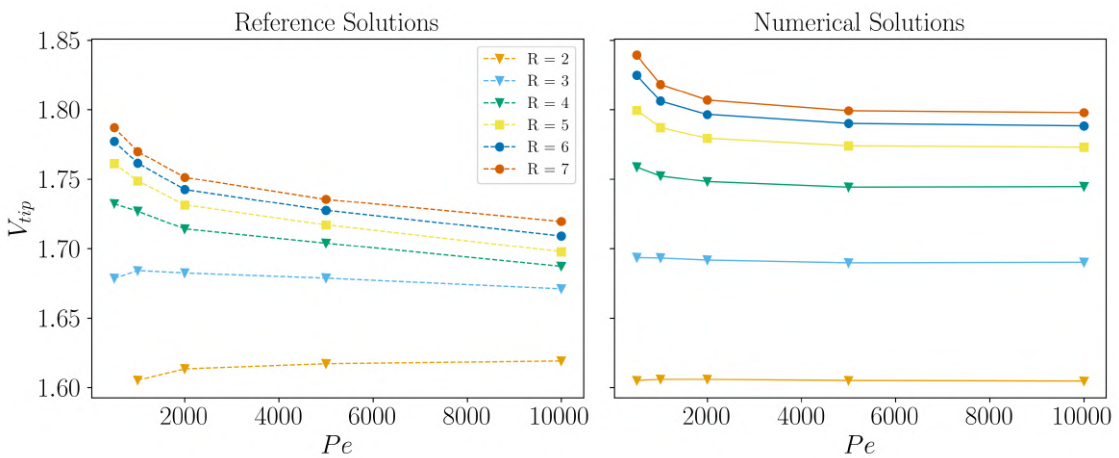
Figure 4.25: Comparison of tip velocity as a function of Pe for different values of R reported in [4] with results from the present study.

Figure 4.25 compares the reference data from [4] with the present numerical results for the normalized tip velocity, V_{tip}, as a function of the Péclet number for

different viscosity ratios R. The tip velocity reflects the effective propagation rate of the miscible front and thus encapsulates the interplay between convective transport and viscous coupling.

In the reference solutions (left panel), the tip velocity decreases systematically with increasing Péclet number for all viscosity ratios. This trend highlights the fact that at higher Pe diffusion becomes progressively less effective in smoothing the concentration gradients at the advancing tip, leading to stronger viscous coupling and, consequently, a reduction in front propagation speed. The dependence on viscosity ratio is also evident: larger R values correspond to higher V_{tip}, indicating that sharper viscosity contrasts enhance the destabilizing effect of the less viscous fluid displacing the more viscous one.

The numerical solutions (right panel) reproduce the same qualitative trends. For all viscosity ratios, the computed V_{tip} decreases monotonically with Pe and approaches an asymptotic value at large Pe, consistent with convection-dominated transport. Quantitative agreement with the reference data is generally good, particularly for intermediate viscosity ratios ($R = 4$–6). For the extreme cases, small discrepancies are observed: at low viscosity contrast ($R = 2$) the numerical results slightly underestimate the tip velocity, while at high viscosity contrast ($R = 7$) they slightly overestimate it. These deviations may stem from discretization effects and the sensitivity of the exponential viscosity law (4.4) to small variations in concentration near the tip.

Overall, the results confirm that the present numerical framework is able to capture the essential dynamics of miscible viscous fingering in Hele-Shaw configurations. The consistent dependence of V_{tip} on both Pe and R demonstrates the robustness of the methodology, while the remaining differences with the reference data provide useful guidance for further refinement of spatial resolution and stabilization strategies in high–Pe regimes.

4.2.2   Microchannel Flow

Five microchannel geometries were simulated to evaluate their ability to enhance mixing and conversion during the miscible displacement of triglyceride (TG, $\rho_{TG \text{ at } 50\ °C} = 899.40\ kg/m^3$, $\mu_{TG \text{ at } 50\ °C} = 2.13e{-}2\ Pa.s$) by alcohol (A, $\rho_{A \text{ at } 50\ °C} = 763\ kg/m^3$, $\mu_{A \text{ at } 50\ °C} = 6.88e - 4\ Pa.s$). The geometries considered were:

1. Straight Channel (SMC) – baseline configuration with no obstacles (Figure 4.26a). It has a height H, with an aspect ratio (L/H) of 20.92. The same aspect ratio was used for the other geometries.

2. Aligned Circular Obstructions (MCE) – 20 evenly spaced ($L_1 = 0.8H$) circular obstructions ($D_1 = 0.4H$) aligned in the channel centerline (Figure 4.26b).

3. Alternating Circular Obstructions (ACE) – staggered array of circular obstructions of different diameters ($D_2 = 0.4H$ and $D_3 = 0.3H$), separated horizontally by $L_2 = 0.6H$, and vertically by $L_3 = 0.4H$ (Figure 4.26c).

4. Rectangular Obstructions (MSE) – periodic alternated rectangular blocks ($L_4 = 0.66H$ and $L_5 = 0.066H$), separated by $L_6 = 0.7H$, starting at $x = 2.4H$ (Figure 4.26d).

5. Triangular Baffles with Circular Obstructions (SR) – combination of triangular baffles ($L_7 = 0.3H$ and $L_8 = 1.2H$) and circular obstructions ($D_4 = 0.4H$) promoting advection (Figure 4.26e).

Two inlet conditions were analyzed to represent different reactant availability:

- 1TG:9A molar ratio, converted into a one-dimensional entry profile for c_{TG} and c_A ($c_{TG} = 1$ and $c_A = 0$ in $0.323 < y_i < 1.0$, and $c_{TG} = 0$ and $c_A = 1$ in $0.0 < y_i < 0.323$).

- 1TG:12A molar ratio, similarly converted into a one-dimensional entry ($c_{TG} = 1$ and $c_A = 0$ in $0.427 < y_i < 1.0$, and $c_{TG} = 0$ and $c_A = 1$ $0.0 < y_i < 0.427$).

(a) Geometry 1: Straight Microchannel (SMC)

(b) Geometry 2: Aligned Circular Obstructions (MCE)

(c) Geometry 3: Alternating Circular Obstructions (ACE).

(d) Geometry 4: Rectangular Obstructions (MSE).

(e) Geometry 5: Triangular Baffles with Circular Obstructions (SR).

Figure 4.26: Five different microchannel geometries evaluated in the present study.

Simulations were carried out for several Reynolds numbers ($Re = 1$-30), and the alcohol concentration profile was measured at different sections along the geometries ($x/H = 0.01, 2.00, 4.95, 5.00, 8.00, 11.90, 15.00, 17.50, 19.20, 20.91$). The Reynolds number was computed using the Triglyceride properties. In order to comprehend the flow behaviour in the following simulations, one can refer to the following correspondence:

- $Re = 1 \rightarrow Re_A = 26.26$.

- $Re = 5 \rightarrow Re_A = 131.32$.

- $Re = 10 \rightarrow Re_A = 262.64$.

- $Re = 20 \rightarrow Re_A = 525.28$.

- $Re = 25 \rightarrow Re_A = 656.60$.

- $Re = 30 \rightarrow Re_A = 787.92$.

where Re_A is the Reynolds number computed with alcohol properties. Mesh convergence studies were also performed to evaluate the numerical diffusivity associated with the grid resolution for each geometry configuration.

Straight Channel (No Obstructions)

The straight microchannel (SMC) was considered as the baseline geometry, where molecular diffusion was the sole mechanism driving cross-stream mixing. Figure 4.27 illustrates an example of the unstructured triangular mesh employed for the discretization of the computational domain.
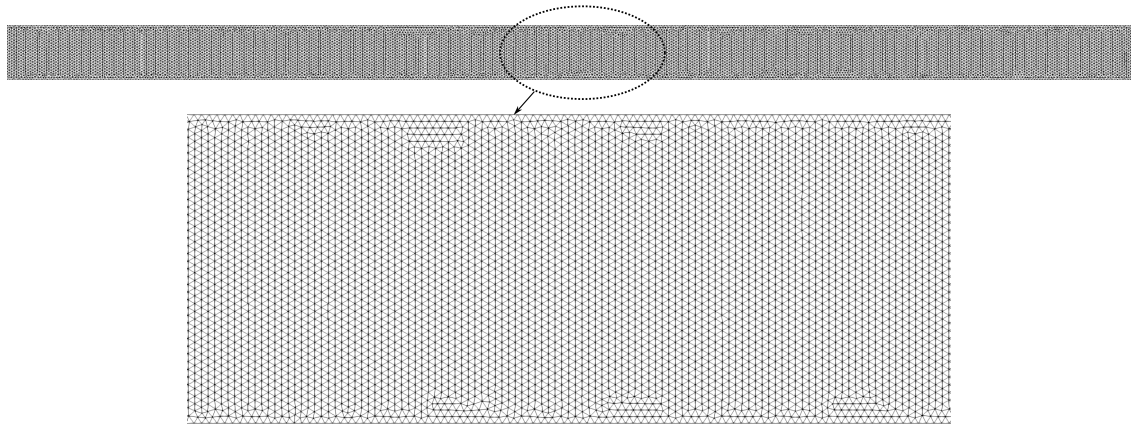

Figure 4.27: Unstructured mesh with triangular elements of the microchannel without obstacles (SMC).

To assess the influence of mesh resolution on the prediction of alcohol concentration along the channel, four different meshes were tested. The number of nodes and elements for each mesh, as well as the corresponding computational (CPU) time, are summarized in Table 4.7. As expected, the computational cost increased with mesh refinement.

Table 4.7: Straight Microreactor mesh statistics and computational time for $Re = 10$.

Mesh	Nodes	Elements	CPU time (h)	Time step [-]
SMC 01	10277	19674	9.42	0.01
SMC 02	15736	30374	14.10	0.01
SMC 03	27816	54166	29.28	0.01
SMC 04	39816	77876	45.87	0.01

Although finer meshes required higher computational times, their impact on the predicted concentration fields was significant. As shown in Figure 4.28, the mesh

resolution strongly influenced the alcohol distribution, which in turn affected the velocity field along the microchannel, as further evidenced in Figure 4.29. Moreover, the use of finer meshes reduced numerical diffusion and allowed sharper concentration gradients to be maintained for the same Reynolds number.
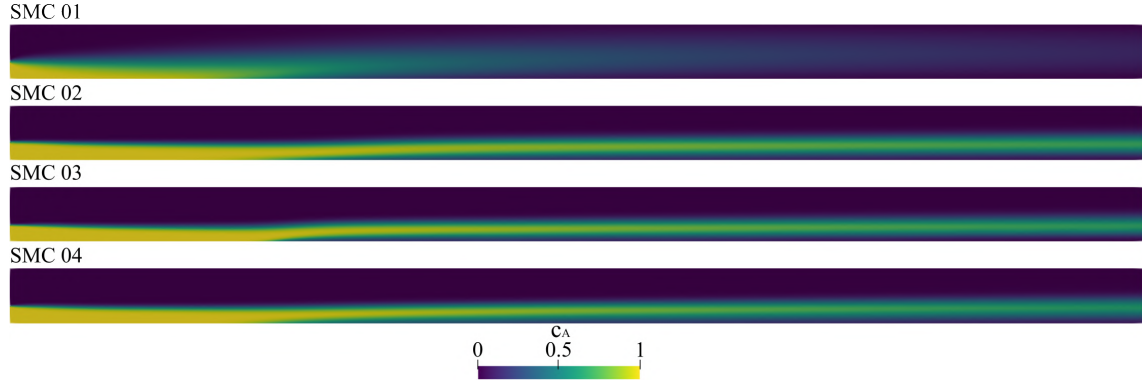

Figure 4.28: Alcohol contour for different meshes in SMC, with $Re = 10$.

Because ethanol entered through the lower section of the channel, the velocity profile deviated from that of a single-phase flow, being skewed towards the region of higher alcohol concentration.

(a) c_A and v_x profile for $Re_{TG} = 10$ at $X = 5H$.

(b) c_A and v_x profile for $Re_{TG} = 10$ at $X = 15H$.

(c) c_A and v_x profile for $Re_{TG} = 10$ at $X = 20.91H$.
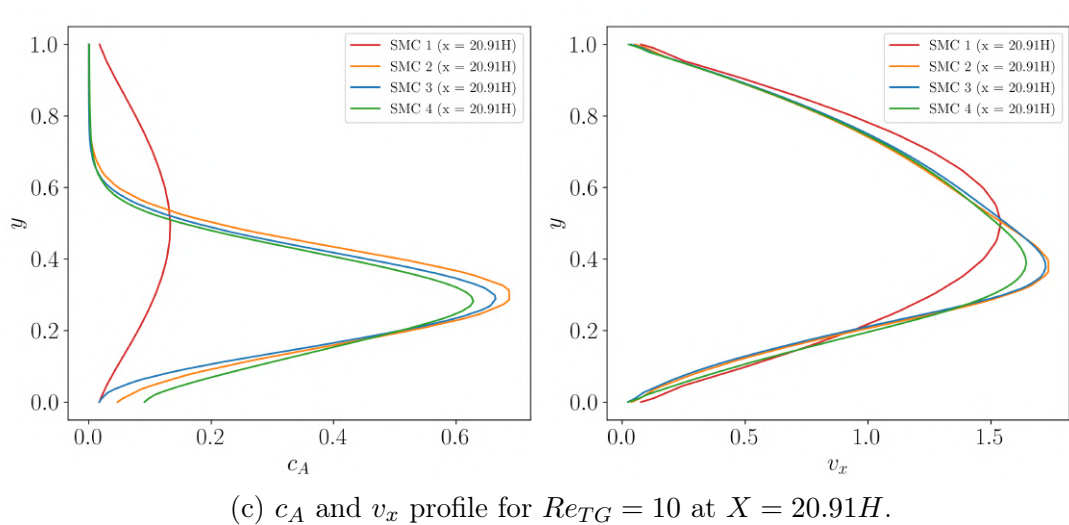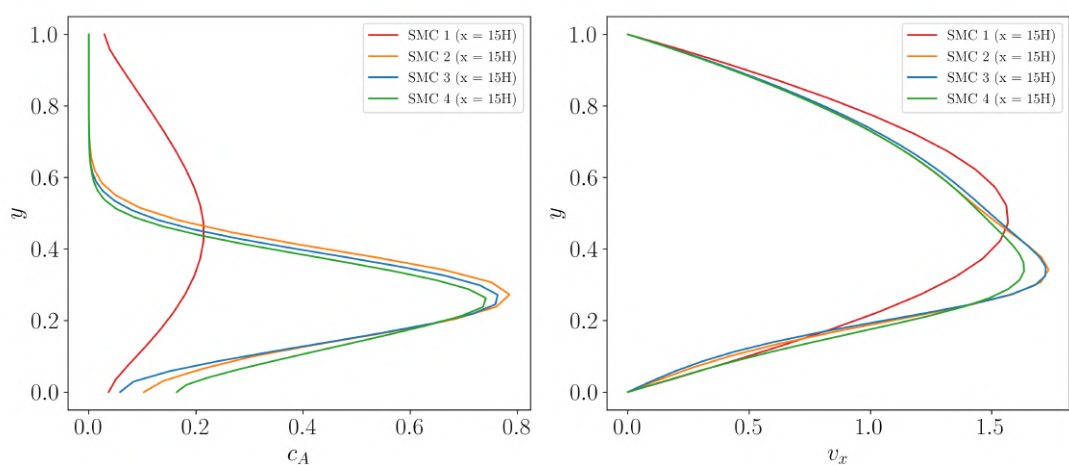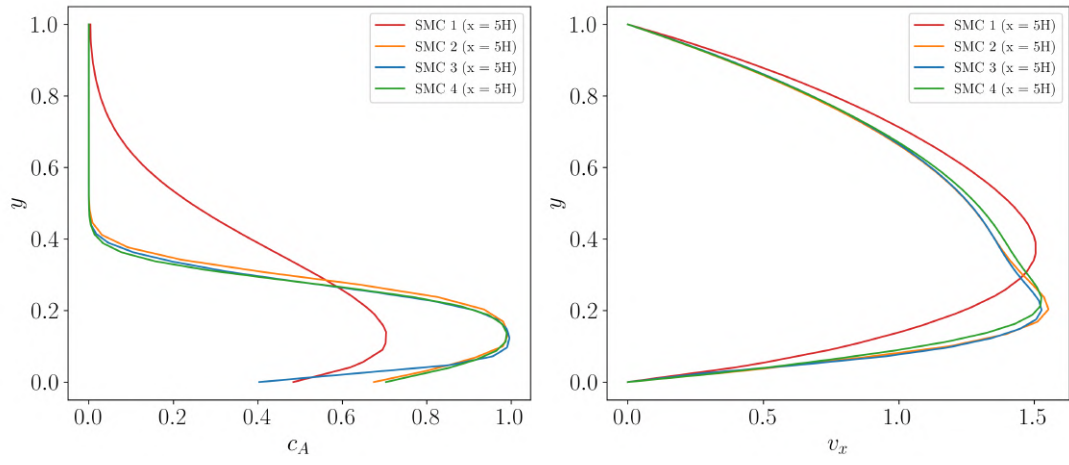
Figure 4.29: SMC v_x and c_A profiles at various X positions along the microreactor for $Re = 10$.

Using the refined mesh (SMC 04), additional simulations were carried out to investigate the influence of the Reynolds number and inlet molar ratio on the mixing behavior of the baseline geometry.

The performance of the micromixer was characterized through the mixing index and the performance index. The degree of mixing between fluid 1 (triglycerides) and fluid 2 (ethanol) was quantified using the standard deviation of the mass fraction of fluid 2 across a cross-section normal to the flow direction (a perpendicular line in this study), as expressed in Equation 4.5.

$$\sigma = \sqrt{\frac{\sum \left(Y_i - \bar{Y}\right)^2}{N}} \tag{4.5}$$

Here, σ denotes the variance of the mass fraction, Y_i is the mass fraction at sampling point i, $\bar{Y}$ is the cross-sectional average, and N is the number of sampling points (500 in the present study). The fluid mixing efficiency was then determined using Equation 4.6.

$$MI = 1 - \sqrt{\frac{\sigma^2}{\sigma_{\max}^2}} \tag{4.6}$$

In this expression, M represents the mixing index and $\sigma_{\max}^2$ is the maximum variance, corresponding to the mass fraction variance at the channel inlet. The mixing index ranges from 0 (complete segregation) to 1 (perfect mixing) [95].

To further assess efficiency, the Performance Index (PI) was employed, which accounts for both mixing enhancement and hydraulic losses. An effective micromixer should achieve a high mixing index with minimal pressure drop [96, 97]. The PI is defined as the ratio between the mixing index and the pressure drop along the channel, as given in Equation 4.7.

$$PI = \frac{MI}{\Delta P} \tag{4.7}$$

where ΔP is the pressure drop across the mixing channel.

The alcohol concentration contours shown in Figures 4.30 and 4.31 clearly show that, at low Reynolds numbers, the concentration gradient between alcohol and triglyceride remained smooth, with diffusion producing a wider interfacial region. At higher Reynolds numbers, although the advection rate increased, the reduced residence time prevented effective homogenization, leaving stratified streams along the channel. The mixing index results in Figure 4.32 confirm that mixing improved only slowly with channel length, reaching low outlet values compared to obstacle-based geometries. Nevertheless, the straight channel consistently achieved the highest performance index across all cases (Table 4.12), with a maximum PI of 0.359 at $Re = 30$

for the 1:9 molar ratio. This reflects its minimal pressure drop, making SMC the most hydraulic-efficient geometry despite its poor mixing.
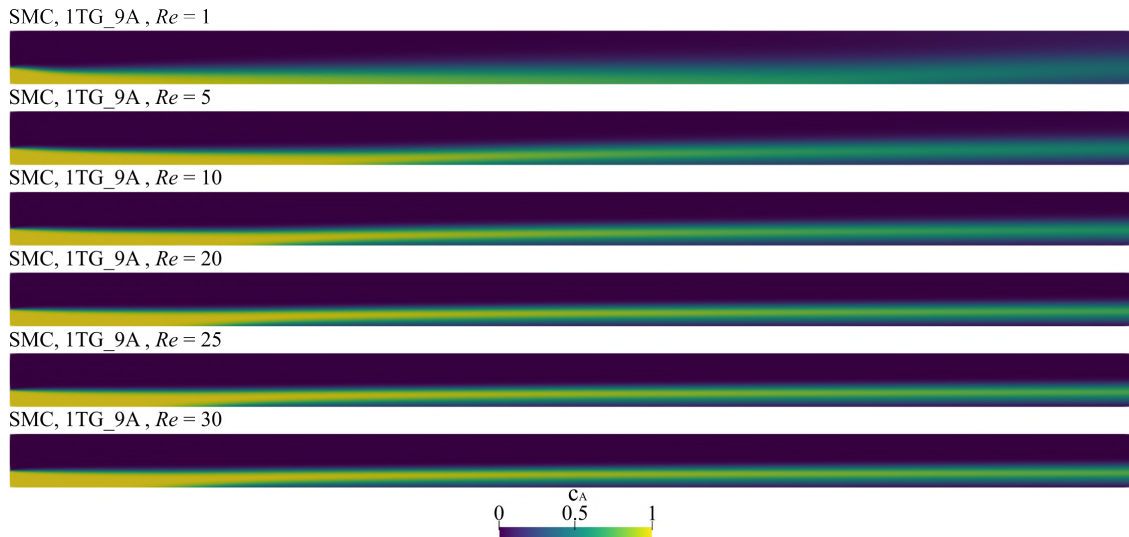
Figure 4.30: Alcohol contour for different Reynolds numbers in SMC with the molar ratio 1TG to 9A.
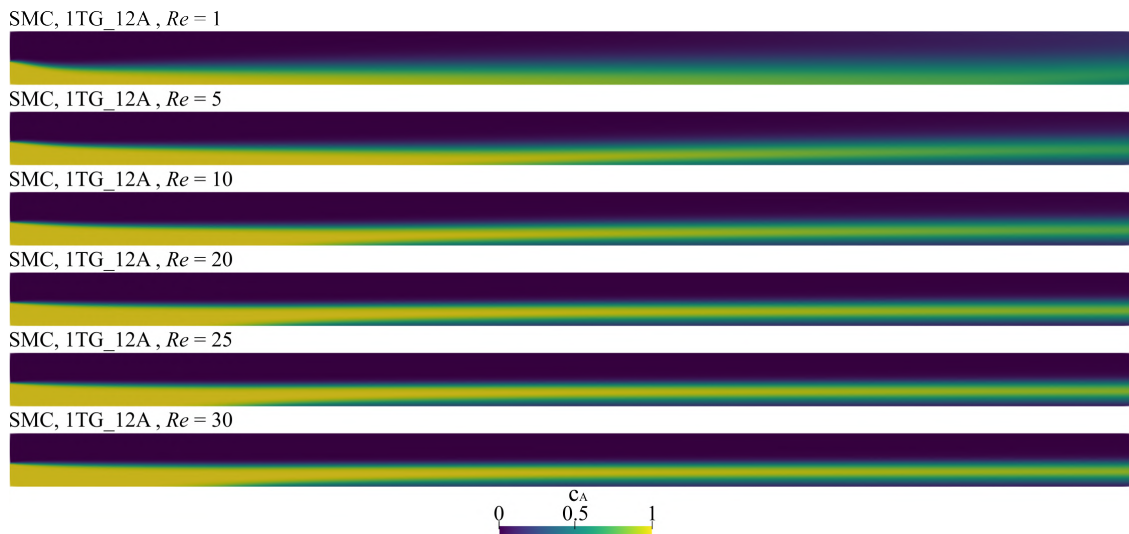
Figure 4.31: Alcohol contour for different Reynolds numbers in SMC with the molar ratio 1TG to 12A.
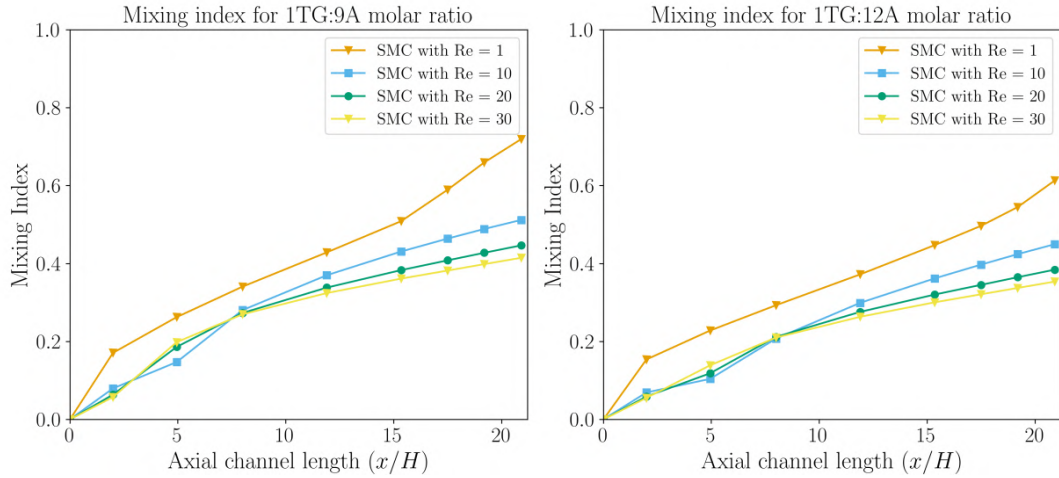
Figure 4.32: Mixing index as a function of axial SMC channel length for different Reynolds numbers and molar ratios.

Aligned Circular Obstructions

The geometry of the microreactor with aligned circular obstructions (MCE) is shown in Figure 4.33, where the evenly spaced obstacles generates narrow passages along the channel. The unstructured triangular mesh resolved the curved surfaces with local refinement, ensuring accurate representation of the obstruction boundaries.
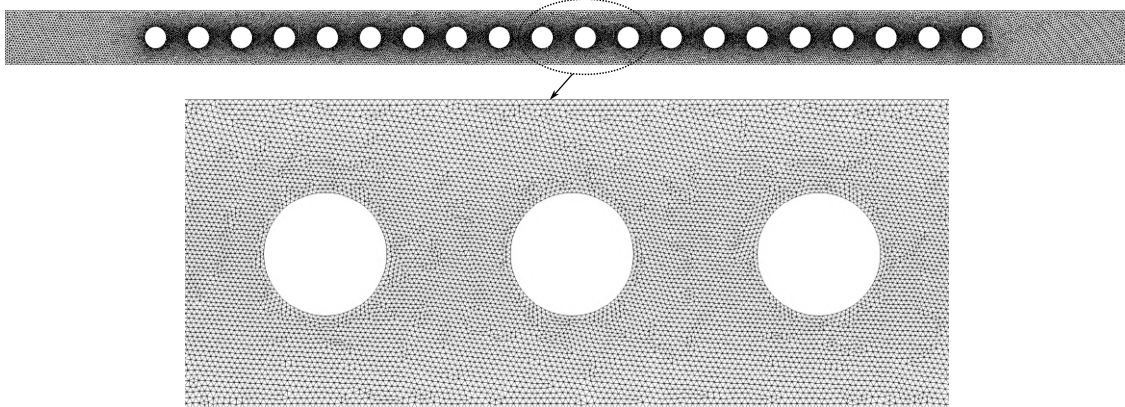

Figure 4.33: Unstructured mesh with triangular elements of the microchannel with aligned circular obstructions (MCE).

The mesh sensitivity analysis, presented in Figure 4.34, demonstrated that the alcohol concentration field stabilized with increasing refinement, particularly from MCE 03 onward, where no significant variations were observed.

MCE 01

MCE 02

MCE 03

MCE 04

c_A
0   0.5   1
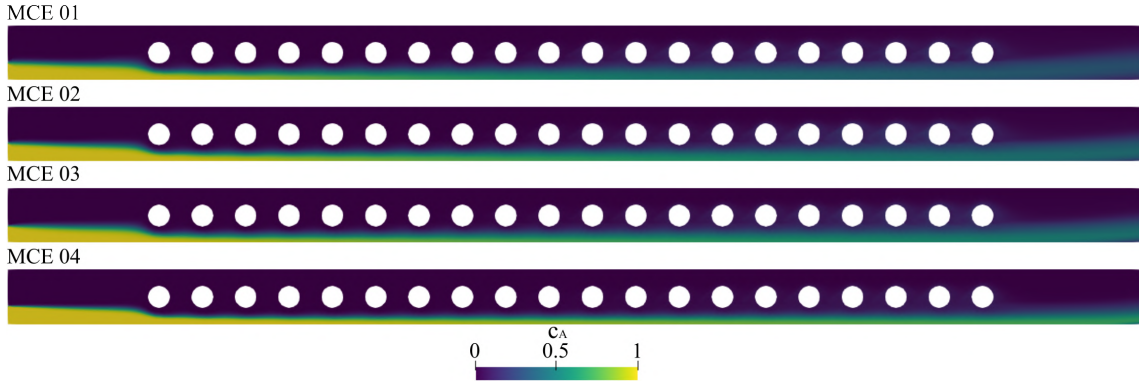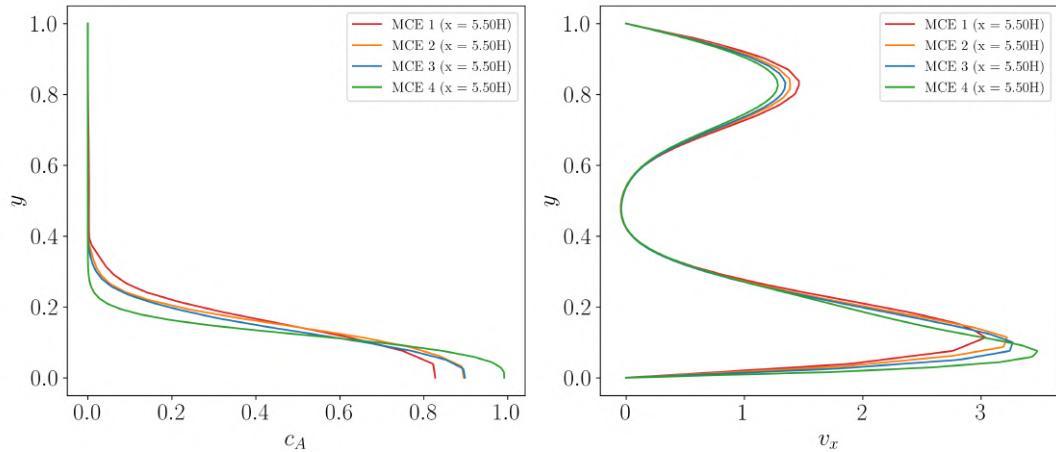
Figure 4.34: Alcohol contour for different meshes in MCE.

Table 4.8 quantifies the computational cost, showing that the number of nodes and elements increases substantially with refinement, leading to CPU times that nearly double between consecutive meshes. For instance, MCE 01 required 10.75 hours, whereas MCE 04 demanded over 69 hours for the same simulation at $Re = 10$. This highlights the trade-off between accuracy and computational cost, which is especially critical for geometries with multiple obstructions. Despite the high computational cost, refinement proved essential for capturing wake regions and narrow gaps between obstructions.
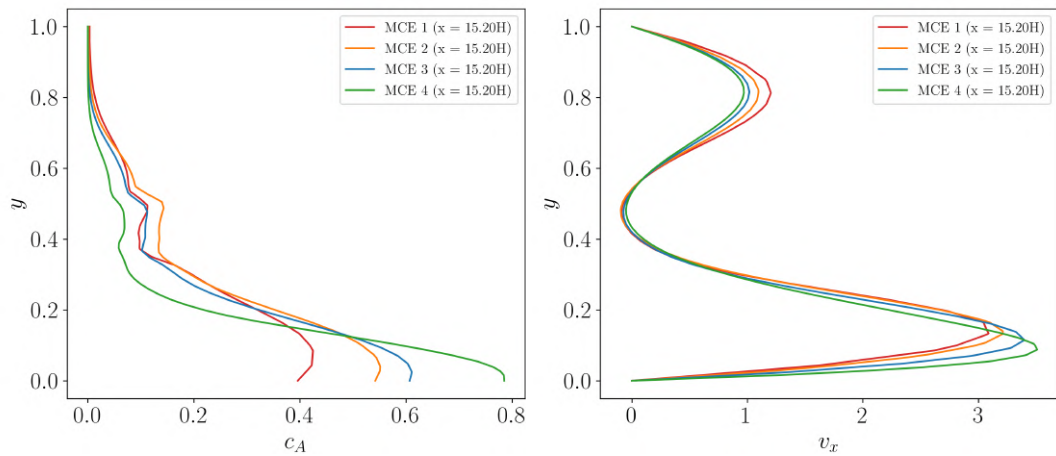
Table 4.8: Aligned Circular Obstructions Microreactor mesh statistics and computational time for $Re = 10$.

Mesh	Nodes	Elements	CPU time (h)	Time step [-]
MCE 01	22268	42416	10.75	0.01
MCE 02	27577	52816	26.05	0.01
MCE 03	36968	71230	38.25	0.01
MCE 04	71804	139774	69.57	0.01
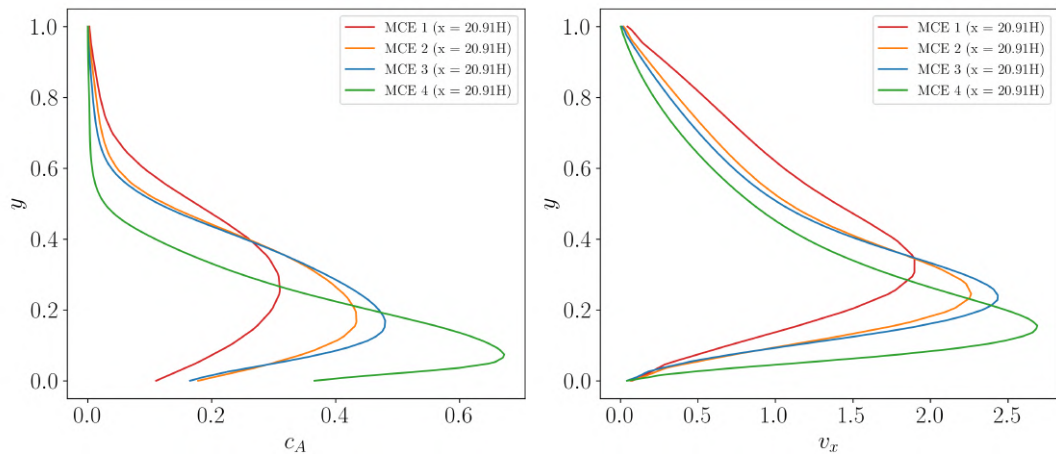
The axial profiles of alcohol concentration and velocity at $X = 5H$, $X = 15H$, and $X = 20.91H$ for $Re = 10$ were illustrated in Figure 4.35. At $X = 5H$, the alcohol front was only beginning to penetrate the triglyceride-rich region, and the velocity field exhibited the acceleration of fluid between the obstructions with wake zones forming downstream. By $X = 15H$, the alcohol distribution showed enhanced penetration into the upper region of the channel, and the velocity contours indicated more defined wake recirculations. At $X = 20.91H$, the alcohol was more evenly spread, although some stratification persisted, indicating that aligned circular obstacles improved mixing relative to the straight channel, but the process remained incomplete at this Reynolds number.

(a) c_A and v_x profile for $Re_{TG} = 10$ at $X = 5H$.

(b) c_A and v_x profile for $Re_{TG} = 10$ at $X = 15H$.

(c) c_A and v_x profile for $Re_{TG} = 10$ at $X = 20.91H$.

Figure 4.35: MCE v_x and c_A profiles at various X positions along the microreactor for $Re = 10$.

The streamline visualizations at different Reynolds numbers (Figure 4.36) re-

vealed that flow recirculations intensified with increasing Re. At $Re = 1$, stream-lines followed smooth paths around the obstructions, with weak disturbances. At $Re = 10$, wakes were clearly observed, while at $Re = 20$ and $Re = 30$, stronger vortices were generated, enhancing lateral transport.
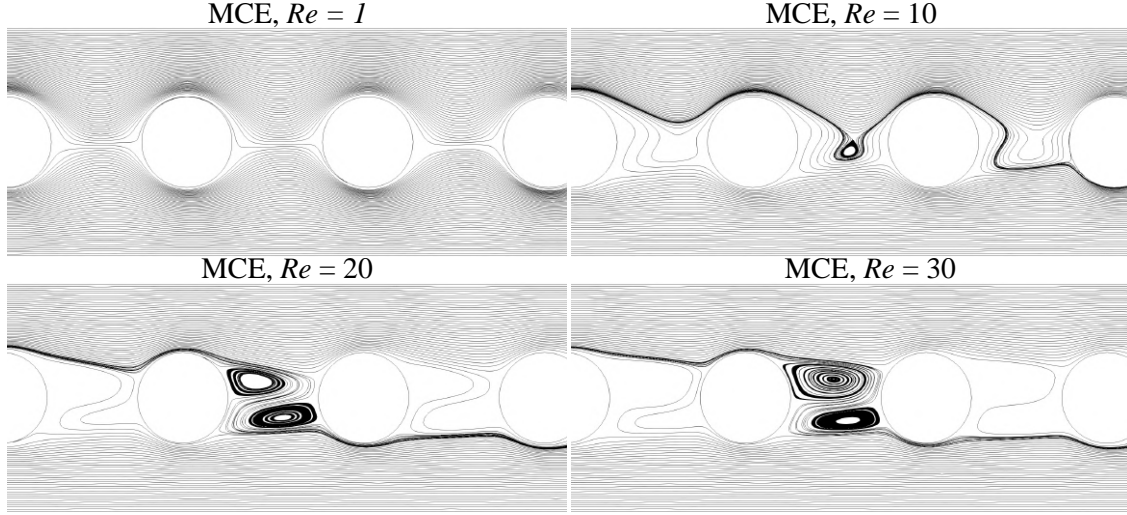

Figure 4.36: Streamlines of MCE for Reynolds number of 1, 10, 20 and 30.

The alcohol contours in Figures 4.37 and 4.38 confirmed that increasing Re improved the spreading of alcohol into the triglyceride-rich region, although homogenization occurred progressively along the channel.
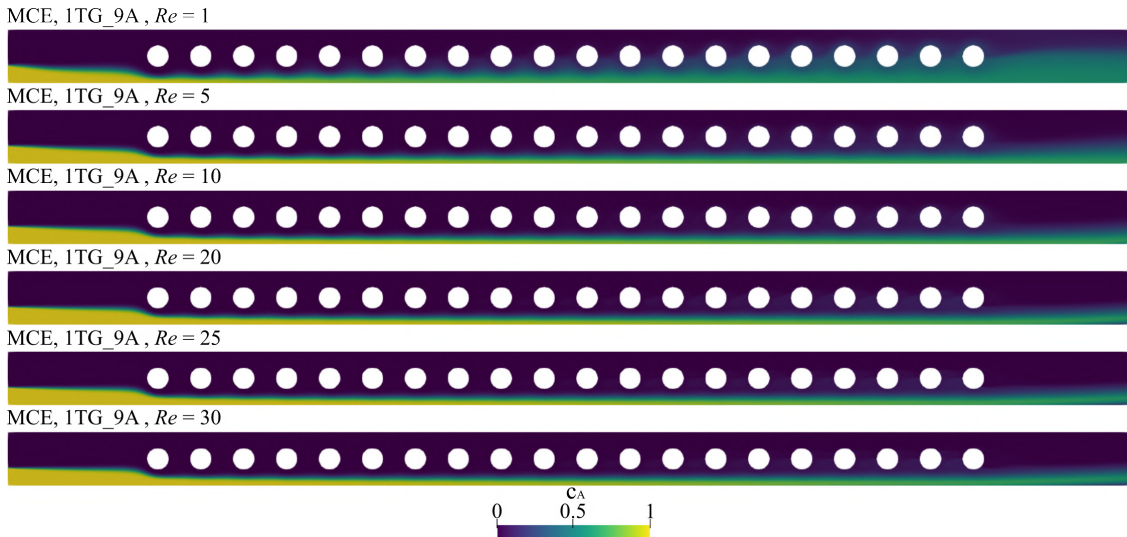
Figure 4.37: Alcohol contour for different Reynolds numbers in MCE with the molar ratio 1TG to 9A.
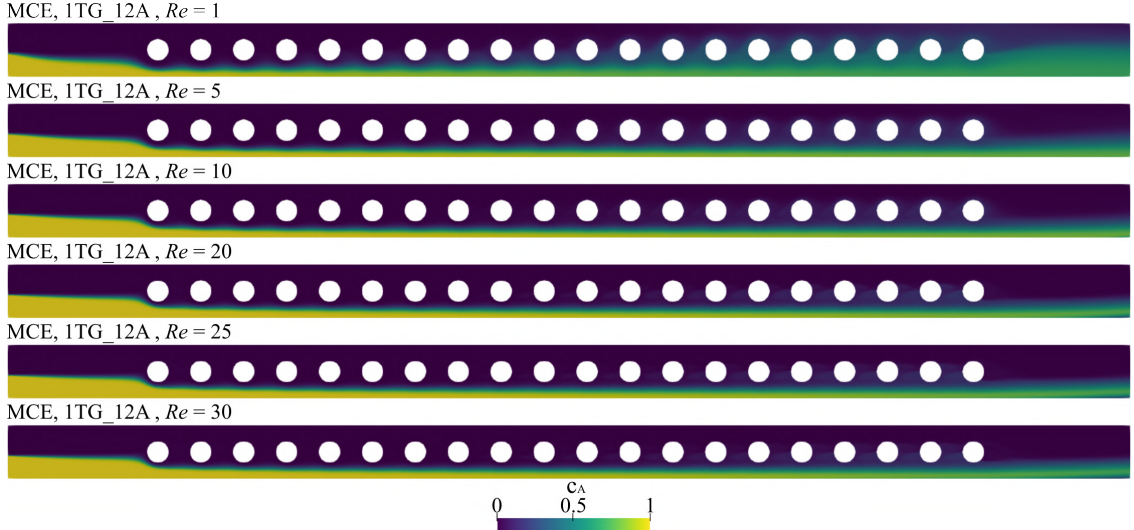
Figure 4.38: Alcohol contour for different Reynolds numbers in MCE with the molar ratio 1TG to 12A.

Finally, the mixing index results in Figure 4.39 showed that higher Reynolds numbers accelerated homogenization, particularly for the 1TG:12A molar ratio. Nevertheless, mixing remained limited compared to other geometries, since aligned obstacles promoted mainly axial stretching of the interface with relatively weak cross-stream mixing.
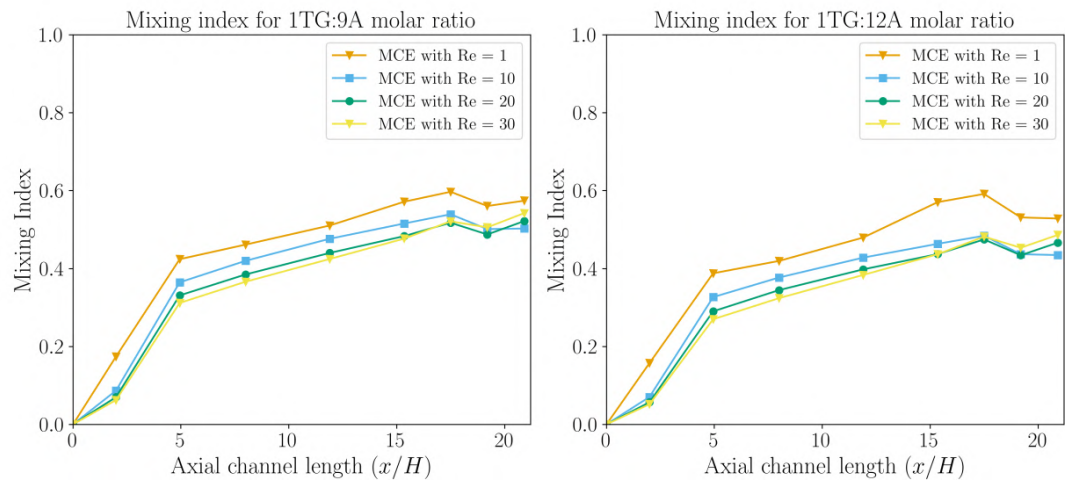
Figure 4.39: Mixing index as a function of axial MCE channel length for different Reynolds numbers and molar ratios.

Alternating Circular Obstructions

The microchannel geometry with alternating circular obstructions (ACE) is shown in Figure 4.40, where the staggered arrangement of the obstacles introduces additional asymmetry compared to the MCE case. The unstructured triangular

mesh resolves the curved surfaces with local refinement around the obstructions, ensuring an accurate representation of the narrow passages.
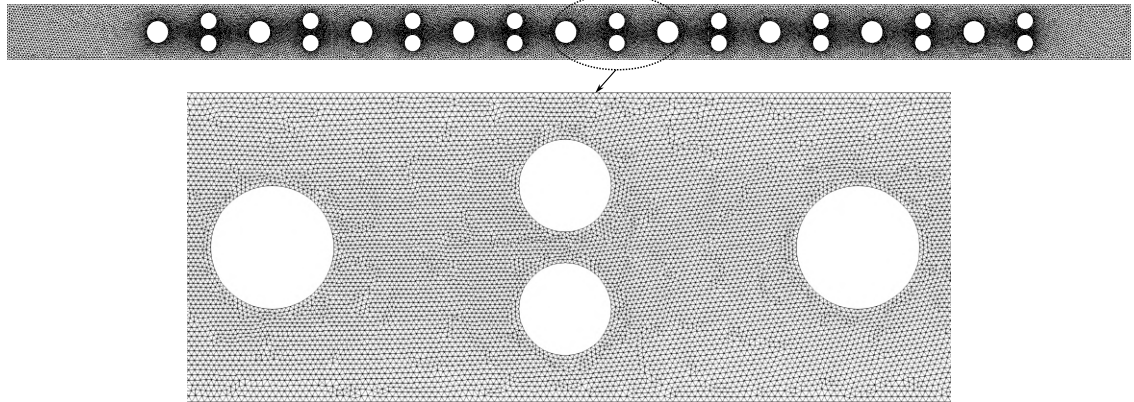
Figure 4.40: Unstructured mesh with triangular elements of the microchannel with alternating circular obstructions (ACE).

The mesh sensitivity analysis, presented in Figure 4.41, shows that the alcohol concentration field stabilizes with increasing refinement, particularly from ACE 03 onward, where the profiles no longer exhibit significant changes.
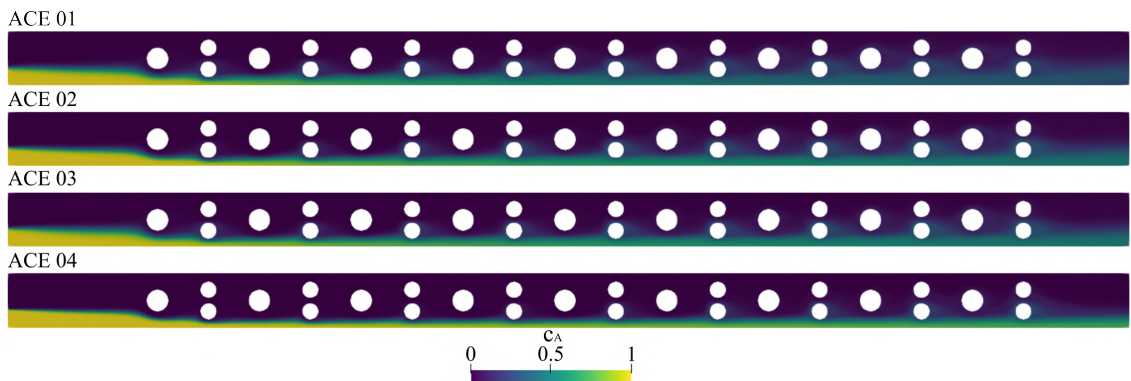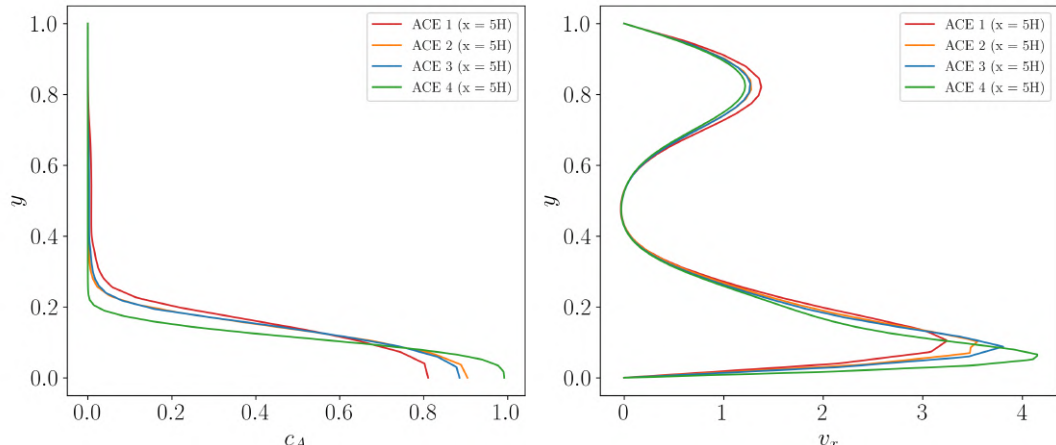
Figure 4.41: Alcohol contour for different meshes in ACE.

The computational demand is reported in Table 4.9, which indicates CPU times ranging from 11.75 h for ACE 01 to over 35 h for ACE 04 at $Re = 10$. Although the computational cost increases considerably, the gains in solution accuracy justify the choice of refined meshes for quantitative analysis.
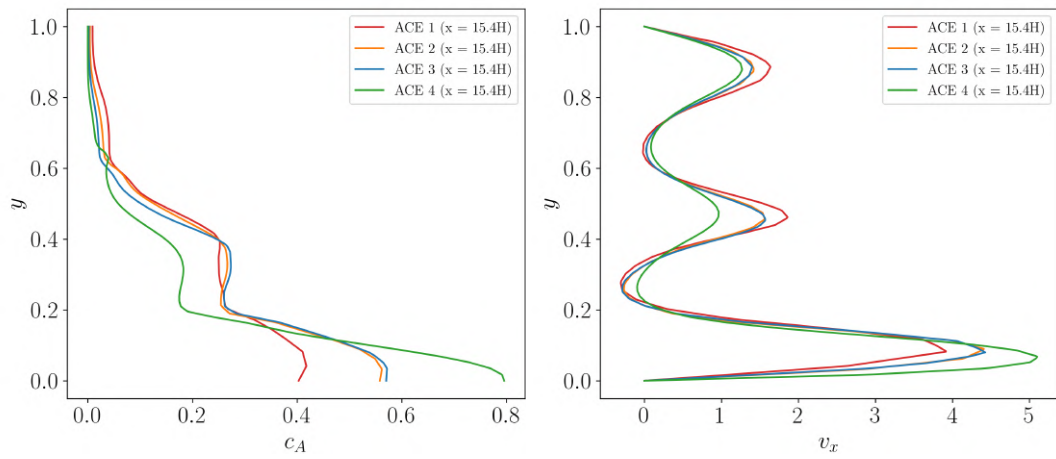
Table 4.9: Alternating Circular Obstructions Microreactor mesh statistics and computational time for $Re = 10$.

Mesh	Nodes	Elements	CPU time (h)	Time step [-]
ACE 01	24446	46626	11.75	0.01
ACE 02	29777	57070	14.17	0.01
ACE 03	40030	77108	18.67	0.01
ACE 04	75073	146098	35.23	0.01
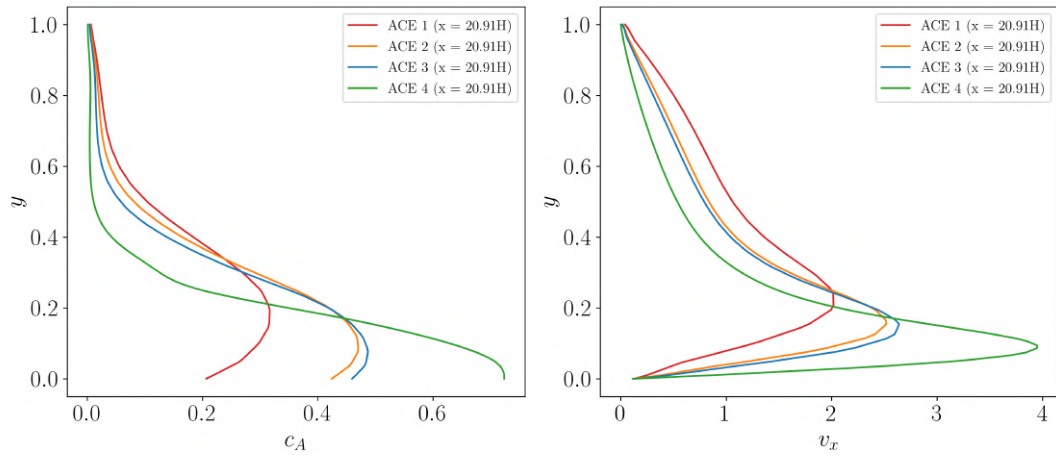
The concentration and velocity distributions at selected axial positions ($X = 5H$, $X = 15H$, and $X = 20.91H$) for $Re = 10$ are shown in Figure 4.42. At $X = 5H$, the flow already exhibits pronounced asymmetry due to the staggered positioning of the obstacles, generating transversal velocity components absent in the MCE configuration. By $X = 15H$, the alcohol concentration spreads much more effectively across the channel height, and the velocity profile shows alternating high- and low-speed regions induced by the circular obstructions. At $X = 20.91H$, the concentration is substantially homogenized compared to the aligned obstruction case, demonstrating that the staggered arrangement enhances cross-stream mixing by forcing repeated lateral deviations in the flow.

(a) c_A and v_x profile for $Re_{TG} = 10$ at $X = 5H$.

(b) c_A and v_x profile for $Re_{TG} = 10$ at $X = 15H$.

(c) c_A and v_x profile for $Re_{TG} = 10$ at $X = 20.91H$.

Figure 4.42: ACE v_x and c_A profiles at various X positions along the microreactor for $Re = 10$.

The streamline plots at different Reynolds numbers (Figure 4.43) reveal how the

staggered obstacles increase the complexity of flow structures compared to MCE. At $Re = 1$, mixing is still limited, but the wakes generated by alternating obstructions deflect the streamlines laterally, enhancing fluid interpenetration. At $Re = 10$ and higher, the wakes extend further downstream, producing alternating recirculation zones that substantially promote transversal exchange. This is clearly visible in Figures 4.44 and 4.45, where the alcohol concentration contours show broader spreading and earlier homogenization compared to MCE. The molar ratio 1TG:12A enhances these effects due to the larger alcohol inlet region.
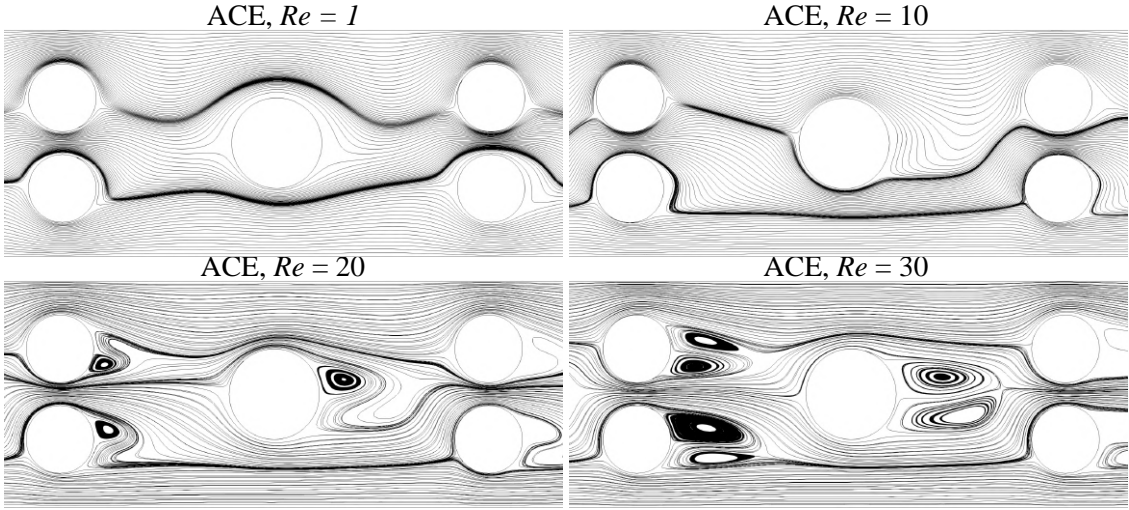
Figure 4.43: Streamlines of ACE for Reynolds number of 1, 10, 20 and 30.
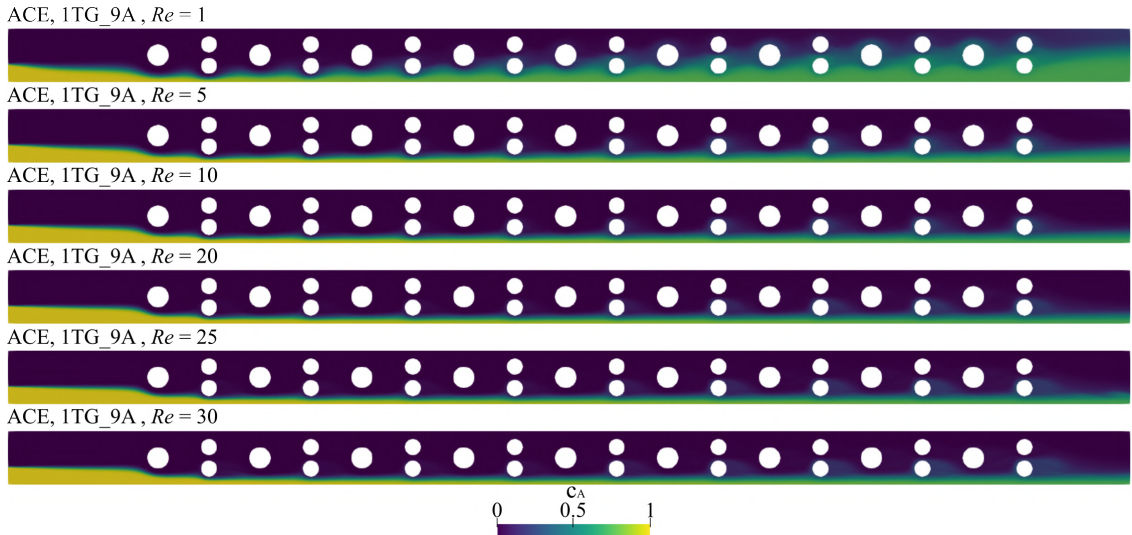
Figure 4.44: Alcohol contour for different Reynolds numbers in ACE with the molar ratio 1TG to 9A.

ACE, 1TG_12A , $Re = 1$

ACE, 1TG_12A , $Re = 5$

ACE, 1TG_12A , $Re = 10$

ACE, 1TG_12A , $Re = 20$

ACE, 1TG_12A , $Re = 25$

ACE, 1TG_12A , $Re = 30$

c_A

0   0,5   1
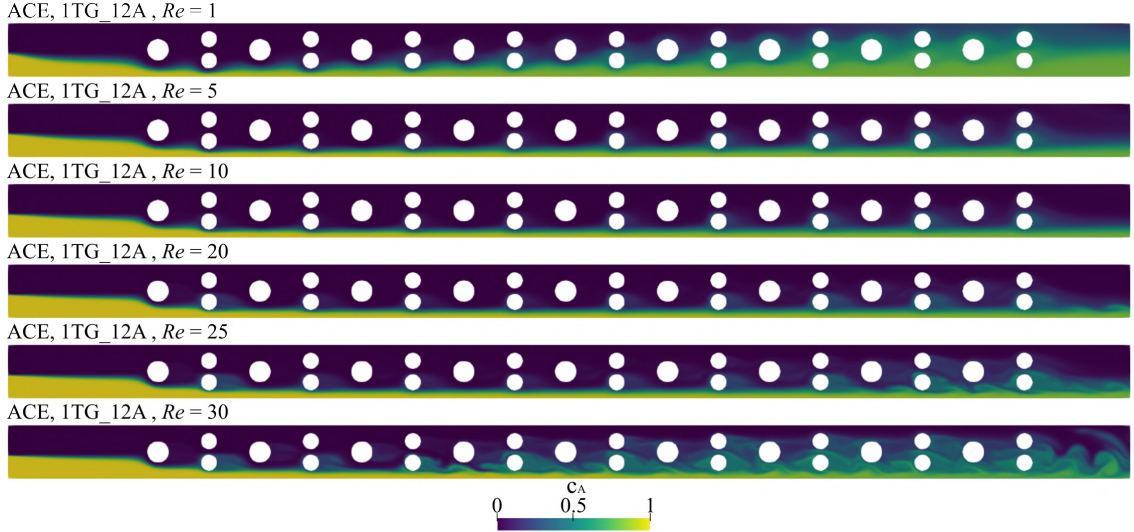
Figure 4.45: Alcohol contour for different Reynolds numbers in ACE with the molar ratio 1TG to 12A.

The ACE geometry was expected to promote greater cross-stream transport due to their staggered arrangement, and indeed, the velocity fields revealed a more significant disruption of the flow compared to the aligned configuration. Nonetheless, the mixing index results, as shown in Figure 4.46, demonstrated that the enhancement remained comparable to the MCE case, with both geometries exhibiting similar axial evolution of MI. This outcome indicated that although the staggered configuration induced additional flow asymmetry, it did not translate into a substantial quantitative advantage in terms of overall mixing efficiency.
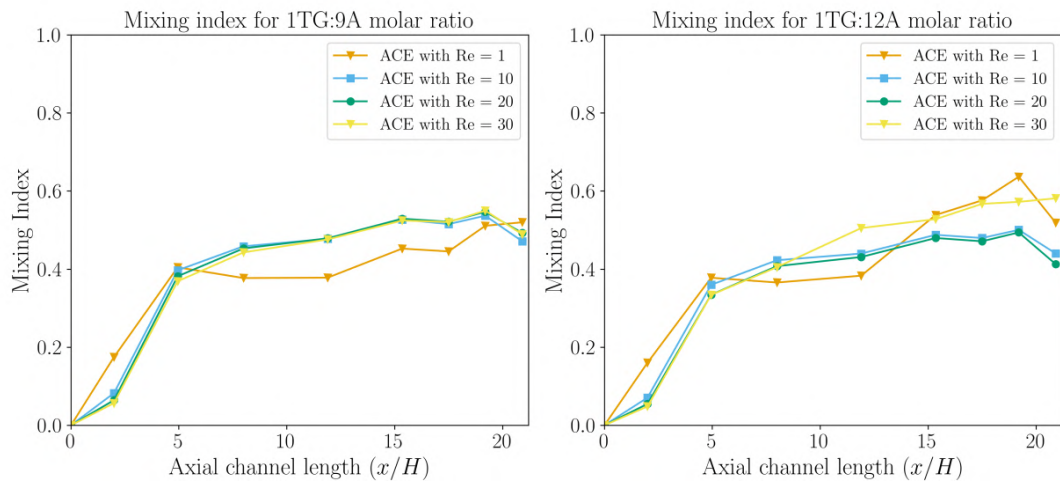
Figure 4.46: Mixing index as a function of axial ACE channel length for different Reynolds numbers and molar ratios.

77

Rectangular Obstructions

The microreactor with rectangular obstructions is illustrated in Figure 4.47, where the sharp-edged blocks are resolved by the triangular unstructured mesh.
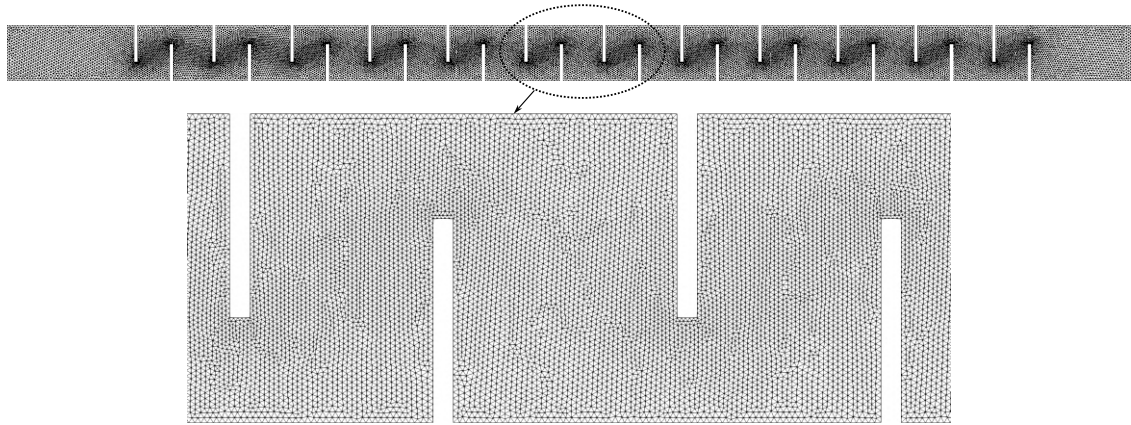
Figure 4.47: Unstructured mesh with triangular elements of the microchannel with rectangular obstructions (MSE).

The alcohol contours for different meshes (Figure 4.48) demonstrated that convergence was achieved for intermediate to fine grids, with an apparent recirculation zone for all meshes after the last static element of obstruction.
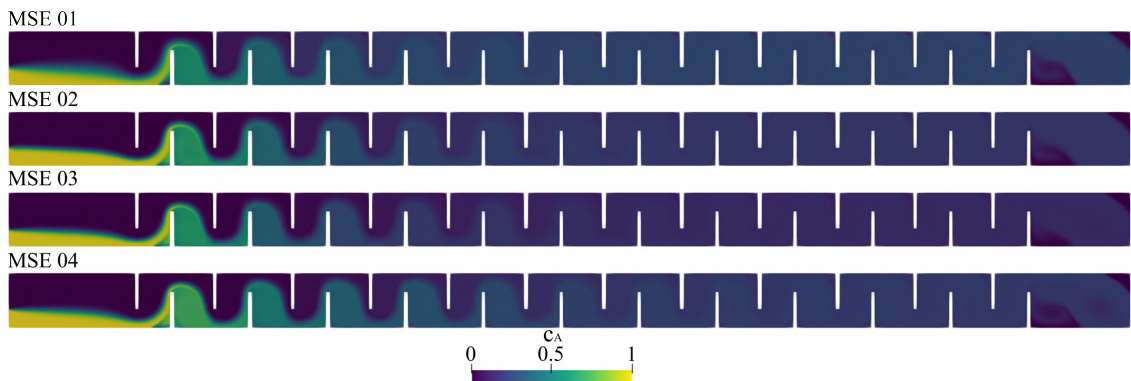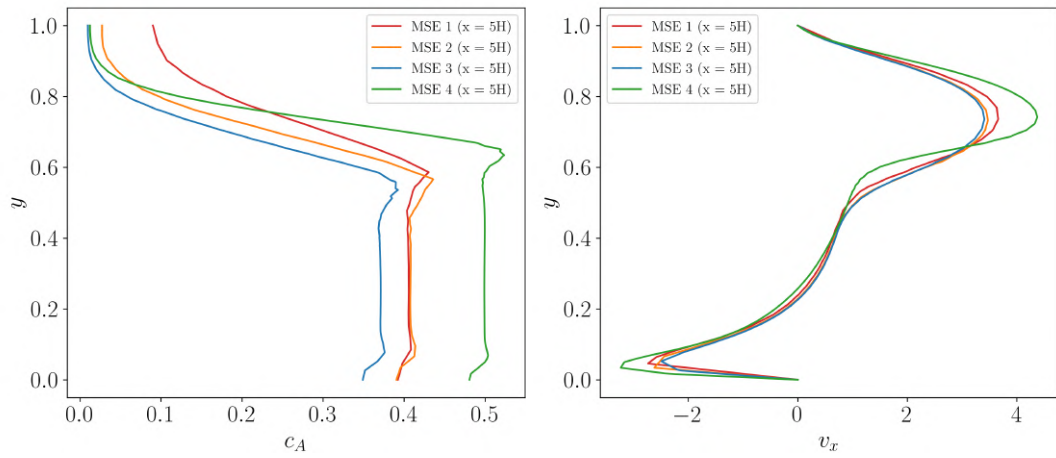
Figure 4.48: Alcohol contour for different meshes in MSE.

The computational requirements listed in Table 4.10 indicated simulation times from 10.05 hours for MSE 01 to 33.47 hours for MSE 04 at $Re = 10$. The geometry proved less expensive computationally than ACE, but refinement remained essential for capturing recirculation behind the obstructions.
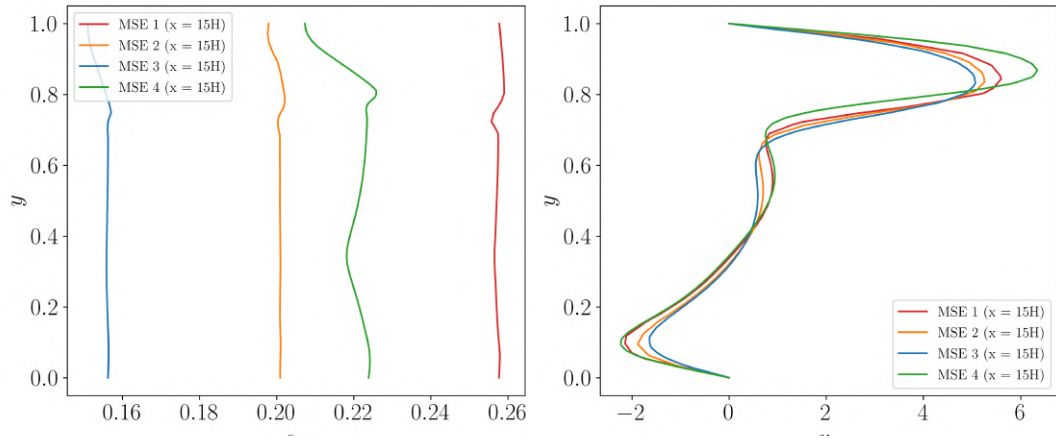
Table 4.10: Rectangular Obstructions Microreactor mesh statistics and computational time for $Re = 10$.

Mesh	Nodes	Elements	CPU time (h)	Time step [-]
MSE 01	21073	40186	10.05	0.01
MSE 02	27746	53224	13.17	0.01
MSE 03	38932	75042	18.27	0.01
MSE 04	77473	150870	33.47	0.01
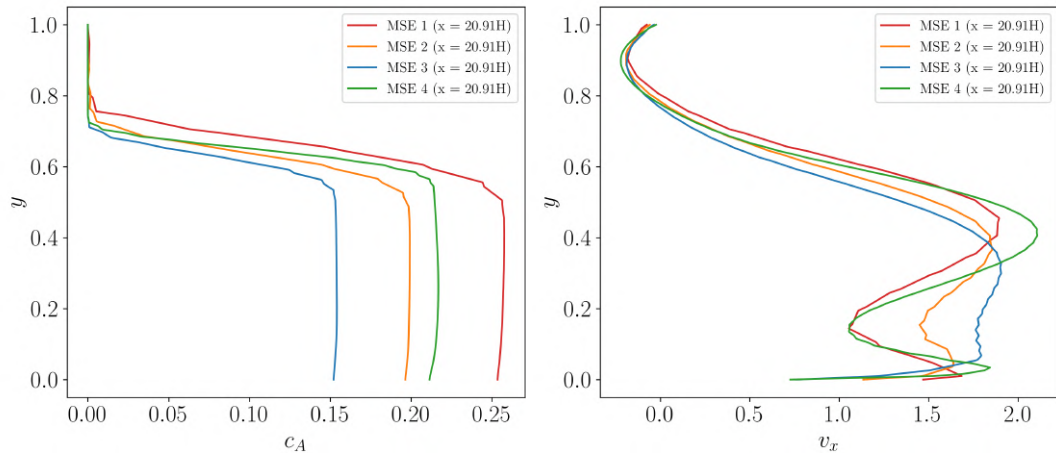
The axial profiles of alcohol concentration and velocity at $X = 5H$, $X = 15H$, and $X = 20.91H$ for $Re = 10$ are presented in Figure 4.49. At $X = 5H$, the presence of rectangular blocks immediately disturbs the flow, generating strong recirculation zones at the corners. These recirculations trap part of the fluid and enhance local mixing. At $X = 15H$, alcohol concentration profiles show substantial penetration into the triglyceride-rich region, while velocity contours reveal low-speed pockets behind the blocks that act as reservoirs of recirculated fluid. By $X = 20.91H$, the concentration is more homogenized compared to the straight channel but still less uniform than in the ACE case, due to the larger stagnant regions formed behind the rectangular obstructions.

(a) c_A and v_x profile for $Re_{TG} = 10$ at $X = 5H$.

(b) c_A and v_x profile for $Re_{TG} = 10$ at $X = 15H$.

(c) c_A and v_x profile for $Re_{TG} = 10$ at $X = 20.91H$.

Figure 4.49: MSE v_x and c_A profiles at various X positions along the microreactor for $Re = 10$.

Streamline distributions at varying Reynolds numbers (Figure 4.50) illustrate

the distinctive mixing mechanism of rectangular blocks. At $Re = 1$, the flow closely follows the block walls, with only weak recirculations. As Re increases, the wakes grow stronger and contribute to cross-stream mixing, although stagnation behind the blocks limits efficiency.
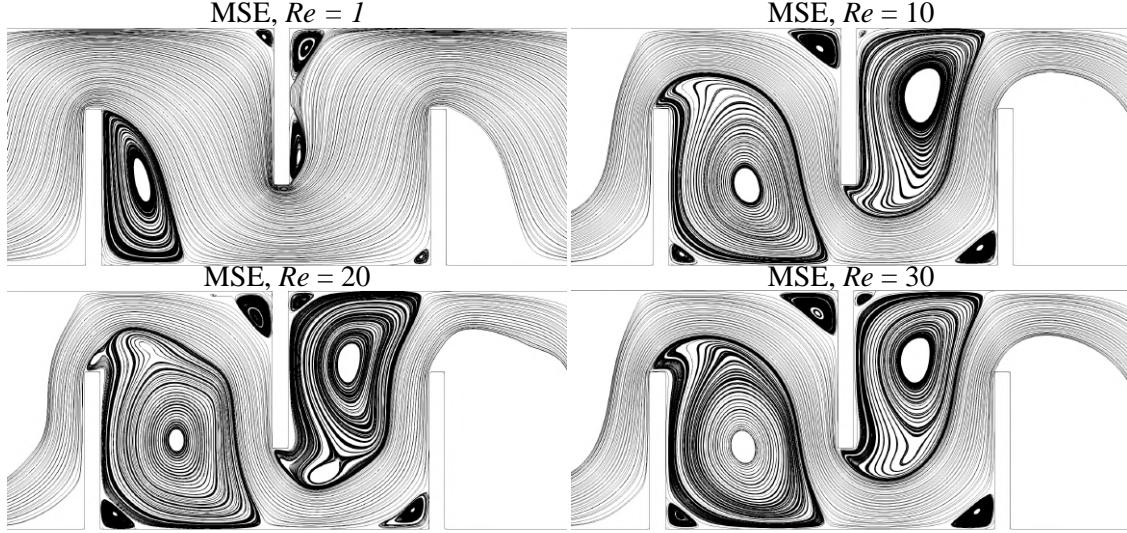
Figure 4.50: Streamlines of MSE for Reynolds number of 1, 10, 20 and 30.

The alcohol concentration contours (Figures 4.51 and 4.52) show that higher Reynolds numbers increase alcohol penetration, but the large recirculation zones delay full homogenization compared to ACE.
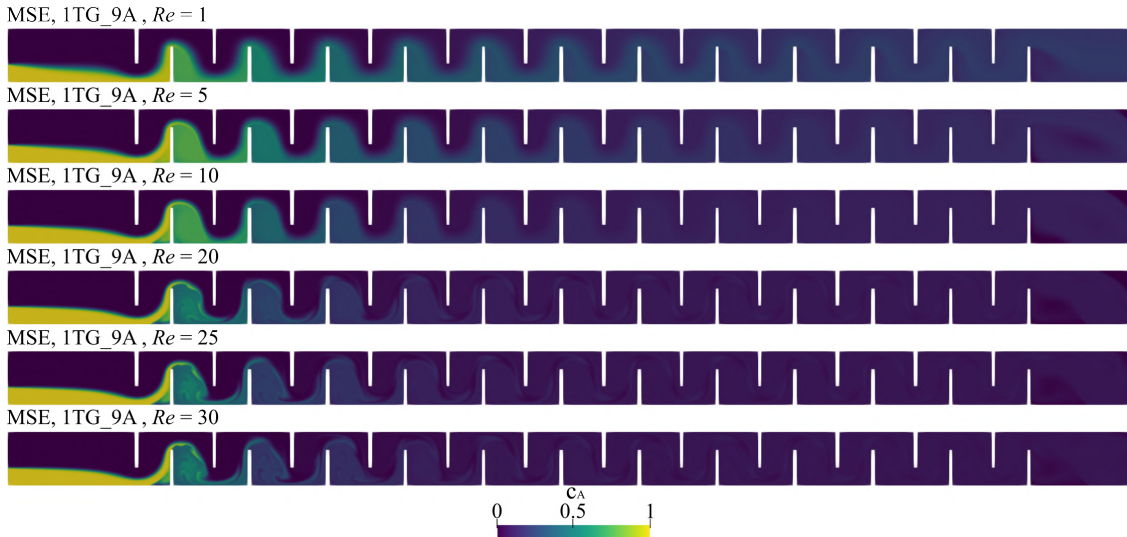
Figure 4.51: Alcohol contour for different Reynolds numbers in MSE with the molar ratio 1TG to 9A.

MSE, 1TG_12A , $Re = 1$

MSE, 1TG_12A , $Re = 5$

MSE, 1TG_12A , $Re = 10$

MSE, 1TG_12A , $Re = 20$

MSE, 1TG_12A , $Re = 25$

MSE, 1TG_12A , $Re = 30$

c_A

0   0,5   1
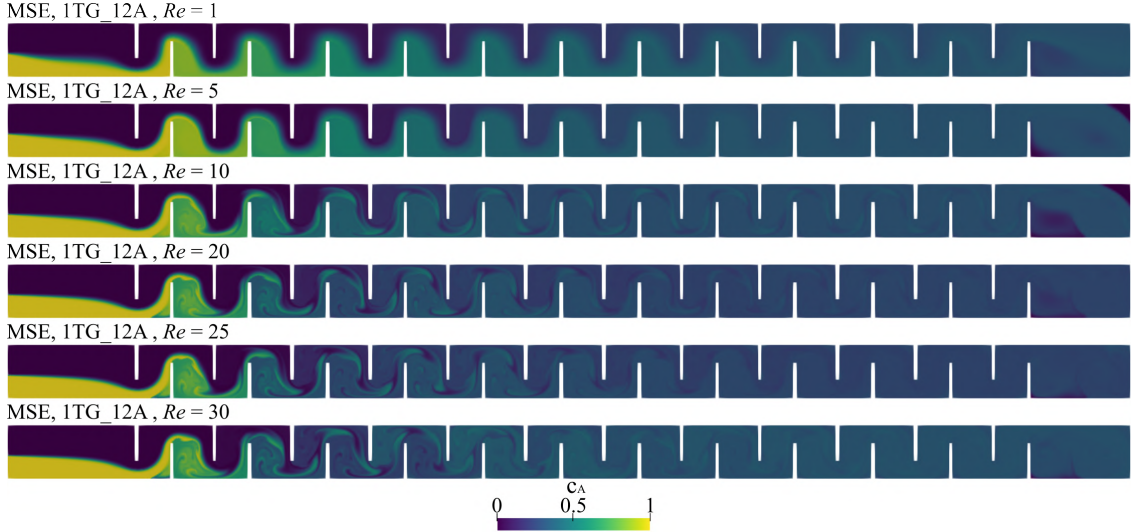
Figure 4.52: Alcohol contour for different Reynolds numbers in MSE with the molar ratio 1TG to 12A.

The rectangular obstruction geometry showed the most promising results in terms of mixing efficiency. The large recirculation zones generated behind the rectangular blocks facilitated intense fluid stretching and folding, accelerating homogenization along the channel. This behavior was clearly reflected in the mixing index (Figure 4.53), which reached the highest values among all tested configurations, outperforming both circular-based designs. Although some localized stagnant regions were identified, their negative impact was outweighed by the strong advective contribution of the recirculating structures. Consequently, this geometry emerged as the most efficient for promoting mixing in miscible displacement flows under the studied conditions.
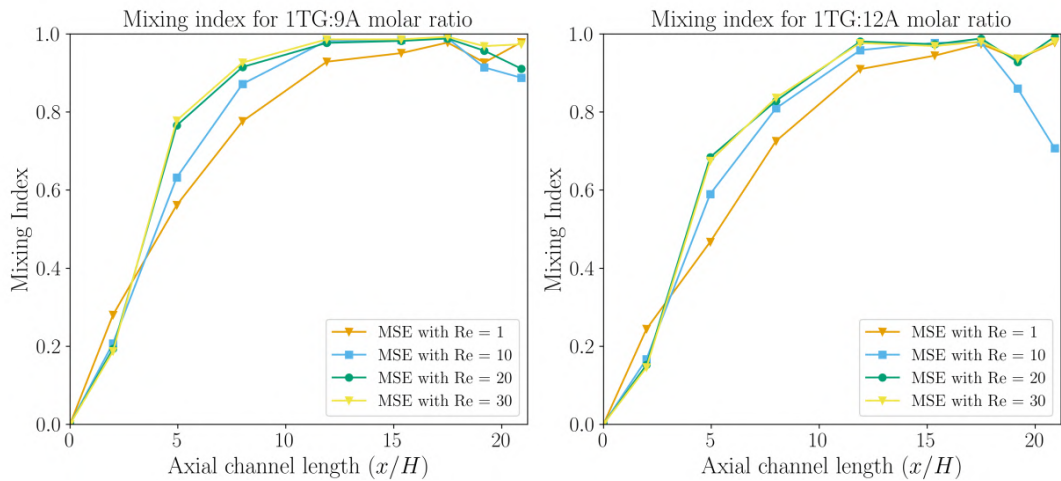
Figure 4.53: Mixing index as a function of axial MSE channel length for different Reynolds numbers and molar ratios.

Triangular Baffles with Circular Obstructions

The most complex configuration studied combines triangular baffles with circular obstructions, as shown in Figure 4.54. The unstructured triangular mesh resolves both the sharp baffle edges and the curved surfaces of the circular obstacles with high fidelity.
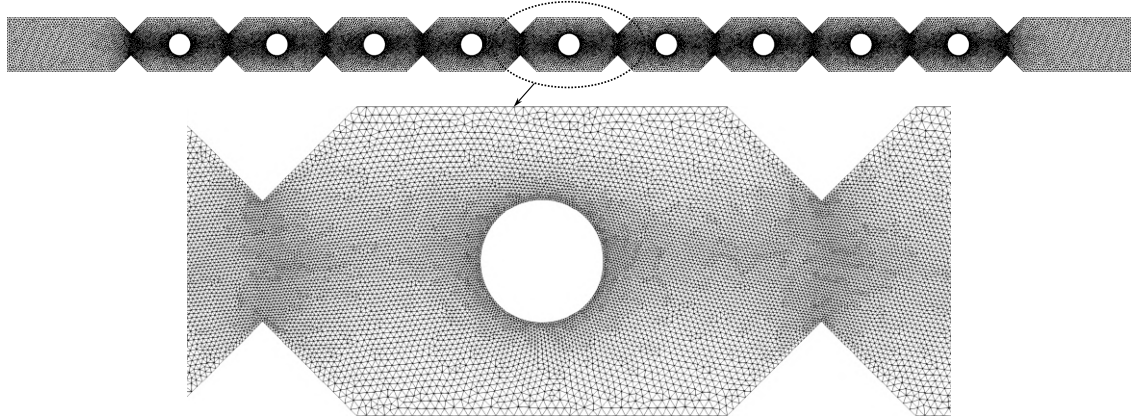
Figure 4.54: Unstructured mesh with triangular elements of the microchannel with triangular baffles and circular obstructions (SR).

The mesh sensitivity analysis (Figure 4.55) demonstrates that the alcohol distribution converges satisfactorily with mesh refinement, while Table 4.11 highlights the high computational demand of this geometry, reaching up to 36.37 h for SR 04 at $Re = 10$. The combined complexity of obstacles significantly increases the resolution requirements.
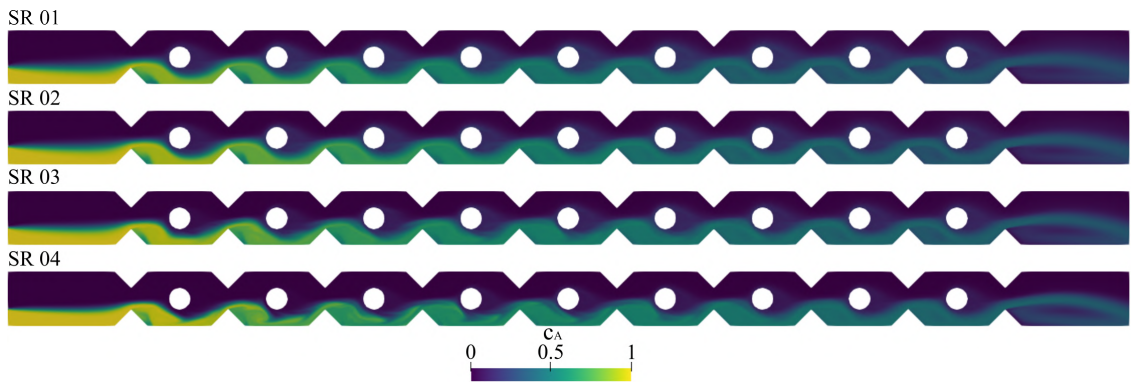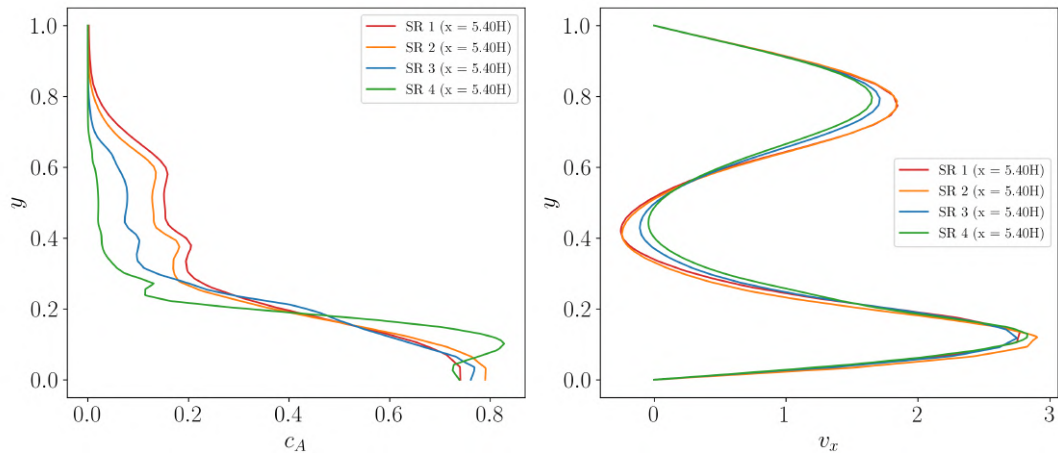
Figure 4.55: Alcohol contour for different meshes in SR.
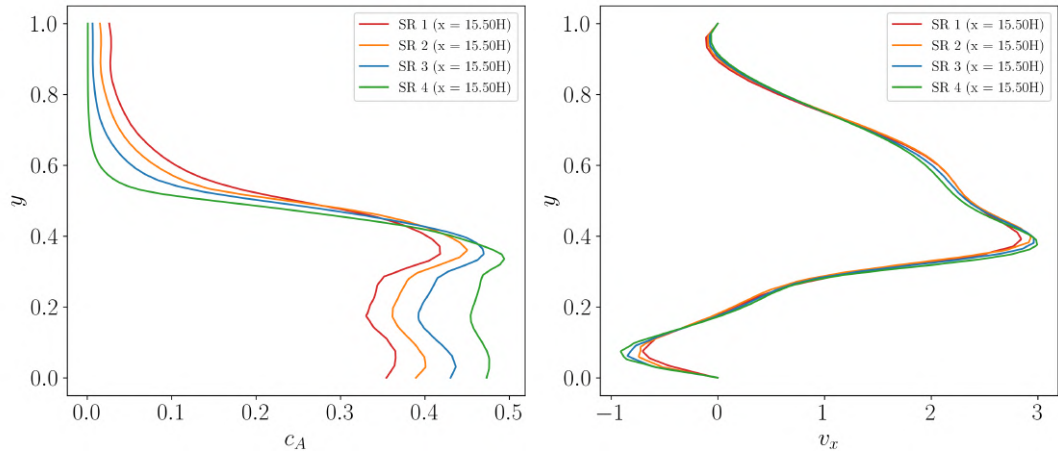
Table 4.11: Triangular Baffles with Circular Obstructions Microreactor mesh statistics and computational time for $Re = 10$.

Mesh	Nodes	Elements	CPU time (h)	Time step [-]
SR 01	27207	52478	12.25	0.01
SR 02	33759	65344	15.50	0.01
SR 03	43737	84982	20.17	0.01
SR 04	82086	160652	36.37	0.01
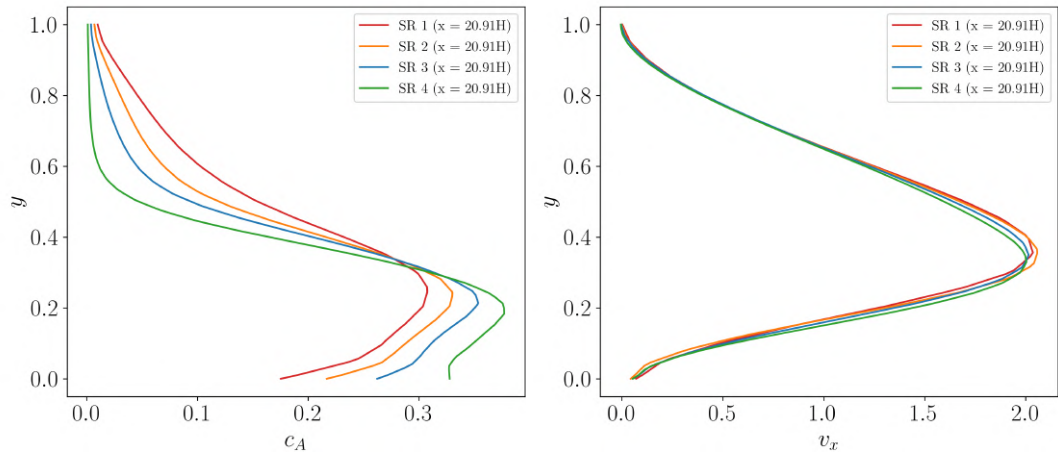
The profiles of alcohol concentration and velocity at $X = 5H$, $X = 15H$, and $X = 20.91H$ for $Re = 10$ are presented in Figure 4.56. At $X = 5H$, the triangular baffles already redirect the alcohol stream toward the channel center, enhancing transversal penetration. At $X = 15H$, the combined effect of baffles and circular obstructions generates alternating shear layers and recirculation zones, leading to highly nonuniform velocity distributions. The alcohol concentration shows strong lateral spreading at this stage. By $X = 20.91H$, the mixture is more homogenized than in all previous geometries, highlighting the effectiveness of combining sharp deflectors with circular obstacles in promoting mixing.

(a) c_A and v_x profile for $Re_{TG} = 10$ at $X = 5H$.

(b) c_A and v_x profile for $Re_{TG} = 10$ at $X = 15H$.

(c) c_A and v_x profile for $Re_{TG} = 10$ at $X = 20.91H$.

Figure 4.56: SR v_x and c_A profiles at various X positions along the microreactor for $Re = 10$.

The streamline plots for different Reynolds numbers (Figure 4.57) further reveal

the aggressive mixing enhancement of the SR geometry. Even at $Re = 1$, the baffles and obstacles deflect the streamlines significantly, breaking flow symmetry and promoting lateral mixing. At higher Reynolds numbers, strong vortices and secondary flows develop, further improving transversal exchange.

SR, Re = 1

SR, Re = 10

SR, Re = 20

SR, Re = 30
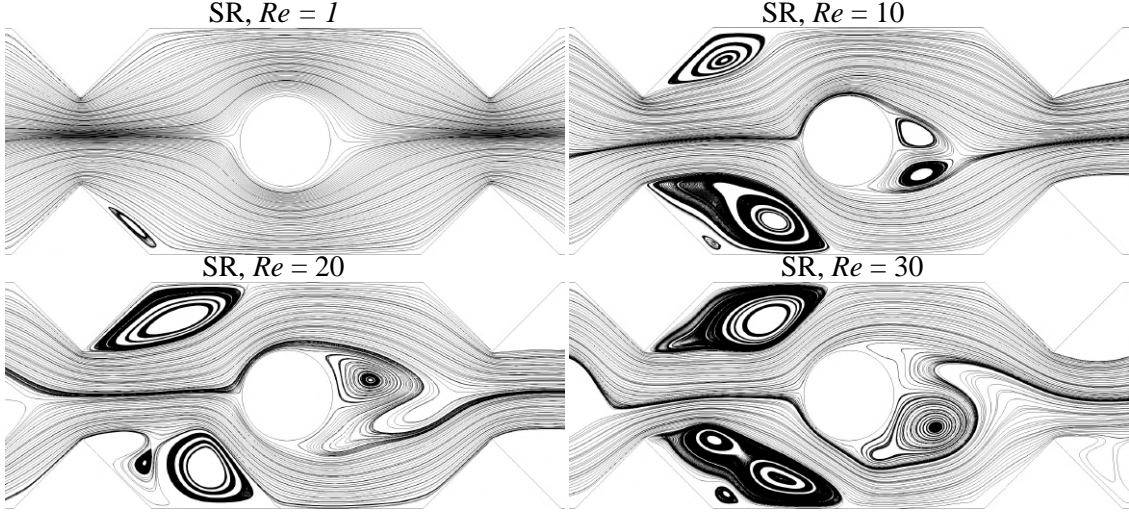
Figure 4.57: Streamlines of SR for Reynolds number of 1, 10, 20 and 30.

The alcohol concentration contours in Figures 4.58 and 4.59 confirm that homogenization occurs earlier and more effectively in SR than in any other geometry.

SR, 1TG_9A , Re = 1

SR, 1TG_9A , Re = 5

SR, 1TG_9A , Re = 10

SR, 1TG_9A , Re = 20

SR, 1TG_9A , Re = 25

SR, 1TG_9A , Re = 30

c_A

0   0,5   1
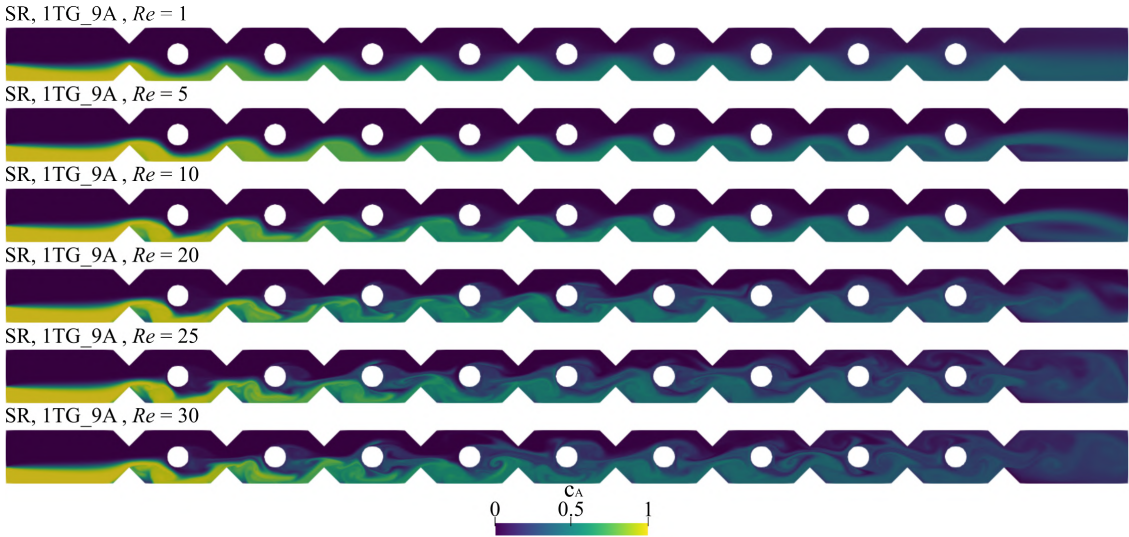
Figure 4.58: Alcohol contour for different Reynolds numbers in SR with the molar ratio 1TG to 9A.
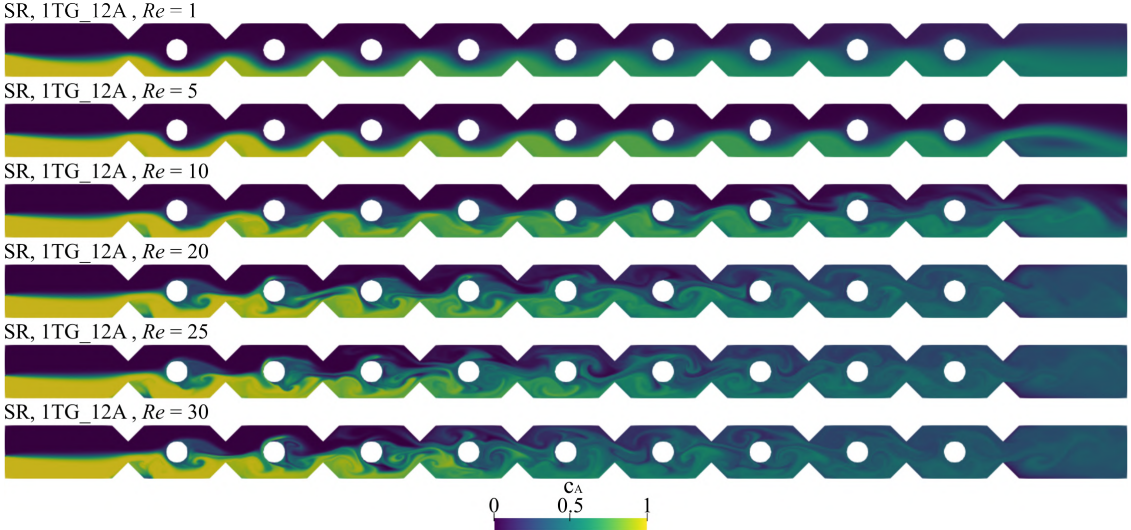
Figure 4.59: Alcohol contour for different Reynolds numbers in SR with the molar ratio 1TG to 12A.

The triangular baffles with circular obstructions produced complex flow structures with significant transversal exchange and secondary recirculation. Qualitatively, the velocity and concentration fields indicated enhanced advective transport when compared to the straight channel and circular-only configurations. However, despite these features, the mixing index results revealed that SR did not achieve the same level of performance as the rectangular obstructions. While still superior to SMC and competitive with the circular geometries, the SR design fell short of the efficiency achieved by MSE, suggesting that the addition of triangular baffles introduced flow disruption but did not maximize the homogenization process as effectively as the rectangular blocks.
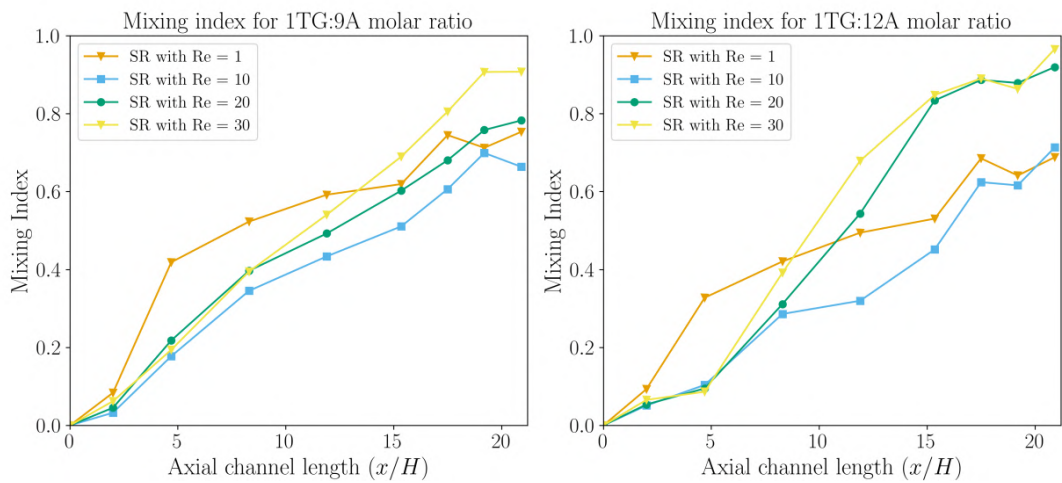
Figure 4.60: Mixing index as a function of axial SR channel length for different Reynolds numbers and molar ratios.

87

Performance Index

The comparative analysis of performance indices, mixing index and pressure drop presented in Tables 4.12, 4.13 and 4.14, respectively, underscores the trade-off between mixing intensity and energetic efficiency. The straight channel consistently achieved the highest PI values across all Reynolds numbers, with 0.359 at Reynolds 30 (1:9), despite having the lowest mixing index values. Conversely, obstacle-rich geometries such as SR and MSE generated much stronger mixing, as confirmed by Figures 4.52 and 4.59, but their PI values were 5–10 times smaller due to severe hydrodynamic penalties. Increasing the inlet molar ratio from 1:9 to 1:12 produced only marginal gains in MI and PI, indicating that stoichiometric excess of alcohol had a limited effect compared to geometric factors. The results therefore reveal a fundamental design trade-off: maximizing mixing requires obstacles, but maximizing performance index favors the unobstructed straight channel.

Table 4.12: Effects of channel geometry and molar ratio on Performance Index for all Reynolds numbers (values multiplied by 10^3).

Geometry	Molar Ratio	Performance Index ($PI \times 10^3$)			
		Reynolds Number			
		1	10	20	30
SMC	1 : 9	47.30	213.00	301.00	359.00
MCE	1 : 9	4.29	25.20	42.00	56.30
ACE	1 : 9	2.17	9.57	15.30	18.50
MSE	1 : 9	3.04	3.49	3.23	3.29
SR	1 : 9	6.01	18.90	27.10	31.80
SMC	1 : 12	50.50	209.00	280.00	329.00
MCE	1 : 12	4.97	23.80	39.60	52.70
ACE	1 : 12	2.73	10.00	14.20	27.70
MSE	1 : 12	3.58	2.60	3.47	3.43
SR	1 : 12	6.85	22.40	33.50	36.20

Table 4.13: Effects of channel geometry and molar ratio on Mixing Index for all Reynolds numbers.

Geometry	Molar Ratio	Mixing Index (MI)			
		Reynolds Number			
		1	10	20	30
SMC	1 : 9	0.72	0.51	0.45	0.42
MCE	1 : 9	0.57	0.50	0.52	0.54
ACE	1 : 9	0.52	0.47	0.49	0.49
MSE	1 : 9	0.98	0.89	0.91	0.97
SR	1 : 9	0.75	0.66	0.78	0.91
SMC	1 : 12	0.61	0.45	0.38	0.35
MCE	1 : 12	0.53	0.44	0.47	0.49
ACE	1 : 12	0.52	0.44	0.41	0.58
MSE	1 : 12	0.98	0.71	0.99	0.98
SR	1 : 12	0.69	0.71	0.92	0.97

Table 4.14: Effects of channel geometry and molar ratio on Pressure Drop for all Reynolds numbers.

Geometry	Molar Ratio	Pressure Drop (ΔP)			
		Reynolds Number			
		1	10	20	30
SMC	1 : 9	15.19	2.39	1.48	1.15
MCE	1 : 9	133.59	19.90	12.40	9.62
ACE	1 : 9	239.44	49.25	32.18	26.37
MSE	1 : 9	321.03	253.98	281.67	295.34
SR	1 : 9	125.22	35.03	28.81	28.46
SMC	1 : 12	12.13	2.15	1.37	1.07
MCE	1 : 12	106.22	18.20	11.77	9.21
ACE	1 : 12	189.84	43.71	29.03	20.95
MSE	1 : 12	272.62	271.54	285.24	285.17
SR	1 : 12	100.32	31.83	27.43	26.66

Chapter 5

Conclusion

In this dissertation, a numerical methodology was developed and applied to the study of miscible two-phase flows in microreactors with different geometrical configurations, aiming to evaluate the hydrodynamic behavior of such systems and to identify optimal conditions for biodiesel synthesis in compact and sustainable technologies. The governing equations of incompressible two-dimensional Navier–Stokes flows were coupled with the transport equation for the alcohol–triglyceride mixture, and simulations were carried out for different inlet molar ratios and Reynolds numbers representative of laminar microchannel conditions.

As an initial step, single-phase flow cases were simulated in order to validate the numerical implementation and assess the reliability of the methodology. The flow between parallel plates reproduced the classical parabolic velocity profile, providing an important verification of the finite element formulation and the numerical stability of the scheme. The lid-driven cavity flow offered a more demanding test of the methodology, highlighting the accuracy in capturing vortical structures while also revealing the impact of numerical diffusion at higher Reynolds numbers. These preliminary cases confirmed the robustness of the numerical strategy and established confidence for the subsequent two-phase miscible flow simulations.

The analysis of microreactor geometries for two-phase miscible flow began with the straight channel, which was adopted as a reference case. As expected, mixing was limited and occurred primarily through molecular diffusion, leading to strongly stratified concentration fields along the channel. However, the absence of obstacles minimized hydrodynamic losses, allowing this configuration to consistently achieve the highest performance index values among all geometries evaluated.

The introduction of obstacles altered the mixing behavior significantly. In the aligned circular obstruction geometry, recirculation zones formed downstream of each post, promoting local mixing but leaving unmixed regions near the walls. When the obstacles were staggered in an alternating arrangement, stronger transverse motion and chaotic advection emerged, increasing interfacial area and enhancing mixing

efficiency. Rectangular obstacles further intensified shear-layer instabilities, accelerating homogenization, but the associated hydrodynamic resistance drastically reduced energetic efficiency. Finally, the geometry combining triangular baffles with circular obstacles produced the most effective mixing, with rapid homogenization of the alcohol–triglyceride mixture occurring much earlier than in other designs. Despite this, the severe pressure penalties associated with the baffles meant that its overall efficiency, measured by the performance index, remained considerably lower than that of the straight channel.

Overall, the results demonstrated a clear trade-off between mixing enhancement and energetic efficiency. Obstacle-rich geometries (rectangular blocks and triangular baffles with circular obstacles) were highly effective in promoting mixing but suffered from significant pressure drops, which compromised their performance index. In contrast, the straight channel provided poor mixing but offered the best balance between simplicity, low hydrodynamic losses, and energetic efficiency. Increasing the inlet alcohol ratio from 1:9 to 1:12 produced only minor improvements in both mixing and performance, confirming that geometry had a much stronger influence on flow behavior than inlet stoichiometry.

In summary, this research highlighted the decisive role of geometry in controlling miscible displacement and mixing in microreactors. When the design goal is to maximize mixing intensity in short channel lengths, complex geometries with deflectors and obstacles are advantageous. However, if the priority is energy efficiency and constructive simplicity, the straight channel remains the most suitable configuration. Future work should focus on defining composite performance metrics that jointly account for mixing efficiency and hydrodynamic losses, extending the numerical methodology to three-dimensional models, and coupling the hydrodynamics with the full chemical kinetics of biodiesel transesterification. Experimental validation at the microscale will also be essential to establish reliable design criteria for sustainable biodiesel microreactors.

5.1 Future Work

A promising direction for future work is the introduction of optimization frameworks such as adjoint methods or evolutionary algorithms could further guide the design of microreactors by systematically exploring geometry variations beyond canonical shapes. This would open pathways for discovering novel geometrical configurations that balance mixing efficiency and pressure drop more effectively than traditional obstacle-based layouts.

Another avenue for improvement lies in the implementation of higher-order advection schemes or flux-correction techniques. The results of this study revealed the

influence of numerical diffusion, particularly in high–Reynolds number flows, which can artificially smear concentration gradients and underestimate mixing intensity. Advanced discretization strategies, such as discontinuous Galerkin formulations, total variation diminishing (TVD) methods, or flux-corrected transport algorithms, could significantly reduce this error, leading to more accurate predictions of concentration fields and interfacial dynamics.

The extension of simulations to three-dimensional geometries is also an essential step forward. While the present two-dimensional framework captured the fundamental mixing mechanisms, it cannot account for secondary flows, spanwise vortices, or out-of-plane circulation, all of which are expected to play an important role in practical microreactors. A full three-dimensional description would provide a more realistic representation of the hydrodynamics and enable the evaluation of geometrical features, such as channel depth and cross-sectional aspect ratios, that were not considered in the current study.

Equally important is the coupling of hydrodynamic mixing fields with the chemical kinetics of biodiesel transesterification. In this work, only the transport of triglycerides and alcohol was considered, but the inclusion of the full reaction pathway involving intermediate species (diglycerides, monoglycerides, glycerol, and methyl esters) would allow direct prediction of chemical yield. This integration would bridge the gap between fluid mechanics and reaction engineering, enabling a more complete evaluation of microreactor performance in terms of product formation rather than purely hydrodynamic measures.

Finally, experimental validation should be pursued to benchmark the numerical predictions and establish confidence in the methodology. Techniques such as micro-Particle Image Velocimetry (micro-PIV) could be used to measure velocity fields, while planar laser-induced fluorescence (PLIF) or other tracer-based methods could provide concentration maps of miscible streams. Such comparisons would not only validate the numerical results but also help calibrate model parameters, quantify uncertainties, and identify limitations in the simulations. Coupling numerical and experimental efforts will be fundamental to advancing the design of optimized microreactors for biodiesel synthesis.

References

[1] ZHAO, Y., CHEN, G., YUAN, Q. "Liquid-liquid two-phase flow patterns in a rectangular microchannel", *AIChE Journal*, v. 52, n. 12, pp. 4052–4060, 2006.

[2] SANTANA, H. S., JÚNIOR, J. L., TARANTO, O. P. "Numerical simulations of biodiesel synthesis in microchannels with circular obstructions", *Chemical Engineering and Processing: Process Intensification*, v. 98, pp. 137–146, 2015.

[3] BISWAS, G., BREUER, M., DURST, F. "Backward-Facing Step Flows for Various Expansion Ratios at Low and Moderate Reynolds Numbers", *Journal of Fluids Engineering*, v. 126, n. 3, pp. 362–374, 2004. ISSN: 0098-2202. doi: 10.1115/1.1760532.

[4] GOYAL, N., MEIBURG, E. "Miscible displacements in Hele-Shaw cells: two-dimensional base states and their linear stability", *Journal of Fluid Mechanics*, v. 558, pp. 329–355, 2006. doi: 10.1017/S0022112006009992.

[5] BRIAN H. DENNIS, WEIYA JIN, J. C., TIMMONS, R. B. "Inverse determination of kinetic rate constants for transesterification of vegetable oils", *Inverse Problems in Science and Engineering*, v. 16, n. 6, pp. 693–704, 2008.

[6] SUN, P., WANG, B., YAO, J., et al. "Fast Synthesis of Biodiesel at High Throughput in Microstructured Reactors", *Industrial & Engineering Chemistry Research*, v. 49, n. 3, pp. 1259–1264, 2010.

[7] LEUNG, D. Y., WU, X., LEUNG, M. "A review on biodiesel production using catalyzed transesterification", *Applied Energy*, v. 87, n. 4, pp. 1083–1095, 2010.

[8] DEMIRBAS, A. "Comparison of transesterification methods for production of biodiesel from vegetable oils and fats", *Energy Conversion and Management*, v. 49, n. 1, pp. 125–130, 2008.

[9] CHAROENWAT, R. *Experimental And Numerical Investigation Of Transesterification Of Vegetable Oil With A Continuous Flow Capillary Reactor.* Thesis, The University of Texas at Arlington, Arlington, Texas, USA, 2011.

[10] BART, J. C., PALMERI, N., CAVALLARO, S. *Biodiesel Science and Technology.* 1st edition ed. Sawston, Woodhead Publishing, 2010.

[11] AL-DHUBABIAN, A. A. *Production of biodiesel from soybean oil in a micro scale reactor.* Tese de Mestrado, Oregon State University, Oregon, USA, 2005.

[12] CAI, Z.-Z., WANG, Y., TENG, Y.-L., et al. "A two-step biodiesel production process from waste cooking oil via recycling crude glycerol esterification catalyzed by alkali catalyst", *Fuel Processing Technology*, v. 137, pp. 186–193, 2015.

[13] HESSEL, V., LÖWE, H. "Organic Synthesis with Microstructured Reactors", *Chemical Engineering & Technology*, v. 28, pp. 267–284, 2005.

[14] KOBAYASHI, J., MORI, Y., KOBAYASHI, S. "Multiphase Organic Synthesis in Microchannel Reactors", *Chemistry – An Asian Journal*, v. 1, n. 1-2, pp. 22–35, 2006.

[15] LEE, C.-Y., WANG, W.-T., LIU, C.-C., et al. "Passive mixers in microfluidic systems: A review", *Chemical Engineering Journal*, v. 288, pp. 146–160, 2016.

[16] COSTA JUNIOR, J. M., NAVEIRA-COTTA, C. P., DE MORAES, D. B., et al. "Innovative Metallic Microfluidic Device for Intensified Biodiesel Production", *Industrial & Engineering Chemistry Research*, v. 59, pp. 389–398, 2020.

[17] WILLIAMSON, C. H. K. "Vortex Dynamics in the Cylinder Wake", *Annual Review of Fluid Mechanics*, v. 28, pp. 477–539, 1996.

[18] CHEN, L., WANG, G., LIM, C., et al. "Evaluation of passive mixing behaviors in a pillar obstruction poly(dimethylsiloxane) microfluidic mixer using fluorescence microscopy", *Microfluidics and Nanofluidics*, v. 7, pp. 267–273, 2008.

[19] ZHANG, S., CAGNEY, N., BALABANI, S., et al. "Probing vortex-shedding at high frequencies in flows past confined microfluidic cylinders using high-

speed microscale particle image velocimetry", *Physics of Fluids*, v. 31, pp. 102001, 2019.

[20] NGUYEN, N.-T., WU, Z. "Characterization of mixing in an optimized designed T–T mixer with cylindrical elements", *Journal of Micromechanics and Microengineering*, v. 15, pp. R1, 2004.

[21] JUNIOR, J. M. C. *Análise Teórico–Experimental de Microrreatores para Síntese de Biodiesel com Recuperação de Calor Rejeitado*. Tese de D.Sc., Universidade Federal do Rio de Janeiro, Rio de Janeiro, RJ, Brazil, 2017.

[22] XIE, T., ZHANG, L., XU, N. "Biodiesel synthesis in microreactors", *Green Processing and Synthesis*, v. 1, n. 1, pp. 61–70, 2012.

[23] MEHER, L., VIDYA SAGAR, D., NAIK, S. "Technical aspects of biodiesel production by transesterification—a review", *Renewable and Sustainable Energy Reviews*, v. 10, n. 3, pp. 248–268, 2006.

[24] SARMA, H., JOSHI, S. J., PRASAD, R., et al. "Correction to: Biobased Nanotechnology for Green Applications". In: *Biobased Nanotechnology for Green Applications*, 2 ed., cap. 7, New York, USA, Springer International Publishing, 2021.

[25] MEHEJABIN, F., MUSHARRAT, A., AHMED, S. F., et al. "Sustainable Biofuel Production Utilizing Nanotechnology: Challenges and Potential Solutions", *GCB Bioenergy*, v. 16, n. 10, pp. e70001, 2024.

[26] BHARATHIRAJA, B., SELVAKUMARI, I. A. E., KUMAR, R. P. "Chapter 39 - Future prospects, opportunities, and challenges in the application of nanomaterials in biofuel production systems". In: *Nanomaterials*, v. 122, Academic Press, pp. 797–806, Chennai, India, 2021.

[27] PATTANAIK, L., PATTNAIK, F., SAXENA, D. K., et al. "Chapter 5 - Biofuels from agricultural wastes". In: *Second and Third Generation of Feedstocks*, v. 122, Elsevier, pp. 103–142, New Delhi, India, 2019.

[28] MOHAMMADSHIRAZI, A., AKRAM, A., RAFIEE, S., et al. "Energy and cost analyses of biodiesel production from waste cooking oil", *Renewable and Sustainable Energy Reviews*, v. 33, pp. 44–49, 2014.

[29] SEKOAI, P. T., OUMA, C. N. M., DU PREEZ, S. P., et al. "Application of nanoparticles in biofuels: An overview", *Fuel*, v. 237, pp. 380–397, 2019.

[30] WANG, H., ZHANG, B., GONG, S., et al. "Experimental and modeling studies of exo-tetrahydrobicyclopentadiene and tetrahydrotricyclopentadiene pyrolysis at 1 and 30 atm", *Combustion and Flame*, v. 232, pp. 111536, 2021.

[31] LAESECKE, J., ELLIS, N., KIRCHEN, P. "Production, analysis and combustion characterization of biomass fast pyrolysis oil – Biodiesel blends for use in diesel engines", *Fuel*, v. 199, pp. 346–357, 2017.

[32] BALOCH, H. A., NIZAMUDDIN, S., SIDDIQUI, M., et al. "Recent advances in production and upgrading of bio-oil from biomass: A critical overview", *Journal of Environmental Chemical Engineering*, v. 6, n. 4, pp. 5101–5118, 2018.

[33] KANNAN, G., ANAND, R. "Experimental investigation on diesel engine with diestrol–water micro emulsions", *Energy*, v. 36, n. 3, pp. 1680–1687, 2011.

[34] AGARWAL, A. K. "Biofuels (alcohols and biodiesel) applications as fuels for internal combustion engines", *Progress in Energy and Combustion Science*, v. 33, n. 3, pp. 233–271, 2007.

[35] MARTÍNEZ ARIAS, E. L., FAZZIO MARTINS, P., JARDINI MUNHOZ, A. L., et al. "Continuous Synthesis and in Situ Monitoring of Biodiesel Production in Different Microfluidic Devices", *Industrial & Engineering Chemistry Research*, v. 51, n. 33, pp. 10755–10767, 2012.

[36] SHELARE, S. D., BELKHODE, P. N., NIKAM, K. C., et al. "Biofuels for a sustainable future: Examining the role of nano-additives, economics, policy, internet of things, artificial intelligence and machine learning technology in biodiesel production", *Energy*, v. 282, pp. 128874, 2023.

[37] KUMAR, D., KUMAR, G., POONAM, et al. "Fast, easy ethanolysis of coconut oil for biodiesel production assisted by ultrasonication", *Ultrasonics Sonochemistry*, v. 17, n. 3, pp. 555–559, 2010.

[38] RICHARD, R., THIEBAUD-ROUX, S., PRAT, L. "Modelling the kinetics of transesterification reaction of sunflower oil with ethanol in microreactors", *Chemical Engineering Science*, v. 87, pp. 258–269, 2013.

[39] SCHWARZ, S., BOROVINSKAYA, E. S., RESCHETILOWSKI, W. "Base catalyzed ethanolysis of soybean oil in microreactors: Experiments and kinetic modeling", *Chemical Engineering Science*, v. 104, pp. 610–618, 2013.

[40] FREEDMAN, B., PRYDE, E., MOUNTS, T. "Variables affecting the yields of fatty esters from transesterified vegetable oils", *Journal of the American Oil Chemists Society*, v. 61, n. 10, pp. 1638–1643, 1984. doi: 10.1007/BF02541649.

[41] MARJANOVIĆ, A. V., STAMENKOVIĆ, O. S., TODOROVIĆ, Z. B., et al. "Kinetics of the base-catalyzed sunflower oil ethanolysis", *Fuel*, v. 89, pp. 665–671, 2010. doi: https://doi.org/10.1016/j.fuel.2009.09.025.

[42] ZANFIR, M. "5 - Portable and small-scale stationary hydrogen production from micro-reactor systems". In: *Advances in Hydrogen Production, Storage and Distribution*, Woodhead Publishing, pp. 123–155, https://doi.org/10.1533/9780857097736.1.123, 2014.

[43] GOPI, R., THANGARASU, V., VINAYAKASELVI M, A., et al. "A critical review of recent advancements in continuous flow reactors and prominent integrated microreactors for biodiesel production", *Renewable and Sustainable Energy Reviews*, v. 154, pp. 111869, 2022.

[44] MOHD LAZIZ, A., KUSHAARI, K., AZEEM, B., et al. "Rapid production of biodiesel in a microchannel reactor at room temperature by enhancement of mixing behaviour in methanol phase using volume of fluid model", *Chemical Engineering Science*, v. 219, pp. 115532, 2020.

[45] GUAN, G., KUSAKABE, K., MORIYAMA, K., et al. "Transesterification of Sunflower Oil with Methanol in a Microtube Reactor", *Industrial & Engineering Chemistry Research*, v. 48, n. 3, pp. 1357–1363, 2009.

[46] GUAN, G., TESHIMA, M., SATO, C., et al. "Two-phase flow behavior in microtube reactors during biodiesel production from waste cooking oil", *AIChE Journal*, v. 56, n. 5, pp. 1383–1390, 2010.

[47] ABDULLA YUSUF, H., ABDULLA, A. F., RADHI, F. A., et al. "Optimization of biodiesel production in a high throughput branched microreactor", *Energy Nexus*, v. 13, pp. 100276, 2024.

[48] AGHEL, B., BIABANI, A. "Using solar microreactors and photocatalysts to synthesize biodiesel", *Renewable Energy*, v. 220, pp. 119654, 2024.

[49] SILVA, J. L., CELESTINO, M. S., TARANTO, O. P., et al. "Smart scale-up of micromixers for efficient continuous biodiesel synthesis: A numerical study for process intensification", *Chemical Engineering and Processing - Process Intensification*, v. 196, pp. 109664, 2024.

[50] TAJIK GHANBARI, T., RAHIMI, M., RANJBAR, A. A., et al. "Mixing performance improvement of T-shaped micromixer using novel structural design of channel and obstacles", *Physics of Fluids*, v. 35, n. 12, pp. 122013, 12 2023.

[51] ÖZKAN, A., ERDEM, E. Y. "Numerical analysis of mixing performance in sinusoidal microchannels based on particle motion in droplets", *Microfluidics and Nanofluidics*, v. 19, n. 5, 2015.

[52] WU, Z., CAO, Z., SUNDEN, B. "Flow patterns and slug scaling of liquid-liquid flow in square microchannels", *International Journal of Multiphase Flow*, v. 112, pp. 27–39, 2019.

[53] WIDIANTO, A. Y., LORENZA, V., CLARISA, C., et al. "Mass transfer phenomena of partially miscible liquids under liquid-liquid slug flow in a circular microchannel", *Chemical Engineering Research and Design*, v. 205, pp. 57–66, 2024.

[54] CHEN, K., NAVEIRA-COTTA, C. P. "Theoretical Analyses of the Flow Patterns in the Biodiesel Production". In: *Proceedings of the 23rd ABCM International Congress of Mechanical Engineering*, pp. 237–253, Rio de Janeiro, dez. 2015.

[55] UNVERDI, S. O., TRYGGVASON, G. "A front-tracking method for viscous, incompressible, multi-fluid flows", *Journal of Computational Physics*, v. 100, n. 1, pp. 25–37, 1992. ISSN: 0021-9991. doi: 10.1016/0021-9991(92) 90307-K. Disponível em: <https://www.sciencedirect.com/science/article/pii/002199919290307K>.

[56] HIRT, C., NICHOLS, B. "Volume of fluid (VOF) method for the dynamics of free boundaries", *Journal of Computational Physics*, v. 39, n. 1, pp. 201–225, 1981. ISSN: 0021-9991. doi: 10.1016/0021-9991(81)90145-5. Disponível em: <https://www.sciencedirect.com/science/article/pii/0021999181901455>.

[57] SOH, G. Y., YEOH, G. H., TIMCHENKO, V. "Improved volume-of-fluid (VOF) model for predictions of velocity fields and droplet lengths in microchannels", *Flow Measurement and Instrumentation*, v. 51, pp. 105–115, 2016.

[58] SOH, G. Y., YEOH, G. H., TIMCHENKO, V. "A CFD model for the coupling of multiphase, multicomponent and mass transfer physics for micro-scale

simulations", *International Journal of Heat and Mass Transfer*, v. 113, pp. 922–934, 2017.

[59] SUSSMAN, M., SMEREKA, P., OSHER, S. "A Level Set Approach for Computing Solutions to Incompressible Two-Phase Flow", *Journal of Computational Physics*, v. 114, n. 1, pp. 146–159, 1994. ISSN: 0021-9991. doi: 10.1006/jcph.1994.1155. Disponível em: <https://www.sciencedirect.com/science/article/pii/S0021999184711557>.

[60] BALCÁZAR-ARCINIEGA, N., ANTEPARA, O., RIGOLA, J., et al. "A level-set model for mass transfer in bubbly flows", *International Journal of Heat and Mass Transfer*, v. 138, pp. 335–356, 2019.

[61] MORA, A. E. M., DE LIMA E SILVA, A. L. F., DE LIMA E SILVA, S. M. "Taylor droplet breakup in T-type microchannels: A detailed flow analysis", *Results in Engineering*, v. 23, pp. 102513, 2024.

[62] KUNDU, P., COHEN, I., DOWLING, D. *Fluid Mechanics*. Elsevier Science, 2012.

[63] BATCHELOR, G. K. *An Introduction to Fluid Dynamics*. Cambridge University Press, 1967.

[64] PORGES, F. "Chapter 6 - Fundamentals of Reservoir Fluid Flow". In: Porges, F. (Ed.), *Reservoir Engineering Handbook (Third Edition)*, third edition ed., Gulf Professional Publishing, pp. 331–483, Burlington, 2006. ISBN: 978-0-7506-7972-5. doi: https://doi.org/10.1016/B978-075067972-5/50009-0. Disponível em: <https://www.sciencedirect.com/science/article/pii/B9780750679725500090>.

[65] SALDANA, M., GALLEGOS, S., GÁLVEZ, E., et al. "The Reynolds Number: A Journey from Its Origin to Modern Applications", *Fluids*, v. 9, n. 12, 2024. ISSN: 2311-5521. doi: 10.3390/fluids9120299.

[66] SMITH, L. H., J. "Some Comments on Reynolds Number", *Journal of Engineering for Power*, v. 86, n. 3, pp. 225–226, 1964. ISSN: 0022-0825. doi: 10.1115/1.3677583.

[67] BANERJEE, R., KUMAR, S. J., MEHENDALE, N., et al. "Intervention of microfluidics in biofuel and bioenergy sectors: Technological considerations and future prospects", *Renewable and Sustainable Energy Reviews*, v. 101, n. 3, pp. 548–558, 2019. ISSN: 1364-0321. doi: 10.1016/j.rser.2018.11.040. Disponível em: <https://www.sciencedirect.com/science/article/pii/S1364032118307949>.

[68] DAMKÖHLER, G. "Einflüsse der Strömung, Diffusion und des Wärmeübergranges auf die Leistung von Reaktionsöfen.: I. Allgemeine Gesichtspunkte für die Übertragung eines chemischen Prozesses aus dem Kleinen ins Große", *Zeitschrift für Elektrochemie und angewandte physikalische Chemie*, v. 42, n. 12, pp. 846–862, 1936. doi: 10.1002/bbpc. 19360421203. Disponível em: <`https://onlinelibrary.wiley.com/doi/abs/10.1002/bbpc.19360421203`>.

[69] REHAGE, H., KIND, M. "The first Damköhler number and its importance for characterizing the influence of mixing on competitive chemical reactions", *Chemical Engineering Science*, v. 229, n. 12, pp. 116007, 2021. ISSN: 0009-2509. doi: 10.1016/j.ces.2020.116007. Disponível em: <`https://www.sciencedirect.com/science/article/pii/S000925092030539X`>.

[70] HEUSSLER, F., OLIVEIRA, R., JOHN, M., et al. "Three-dimensional Navier–Stokes simulations of buoyant, vertical miscible Hele-Shaw displacements", *Journal of Fluid Mechanics*, v. 752, pp. 157–183, 2014. doi: 10.1017/jfm.2014.327.

[71] ARRHENIUS, S. "Über die innere Reibung verdünnter wässeriger Lösungen", *Zeitschrift für Physikalische Chemie*, v. 1U, n. 1, pp. 285–298, 1887. doi: doi:10.1515/zpch-1887-0133. Disponível em: <`https://doi.org/10.1515/zpch-1887-0133`>.

[72] WHITE, F. M. *Viscous Fluid Flow*. 2nd ed. , McGraw-Hill, 1991.

[73] J N REDDY, D. *An Introduction to the Finite Element Method*. McGraw-Hill Education, 2005.

[74] NAVIER, C. L. M. H. "Mémoire sur les lois du mouvement des fluides", *Mémoires de l'Académie Royale des Sciences de l'Institut de France*, v. 6, pp. 389–440, 1823.

[75] LAUGA, E., BRENNER, M. P., STONE, H. A. "Microfluidics: The no-slip boundary condition". In: Tropea, C., Yarin, A. L., Foss, J. F. (Eds.), *Springer Handbook of Experimental Fluid Mechanics*, Springer, pp. 1219–1240, https://doi.org/10.48550/arXiv.cond-mat/0501557, 2007. doi: 10.1007/978-3-540-30299-5_19.

[76] BOCQUET, L., BARRAT, J.-L. "Flow boundary conditions from nano- to micro-scales", *Soft Matter*, v. 3, n. 6, pp. 685–693, 2007. doi: 10.1039/B616490C.

[77] DONEA, J., HUERTA, A. "Introduction and Preliminaries". In: *Finite Element Methods for Flow Problems*, cap. 1, online, John Wiley & Sons, Ltd, 2003.

[78] REDDY, J. N., ANAND, N. K., ROY, P. *Finite Element and Finite Volume Methods for Heat Transfer and Fluid Dynamics*. Cambridge University Press, 2022.

[79] LADYZHENSKAYA, O. A. "The mathematical theory of viscous incompressible flow", *Gordon & Breach*, 1969.

[80] BABUŠKA, I. "The finite element method with penalty", *Mathematics of computation*, v. 27, n. 122, pp. 221–228, 1973.

[81] BREZZI, F. "On the existence, uniqueness and approximation of saddle-point problems arising from Lagrangian multipliers", *Publications des séminaires de mathématiques et informatique de Rennes*, v. 8, n. R2, pp. 1–26, 1974.

[82] O. C. ZIENKIEWICZ, R. L. TAYLOR, P. N. *The Finite Element Method for Fluid Dynamics*. 7 ed. The Boulevard, Langford Lane, Kidlington, Oxford, OX5 1GB 225 Wyman Street, Waltham, MA 02451, USA, Elsevier, 2014.

[83] ROBERT, A., YEE, T. L., RITCHIE, H. "A Semi-Lagrangian and Semi-Implicit Numerical Integration Scheme for Multilevel Atmospheric Models", *Monthly Weather Review*, v. 113, pp. 388–394, 1985. doi: 10.1175/1520-0493(1985)113<0388:ASLASI>2.0.CO;2.

[84] ANJOS, G. R., OLIVEIRA, G. P., MANGIAVACCHI, N., et al. "One- and two-step semi-Lagrangian integrators for arbitrary Lagrangian–Eulerian-finite element two-phase flow simulations", *International Journal for Numerical Methods in Fluids*, v. 94, n. 6, pp. 632–654, 2022. doi: 10.1002/fld.5069. Disponível em: <https://onlinelibrary.wiley.com/doi/abs/10.1002/fld.5069>.

[85] DE OLIVEIRA ANTÃO, G. F. *Implementação de um simulador de escoamento de fluidos em Julia usando método da separação das curvas características*. Tese de Mestrado, Universidade Federal do Rio de Janeiro, 2024.

[86] DAVIS, T. A. "Algorithm 832: UMFPACK V4.3—an unsymmetric-pattern multifrontal method", *ACM Trans. Math. Softw.*, v. 30, n. 2, pp. 196–199, 2004. ISSN: 0098-3500. doi: 10.1145/992200.992206. Disponível em: <https://doi.org/10.1145/992200.992206>.

[87] DALCIN, L. D., PAZ, R. R., KLER, P. A., et al. "Parallel distributed computing using Python", *Advances in Water Resources*, v. 34, n. 9, pp. 1124–1139, 2011. ISSN: 0309-1708. doi: https://doi.org/10.1016/j.advwatres.2011.04.013. Disponível em: <https://www.sciencedirect.com/science/article/pii/S0309170811000777>. New Computational Methods and Software Tools.

[88] GEUZAINE, C., REMACLE, J.-F. "Gmsh: A 3-D finite element mesh generator with built-in pre- and post-processing facilities", *International Journal for Numerical Methods in Engineering*, v. 79, pp. 1309–1331, 2009.

[89] MARCHI, C. H., SUERO, R., ARAKI, L. K. "The lid-driven square cavity flow: numerical solution with a 1024 x 1024 grid", *Journal of the Brazilian Society of Mechanical Sciences and Engineering*, v. 31, pp. 186–198, 2009. doi: 10.1590/S1678-58782009000300004.

[90] ARMALY, B. F., DURST, F., PEREIRA, J. C. F., et al. "Experimental and theoretical investigation of backward-facing step flow", *Journal of Fluid Mechanics*, v. 127, pp. 473–496, 1983.

[91] CACCIA, C. G., CORTI, M., DELLA TORRE, A., et al. "Backward facing step: from fluid flow to conjugate heat transfer with the coupling library preCICE", *IOP Conference Series: Materials Science and Engineering*, v. 1312, n. 1, pp. 012007, aug 2024.

[92] TERUEL, F. E., FOGLIATTO, E. O. "Numerical Simulations of Flow, Heat Transfer and Conjugate Heat Transfer in the Backward-Facing Step Geometry". In: *Proceedings of the International Symposium on Continuum Mechanics and Partial Differential Equations: Contemporary Developments in Continuum Mechanics and Partial Differential Equations*, 2013.

[93] BARTON, I. E. "The entrance effect of laminar flow over a backward-facing step geometry", *International Journal for Numerical Methods in Fluids*, v. 25, n. 6, pp. 633–644, 1997. doi: https://doi.org/10.1002/(SICI)1097-0363(19970930)25:6<633::AID-FLD551>3.0.CO;2-H.

[94] ZANG, Y., STREET, R. L., KOSEFF, J. R. "A Non-staggered Grid, Fractional Step Method for Time-Dependent Incompressible Navier-Stokes Equations in Curvilinear Coordinates", *Journal of Computational Physics*, v. 114, n. 1, pp. 18–33, 1994. ISSN: 0021-9991. doi: https://doi.org/10.1006/jcph.1994.1146.

[95] SANTANA, H. S., SILVA, J. L., TARANTO, O. P. "Optimization of micromixer with triangular baffles for chemical process in millidevices", *Sensors and Actuators B: Chemical*, v. 281, pp. 191–203, 2019. ISSN: 0925-4005. doi: https://doi.org/10.1016/j.snb.2018.10.089. Disponível em: <https://www.sciencedirect.com/science/article/pii/S0925400518318677>.

[96] SOLEHATI, N., BAE, J., SASMITO, A. P. "Numerical investigation of mixing performance in microchannel T-junction with wavy structure", *Computers and Fluids*, v. 96, pp. 10 – 19, 2014. doi: 10.1016/j.compfluid.2014.03.003. Disponível em: <https://www.scopus.com/inward/record.uri?eid=2-s2.0-84897061412&doi=10.1016%2fj.compfluid.2014.03.003&partnerID=40&md5=98c7096412ba712eaf85f761c979ebe5>.

[97] SADEGH CHERI, M., LATIFI, H., SALEHI MOGHADDAM, M., et al. "Simulation and experimental investigation of planar micromixers with short-mixing-length", *Chemical Engineering Journal*, v. 234, pp. 247–255, 2013. ISSN: 1385-8947. doi: https://doi.org/10.1016/j.cej.2013.08.067. Disponível em: <https://www.sciencedirect.com/science/article/pii/S1385894713011200>.